
**Max-Planck-Institut für Metallforschung**
Stuttgart

# Microstructural Studies on the Reoxidation Behavior of Nb-doped $SrTiO_3$ Ceramics

Behnaz Rahmati Kalkhoran

Dissertation
an der
**Universität Stuttgart**

Bericht Nr. 152
März 2004

# Microstructural Studies on the Reoxidation Behavior of Nb-doped $SrTiO_3$ Ceramics

Von der Fakultät Chemie der Universität Stuttgart
zur Erlangung der Würde eines Doktors der
Naturwissenschaften (Dr. rer. nat.) genehmigte Abhandlung

Vorgelegt von
**Behnaz Rahmati Kalkhoran**
aus Teheran

| | |
|---|---|
| Hauptberichter: | Prof. Dr. M. Rühle |
| Mitberichter: | Prof. Dr. F. Aldinger |
| Tag der Einreichung: | 31. März 2004 |
| Tag der Prüfung: | 22. Juni 2004 |

Max-Planck-Institut für Metallforschung Stuttgart
2004

# Contents

# List of Abbrivations

| | |
|---|---|
| AFM | Atomic Force Microscopy |
| CTEM | Conventional Transmission Electron Microscopy |
| EDXS | Energy Dispersive X-ray Spectroscopy |
| GB | Grainboundary |
| HRTEM | High Resolution Transmission Electron Microscopy |
| ICP | Induction-Coupled Plasma |
| OIM | Orientation Imaging Microscopy |
| RHEED | Reflection High-Energy Electron Diffraction |
| RP-phase | Ruddlesden-Popper phase ($Sr_{n+1}\ Ti_n\ O_{3n+1}$, $n$ = 1, 2, 3, …) |
| SAD | Selected Area Diffraction |
| SEM | Scanning Electron Microscopy |
| STEM | Scanning Transmission Electron Microscopy |
| SIMS | Secondary-Ion Mass Spectroscopy |
| STM | Scanning Tunneling Microscopy |
| STS | Scanning Tunneling Spectroscopy |
| TEM | Transmission Electron Microscopy |
| UHM | Ultra High Vacuum |
| UPS | Ultra-Violet Photoemission Spectroscopy |
| XPS | X-ray Photoelectron Spectroscopy |

# Abstract

Donor-doped $SrTiO_3$ ceramics have found application in sensors, varistors, grain boundary layer capacitors and catalysts. This wide range of applications is closely related to the defect chemistry of $SrTiO_3$ and the fact that the properties can be strongly changed by varying the processing parameters. Oxidation of an initially reduced donor-doped $SrTiO_3$ ceramics, for example, leads to a strongly enhanced resistivity, which is generally assumed to result from the formation of cation vacancies. This formation of cation vacancies, however, raises the question of the whereabout of the expelled Sr-ions.

In this contribution, the structural and chemical phenomena observed after high temperature oxidation (at 1200°C for 30 hours) of 5 at.% Nb-doped polycrystalline $SrTiO_3$ are reported. This reoxidation procedure leads to the formation of Sr-rich islands on the surface. These islands exhibit characteristic shapes, areal densities, and sizes, that depend on the surface orientation of the underlying grain. A correlation between grain orientation (determined by orientation imaging microscopy) and tendency towards island formation was found. The structure and the composition of the islands were investigated by transmission electron microscopy and significant differences were observed for different islands. The bulk interior was also investigated after reoxidation. Sr-rich secondary phases were found at the triple grain junctions and could be identified as a Ruddlesden-Popper phase. Moreover, surprising compositional gradients including Sr enrichment were observed in the grain interior beneath the surface. The results are discussed in terms of the defect chemistry of $SrTiO_3$.

# 1. Introduction

The surface as well as the bulk and grain boundary properties of strontium titanate ($SrTiO_3$) are utilized in several applications such as: sensors [Gopel, 85], photocatalysts [Brooks, 87], substrates for the epitaxial growth of high-$T_c$ supperconductors [Aruta, 01], dielectric gates for silicon-based electronic devices ([McKee, 98], [McKee, 01]), varistors [Levinson, 86] and grain boundary layer capacitors (GBLC) [Fujimoto, 85a]. The materials properties underlying these applications can be drastically changed by varying the processing parameters such as stoichiometry, dopant, temperature and oxygen partial pressure ($p(O_2)$) of the ambient gas.

Changing of $p(O_2)$ at high temperatures, for example, induces major changes in the electrical conductivity of the bulk of $SrTiO_3$ ([Daniels, 76], [Eror, 81], [Moos, 97b]). This is explained in terms of the defect chemical model for donor-doped $SrTiO_3$ and $BaTiO_3$ ceramics [Daniels, 76]. Accordingly, at low $p(O_2)$, electrons serve as counter charges to positively charged donors and give rise to the semiconducting behavior of the material. At high $p(O_2)$ (e.g. 1 bar), on the other hand, ionic defects such as strontium vacancies in $SrTiO_3$ (possessing a double negative charge) often adopt the charge balancing task and the material behaves as an insulator. This property is related to the functionality of positive temperature coefficient (PTC) resistors (based on $BaTiO_3$) and GBLCs (based on $SrTiO_3$): The semiconducting ceramics undergo an oxidation procedure and/or acceptor type metal oxide infiltration. While GB oxidation causes the formation of cationic vacancies (acceptor type defects), the infiltration leads to segregation of metal solutes to the GBs (also acceptor type defects). With respect to electrical properties, both processes cause spatially localized acceptor states at the GB, which trap the conduction band electrons. The resulting semiconducting-insulator-semiconducting junctions (double Schottky barriers) at the grain boundaries serve as grain boundary layer capacitors as well as PTC resistors.

From a scientific point of view, however, the location of the cations, released during the cation vacancy formation is still being discussed. Several authors ([Daniels, 76], [Moos, 97II]) assume Sr-rich phases (Ruddlesden-Popper phases [Ruddlesden, 57]) in the bulk of the material as the source of Sr-vacancies (i.e. sink of Sr-ions). Experimental evidence for the formation of Sr-rich secondary phases in the bulk during reoxidation, however, has to date not been given.

Concerning the surface of $SrTiO_3$, variation of $p(O_2)$, leads to surface reconstruction and secondary phase formation ([Liang, 94], [Liang,, 95], [Erdman, 03], [Castel, 02]), which affect the electrical and optical properties of the surface [Tanaka, 93]. Exposure of the (100) surface of single crystalline $SrTiO_3$ to oxygen at high temperatures (1200-1400°C) is reported to result in the formation of Sr-rich secondary phases on the surface ([Meyer, 99], [Szot, 99], [Wei, 01], [Gunhold, 03]). In this context, two different (and partly contradicting) phenomena are discussed in the literature. According to Meyer and Waser ([Meyer, 99], [Meyer, 02]), the near-surface formation of Sr-vacancies leads to the formation of $SrO_x$ complexes on the surface. Szot et. al, [Szot, 99], on the other hand, report that the kinetic demixing of a metastable surface at high temperatures leads to a Sr-rich phase (Ruddlesden-Popper phases, $Sr_{n+1}Ti_nO_{3n+1}$ [Ruddlesden, 57]) on the surface and Ti-rich phases ($TiO_2$ or Magneli-type phases, $Ti_nO_{2n-1}$, [Fujimota, 85b]) in the near-surface region. General agreement concerning chemical and structural properties of secondary phases on the surface, as well as the driving forces leading to its formation, is still not achieved.

The reoxidation (i.e. the change of the charge compensation) and, as a consequence, the Sr-vacancy formation in the bulk and Sr-rich phase at the surface are closely related. Nevertheless, an experimental study dealing with both the oxidation behavior of the surface and the bulk has not been reported yet. In particular, the role of the surface orientations on the oxidation of $SrTiO_3$ has never been investigated and the chemical and structural changes of the bulk during reoxidation are still unknown. These are the main motivations for studying the reoxidation behavior of highly donor doped polycrystalline $SrTiO_3$ in the framework of this PhD thesis.

For this reason, highly Nb-doped (5 mol%) polycrystalline $SrTiO_3$ in stoichiometric composition ([Sr]/([Ti]+[Nb])=1) is used. The surface of such a polycrystalline sample offers a wide range of surface orientations enabling orientation dependent investigations. The preparation of the polycrystalline samples is done in two steps. Firstly, samples are sintered under reducing atmosphere (5% $H_2$ + 95% Ar) at 1360 °C (reduction). Then an additional annealing is performed at a temperature of 1200°C under oxygen atmosphere for 30 hours (reoxidation). The electrical properties of reduced and reoxidized samples are determined by means of impedance spectroscopy. This is to check the semiconducting to insulating transition because of the reoxidation. Structure and chemistry of both, surface and bulk of the resulting ceramics are studied. Morphological and structural aspects were investigated by different imaging methods such as optical microscopy (LM), atomic force microscopy (AFM), scanning electron microscopy (SEM) and transmission electron microscopy (TEM). The

compositional changes upon reoxidation were determined by means of X-ray energy dispersive spectroscopy installed at a transmission electron microscope (XEDS/TEM). For investigating the correlation between different orientations of the surface of the polycrystalline sample and the oxidation tendency of the surface, orientation imaging microscopy (OIM) was applied to the surface of the reoxidized samples.

The outline of the thesis reads as follows: The fundamental aspects of single crystalline and polycrystalline $SrTiO_3$ in terms of the relevant point defects and dominant defect chemical reactions are presented in chapter 2. In addition, the mostly investigated surfaces of $SrTiO_3$, namely (100), (110), and (111) surfaces are reviewed in terms of the surface termination as well as surface reconstruction due to high temperature annealing. In chapter 3, the experimental methods including different types of electron microscopes and impedance spectroscopy are also introduced. In chapter 4, the material system used in this study is discussed and the preparation route of the samples as well as the oxidation procedure is explained. The main results of this study, i.e. the observations related to the reoxidation of the surface, the region beneath the surface and the bulk, are separately reported and discussed in chapter 5 and 6. Finally, the highlights of the reoxidation behavior of donor-doped $SrTiO_3$ are summarized in chapter 7.

# Chapter 2

# Fundamentals and literature review

This work deals with the reoxidation of the surface and the bulk of polycrystalline donor-doped $SrTiO_3$. Therefore, in the first part of this chapter, the bulk properties of single crystalline $SrTiO_3$, the predominant point defects in $SrTiO_3$ and their dependence on the oxygen partial pressure of the ambient atmosphere are reviewed. In the second part, the interaction of the charged defects with the grain boundaries (GBs) in polycrystalline $SrTiO_3$ and consequences on the electrical properties of $SrTiO_3$ ceramics will be discussed. Furthermore, the role of processing parameters on the microstructural evolution and the conductivity of $SrTiO_3$ ceramics will be considered. In the third part of this chapter, the surface of single crystalline $SrTiO_3$ is considered. Different surface orientations and the corresponding terminations of the surface are introduced and the gas-solid interaction at high temperatures is reviewed.

## 2.1 Properties of $SrTiO_3$ single crystals

### 2.1.1 Crystal and electrical structure

At room temperature, $SrTiO_3$ crystallizes in the cubic perovskite structure ($ABO_3$) with a lattice parameter of 0.3905 nm. In the perovskite structure (Fig. 2.1), titanium ions $Ti^{4+}$ as the smaller cations (B-cations) occupy the corner positions of the cube and are surrounded by six oxygen ions $O^{2-}$, located at the cube edge centers thus forming $TiO_6$ octahedral units. The strontium ions $Sr^{2+}$ as the larger cations (A-cations) occupy the larger space in the center of the cube. At lower temperatures, there is a structural phase transition from cubic to tetragonal (110 K) and to orthorhombic (65 K).

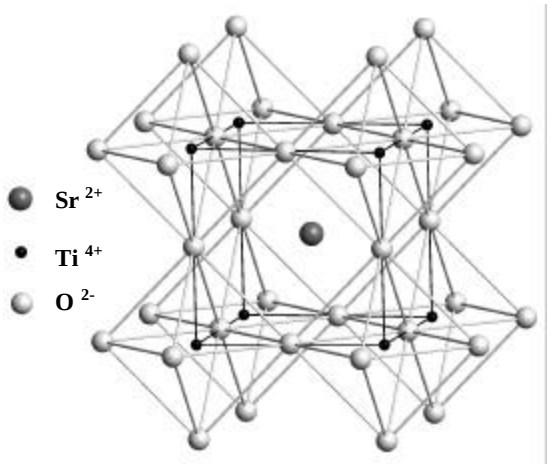


**Fig 2.1:** Cubic perovskite structure of $SrTiO_3$. The radii of $Sr^{2+}$ and $Ti^{4+}$ cations are 0.132 and 0.056 nm, respectively.

In its stoichiometric form (Sr/Ti = 1; O/Sr = 3), $SrTiO_3$ is a good insulator with a 3.2 eV band gap (at T = 0K). The top of the valence band is dominated by O 2p states and the bottom of the conduction band is formed mainly by Ti 3d states ([Henrich, 78], [Reihl, 84]). $SrTiO_3$ has mixed ionic-covalent bonding properties. While a hybridization of O-2p states with the Ti-3d states leads to a pronounced covalent bonding [de Groot, 89], $Sr^{2+}$ and $O^{2-}$ ions exhibit ionic bonding character.

### 2.1.2 Point defects

Defects are inevitable species in crystalline solids. The main defects are point defects such as vacancies, interstitials as well as substitutional species, and, in addition, extended defects such as dislocations, interfaces and precipitates. Point defects in ionic ceramics have either ionic or electronic character.

The description of point defects follows the standard notation for defects in ionic solids introduced by Kröger and Vink [Kröger, 56]. In this notation each point defect is represented by a main symbol, a subscript and a superscript. The main symbol denotes whether the defect is a vacancy (V) or an ion such as "Sr" in $SrTiO_3$. A subscript denotes the site that the defect occupies, and a superscript identifies the relative charge of the defect with respect to the perfect lattice. Positive charges are denoted by dots ($^{\bullet}$), negative charges by dashes ($'$) and ($^{\times}$) represents electroneutral defects.

The intrinsic ionic defects in $SrTiO_3$ are double negatively charged strontium vacancies ($V_{Sr}^{''}$) and doubly positive charged oxygen vacancies ($V_O^{\bullet\bullet}$). Owing to their high formation energies, Ti-vacancies ($V_{Ti}^{''''}$) are usually not considered in defect chemistry of $SrTiO_3$ ([Tien, 67], [Eror, 81], [Moos, 97a]). Electrons ($e'$) in the conduction band and electron holes ($h^{\bullet}$) in the valence band are the electronic charge carriers.

Extrinsic defects such as aliovalent ions (dopants) are often intentionally introduced point defects. The most important criterion for a possible substitution of A- or B-site ions by dopants is a comparable ionic radius of the corresponding species. Dopants with a higher (lower) oxidation level than the host ion act as donors (acceptors). In the following some examples for each type of dopant are given.

**Donors:** Trivalent ions such as $Al^{3+}$, $La^{3+}$ ions on $Sr^{2+}$ sites ($Al_{Sr}^{\bullet}$, $La_{Sr}^{\bullet}$) or pentavalent ions such as $Nb^{5+}$, $Ta^{5+}$ ions on $Ti^{4+}$ sites ($Nb_{Ti}^{\bullet}$, $Ta_{Ti}^{\bullet}$) act as donors.

**Acceptors:** $Fe^{3+}$ as trivalent ions on $Ti^{4+}$ sites ($Fe_{Ti}'$), or $Na^{1+}$ as monovalent dopant on $Sr^{2+}$ sites ($Na_{Sr}'$), act as acceptors.

Consequently, the incorporation of donors and acceptors into the lattice lead respectively to an excess of positively charged defect ($D^{\bullet}$) or an excess of negatively charged defect ($A'$) in the perovskite lattice. Because of the overall charge neutrality condition in a crystal, the formation of charged defects is accompanied by the formation of oppositely charged defects in the crystal. These processes can be considered in terms of defect-chemical reactions and must obey mass, site and charge balance. Defect concentrations are coupled via mass-action laws.

In the following, the defect chemistry (defect-chemical reactions) of $SrTiO_3$ at high temperatures (T > 1000°C) are discussed as a function of $p(O_2)$ and of the type of dopant. High temperatures are assumed because only then $V_{Sr}^{''}$ are assumed to be formed. Chemical reactions involving $V_O^{\bullet\bullet}$ can take place at much lower temperatures (250 - 400°C) ([Moos, 97II], [Leonhardt, 02]).

### i) Interaction of $SrTiO_3$ with the atmosphere

Depending on the $p(O_2)$ of the processing atmosphere, one can expect incorporation (excorporation) of oxygen into (from) the lattice. If a sample is exposed to low $p(O_2)$ (e.g. $10^{-20}$ - $10^{-10}$ atm. at 1000 °C) after equilibration at high $p(O_2)$ (e.g. 1 atm.) neutral oxygen

can be removed from the lattice, leaving behind oxygen vacancies and two electrons in the conduction band. The corresponding defect chemical reaction is shown in Eq.2.1 (left $\rightarrow$ right). On the other hand, if the sample is exposed to high $p(O_2)$ after equilibration in low $p(O_2)$ the chemical reaction runs in the opposite direction and oxygen is incorporated on a vacant lattice site consuming two electrons, Eq.2.1 (right $\rightarrow$ left). In thermodynamic equilibrium, both processes occur at the same rate. The corresponding reaction reads

$$O_O^{\times} \rightleftharpoons V_O^{\bullet\bullet} + 2e' + \frac{1}{2}O_2\ (\text{gas}) \tag{2.1}$$

with the related mass-action law

$$\left[V_O^{\bullet\bullet}\right] n^2\ P(O_2)^{1/2} = K_{Red}(T) = K_{Red}^{\circ}\ \exp\left(-\frac{?H_{Red}}{kT}\right) \tag{2.2}$$

and couples the concentration of oxygen vacancies $\left[V_O^{\bullet\bullet}\right]$ with the concentration of electrons $n$. $K_{red}$ represents the formation constant of oxygen vacancies and is thermally activated with a reduction enthalpy $\Delta H_{Red}$.

### ii) Intrinsic electronic reaction

Electronic defects undergo a generation/recombination process due to excitation of electrons/holes across the band gap. The necessary energy for this process corresponds to the band gap energy of $SrTiO_3$ ($E_g$ = 3.2 eV at 0 K). The corresponding reaction is:

$$\text{nil} \rightleftharpoons e' + \dot{h} \tag{2.3}$$

and the related mass-action law with the intrinsic constant $K_i$ (T) is given by

$$n\ p = K_i(T) = K_i^{\circ}\ \exp\left(-\frac{E_g}{kT}\right). \tag{2.4}$$

$n$ and $p$ represent the concentration of electrons and holes respectively.

### iii) Formation of strontium vacancies

The formation of cation and anion vacancies is coupled via a Schottky reaction ([Maier, 20], [Chiang, 97]). In the case of $SrTiO_3$ the main ionic defects are $V''_{Sr}$ and $V^{\bullet\bullet}_O$ and the corresponding Schottky reaction reads

$$Sr^{\times}_{Sr} + O^{\times}_O \rightleftharpoons V''_{Sr} + V^{\bullet\bullet}_O + SrO(2.phase) \qquad (2.5)$$

where $SrO_{2.phase}$ acts as a sink (source) for Sr ($V''_{Sr}$). The corresponding mass-action equation

$$[V''_{Sr}]\,[V^{\bullet\bullet}_O] = K_S(T) = K^{\circ}_S \exp\left(\frac{-H_S}{kT}\right) \qquad (2.6)$$

relates the defect concentrations to the formation enthalpy $H_S$ of Schottky defects.
The crystal as an electroneutral entity demands a balance between positively and negatively charged mobile and immobile defects including intrinsic and extrinsic defects. The electroneutrality condition (ENC) for $SrTiO_3$ including all charged defects is:

$$n + 2\,[V''_{Sr}] + [A'] = p + 2\,[V^{\bullet\bullet}_O] + [D^{\bullet}]. \qquad (2.7)$$

In many cases only two or three defects are relevant and the ENC can be simplified for different oxygen partial pressure range and doping regimes. However, in all cases the dominant point defects in $SrTiO_3$, namely, $V''_{Sr}$, $V^{\bullet\bullet}_O$, $e'$ and $h^{\bullet}$ are coupled with each other via mass-action laws (Eq. 2.2, Eq. 2.4, Eq. 2.6) and ENC (Eq. 2.7). In the following, two cases are discussed, namely acceptor and donor doping.

## 2.1.3 Defect chemistry of donor doped $SrTiO_3$

The defect chemistry of donor doped $SrTiO_3$ has been intensively studied by conductivity measurements as a function of $p(O_2)$ and temperature. From these measurements a set of mass action laws was developed and mass action constants were determined by Moos [Moos, 97]. Accordingly, the regimes, in which the different defects are relevant, can be sketched schematically in a Kröger-Vink diagram (Fig. 2.2).

- At very low $p(O_2)$ values, (Fig. 2.2: Regime I), according to the reduction reaction (Eq.2.1), oxygen vacancies are the predominant ionic defects compensated by conduction electrons. All other defects, including donors can be neglected. ENC (Eq. 2.7) can therefore be simplified to

$$n \approx 2\,[V_O^{\bullet\bullet}]. \tag{2.8}$$

In this regime, the crystal behaves as a *n*-type semiconductor independent of the type and level of doping. The defect concentration, however, is $p(O_2)$ dependent.

- At intermediate $p(O_2)$ values, (Fig. 2.2: Regime II), the oxygen vacancy concentration becomes small compared to the extrinsic donor concentration. The predominant charged defects in this regime are donors and electrons. Thus, the ENC (Eq. 2.7) would be

$$n \approx [D^{\bullet}]. \tag{2.9}$$

This means, in this regime electronic compensation of donors again leads to a n-type conductivity, now depending on the donor level but not on $p(O_2)$.

- At high $p(O_2)$ values, (Fig. 2.2: Regime III), ionic defects (so-called intrinsic acceptors) in form of strontium vacancies compensate the donors. This is also called cation-vacancy compensation. The simplified ENC is given by

$$2\,[V_{Sr}^{''}] \approx [D^{\bullet}]. \tag{2.10}$$

In thermodynamic equilibrium, the maximum concentration of $V_{Sr}^{''}$ and, hence, the maximum oxygen excess is given by the amount of the donor

$$[V_{Sr}^{''}]_{max} = O_{excess} \approx 0.5\,[D^{\bullet}]. \tag{2.11}$$

Accordingly, a strontium deficiency (strontium vacancy) has to be considered under oxidizing conditions. The formation of Sr-vacancies is accompanied by releasing of Sr from the regular lattice site resulting in the formation of a SrO-rich second phase. This can be expressed by a combination of Eqs (2.1) and (2.5) and leads to

$$Sr_{Sr}^{\times} + \frac{1}{2}O_2(gas) + 2e' \xrightarrow{ox} V_{Sr}^{''} + SrO(2.phase). \tag{2.12}$$

As a sink for the expelled Sr-ions, a Sr-rich phase in the form of Ruddlesden-Popper (RP-phase) SrO.$(SrTiO_3)_n$ [Ruddlesden, 57] has been supposed by several authors. Although, thermogravimetric measurements have verified a mass increase that took place by the formation of Sr-vacancies via an oxygen uptake according to Eq. 2.12 [Moos, 97b] and electrical conductivity measurements $\sigma$ ($p$(O2)) give strong evidence for the formation of Sr-vacancies ([Daniels, 76], [Eror, 81], [Flandermeyer, 84], [Anderson, 85], [Moos, 97b], and [Menesklou, 97]) and computer simulation studies supporting this belief [Akhtar, 95], an experimental evidence for the existing of a Sr-rich second phase in the interior of the material has not yet been given. Secondary phases at the surface, however, have been observed and will be discussed in more detail in section 2.4.

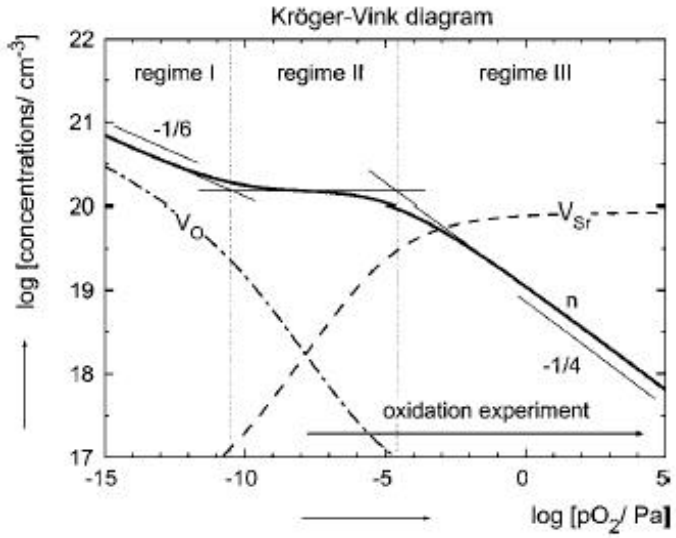


**Fig. 2.2:** Calculated defect concentrations of $e'$, $V_{Sr}^{''}$ and $V_O^{\bullet\bullet}$ for donor-doped (1.0 at.%) single crystal $SrTiO_3$ as a function of $p(O_2)$ at 1400°C. Regimes I, II, and III defined in text. From Meyer et al. [Meyer, 02].

## 2.1.4 Defect chemistry of undoped and acceptor doped $SrTiO_3$

Since nominally pure $SrTiO_3$ contains an excess of ''naturally-occuring'' acceptor impurities such as $Fe'_{Ti}$, the defect chemistry of undoped and acceptor-doped $SrTiO_3$ is essentially the same. The predominant defects depend, as in the case of donor doping, on the level of $p(O_2)$. This is discussed in detail by Daniels [Daniels, 76] and Waser [Waser, 91]. The corresponding dependencies are shown in Fig. 2.3.

- At very low $p(O_2)$ values, (Fig. 2.3: regime Ⅰ), oxygen vacancies and electrons are predominant (ref. Eq. 2.1). This is the same as in the case of donor doping. Respectively, at very low $p(O_2)$ *n*-type conductivity is characteristic and independent of the type and level of doping.
- At intermediate $p(O_2)$ values, (Fig. 2.3: regime Ⅱ), acceptors are compensated by oxygen vacancies. The acceptors can either originate from acceptor type impurities ( A' ) or from frozen-in $V_{Sr}^{''}$. Hence ENC (Eq. 2.7) reads

$$2\,[V_{Sr}^{''}] + [A'] \approx 2\,[V_O^{\bullet\bullet}]. \qquad (2.13)$$

- At high $p(O_2)$ values, (Fig. 2.3: regime Ⅲ), compensation of acceptors takes place via holes (electronic compensation) and this leads to *p*-type conductivity with

$$[A'] \approx p. \qquad (2.14)$$

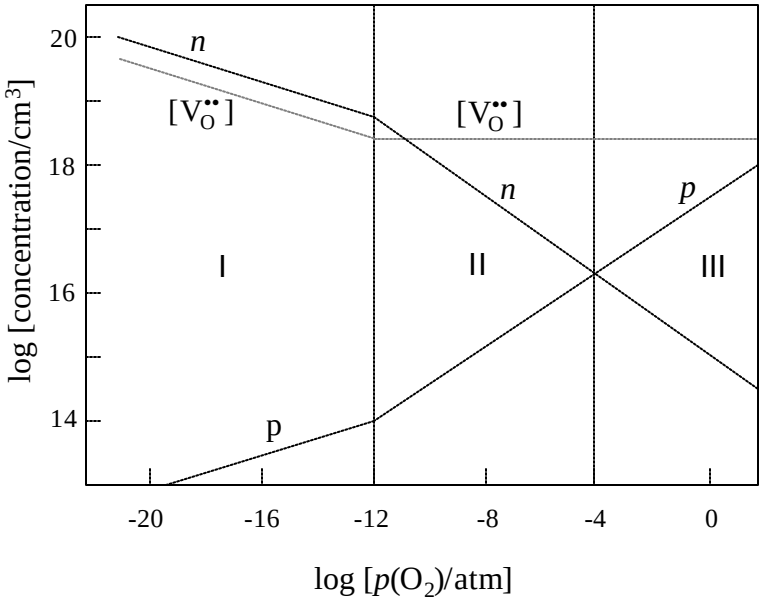


**Fig. 2.3:** Schematic representation of the equilibrium defect model for undoped and acceptor- doped $SrTiO_3$. Regions Ⅰ, Ⅱ, and Ⅲ defined in text. Defect concentrations calculated from conductivites at 1000 °C. From Chan et al. [Chan, 81].

## 2.2 Properties of polycrystalline $SrTiO_3$

In electroceramics materials, such as $SrTiO_3$, exist an interaction between charged defects and the GBs. This interaction leads to a depletion or accumulation of the mobile ionic and/or electronic charge defects at the GBs and consequently result in electrically active GBs. A prominent example for this interaction can be found in acceptor-doped $SrTiO_3$ that has been investigated by several groups ([Vollman, 94], [MacIntyre, 20]). According to the experimental work of Vollman et al. and theoretical studies by McIntyre the accumulation of oxygen vacancies at the GBs results in a positively charged GB core.

The possible driving forces governing this interaction in terms of segregation of point defects into the GBs resulting in electrically active GBs have been discussed by several research groups. Most of the models ([Desu, 90], [Chiang, 90]) are based on the idea of a space-charge compensating the positively charged GB core. These space-charge models consider two segregation driving forces: first, the different vacancy-formation energies of the components at the GB and secondly, the macroscopic electrostatic potential, which results as a consequence of the violation of charge neutrality in the GB-region. Bristowe et. al [Bristowe, 20] makes breaking of crystal symmetry of the bulk at the GB responsible for the electrical properties of the GBs. According to this model a bonding sequence often changes at the GB because the grain orientation relationship between adjacent grains changes there. As a result extra bonding or dangling bonds are generated, and additional GB-states are sometimes created in the band gap.

However, in either case a depletion of the majority charge carriers in the space charge layer at GBs explains the resistive behavior of GBs. Traditionally the potential barrier at the GB is called double-Schottky barrier in analogy to the Schottky barrier at a semiconductor-metal interface. For the potential barrier height ($\Delta\phi$) and the extension of the space charge layer ($w$) the following relations are valid ([Greuter, 99],[Fleig, 20]):

$$\Delta\phi = \frac{(Q_{core})^2}{8\,\varepsilon_\circ\varepsilon_r c_D\, q} \tag{2.15}$$

$$w = \left(\frac{2\,\varepsilon_\circ\varepsilon_r\,\Delta\phi}{q\,c_d}\right)^{1/2} \tag{2.16}$$

where $Q_{core}$ means the core (GB-core) charge, $c_d$ is the dopant concentration and $q$ represents the relative charge of the dopant ion. Potential barrier height and related space charge width in an acceptor doped (0.2 mol% Fe) polycrystalline $SrTiO_3$ are reported by Rodewald et al. [Rodewald, 01]. They applied microcontact impedance spectroscopy to measure electrical properties of individual GBs. Typical barrier heights and space charge widths are about 600 mV and 20-50 nm.

The potential barrier height of the GB can be strongly influenced by temperature and external electric field. The blocking character of GBs and its dependencies on temperature and electric field are used extensively in positive temperature constant resistors (PTCR) [Heywang, 61], varistors [Levinson, 86] and GB layer capacitors (GBLCs) [Fujimoto, 85I].

**Varistors** are voltage-dependent resistors which show a highly non-linear I-V characteristic. At low voltages, the GBs act as Schottky barriers but at sufficiently high voltages the barriers break down. This property is used to protect sensible devices, in which the varistor is connected in parallel with the device. The most widely used commercial varistors are based on ZnO and $SrTiO_3$.

**PTC resistors** are based on polycrystalline, ferroelectric $BaTiO_3$ material and undergo a change in their resistance by several orders of magnitude within a small temperature range in the vicinity of the Curie temperature ($T_C$). Below $T_C$, the charge in the GB is almost completely compensated by the ferroelectric polarization of the domains crossing the GB. Therefore potential barriers are low and lead to a comparably low GB resistance. Above $T_C$, ferroelectric domains disappear, GBs maintain their electrical charge and according to Eq. 2.15 the potential barrier increases since ε decreases according to Curie-Weiss law. Typical applications of PTCRs are self-regulating heating elements or protection devices against overheating.

**GBLC** are based on a semiconductor-insulator-semiconductor junction at GBs. While semiconducting grains are achieved by donor-doping, insulating regions at GBs originate either from oxidation of GBs and/or infiltiration of GBs by acceptor type metal oxides. $SrTiO_3$ ceramics is commercially used for the fabrication of GBLCs with niobium as donor dopant and potassium, sodium or lead as typical acceptors at GB.

## 2.3 Effect of processing parameters on the microstructural and electrical properties of polycrystalline $SrTiO_3$

The microstructure as well as the electronic properties of electeroceramics depend sensitively on the processing parameters such as stoichiometric or non-stoichiometric composition, dopant level, processing temperature and processing atmosphere (i.e. oxygen partial pressure). In the following some explanations are given about the role of each processing parameter on the microstrucural evolution and defect chemistry of ceramics.

### 2.3.1. Stoichiometric and non-stoichiometric compositions

A stoichiometric composition with respect to cations means equal concentration of cations on A- and B-sites. In the case of Nb-doped $SrTiO_3$, this means [Sr] = [Ti] + [Nb] and the general formulation for a stoichiometric system would be $Sr_1Ti_{1-x}Nb_xO_3$. A non-stoichiometric composition can lead to the formation of Sr- or Ti-rich secondary phases. The effect of non-stoichiometry in $SrTiO_3$ can be derived from the phase diagram of the quasi binary system (SrO-$TiO_2$) (Fig. 2.4).

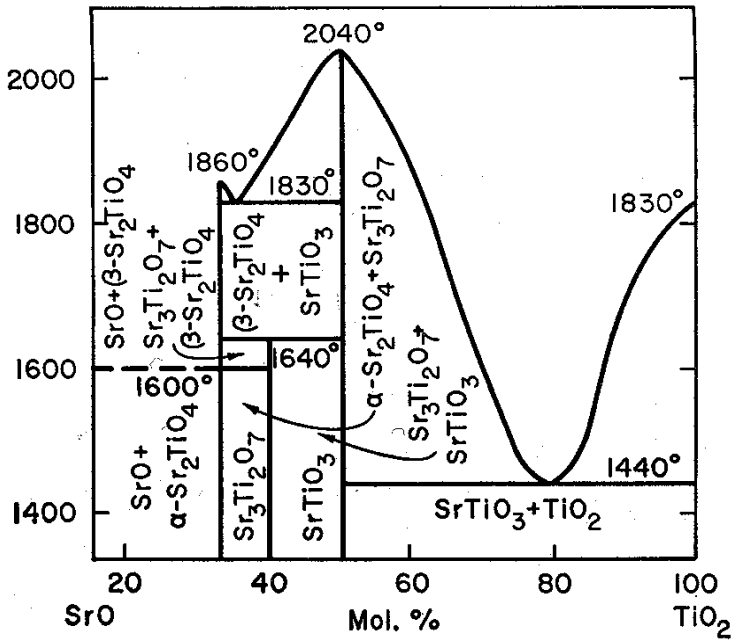


**Fig. 2.4:** SrO-$TiO_2$ binary system [Levin, 64].

Sr as well as Ti possess a low solid solubility. According to Smyth and Witke [Smyth, 81], at temperatures below 1400 °C, $SrTiO_3$ can dissolves less than 0.5 mol% excess of $TiO_2$ and less than 0.2 mol% excess of SrO. Higher amounts of Sr lead to the formation of Sr-rich phases such as $Sr_2TiO_4$, $Sr_3Ti_2O_7$ phase (see Fig. 2.4). These are well known as Ruddlesden-Popper-phases ($Sr_{n+1}Ti_nO_{3n+1}$) [Ruddlesden, 57]. In the case of Ti-excess, a Ti-rich phase, such as $TiO_2$ or Magneli-phases ($Ti_mO_{2m-1}$) can be expected [Fujimota, 85b].

In this study the Ruddlesden-Popper-phases (RP-phases) play an important role during the reoxidation process. Therefore, the formation mechanism and structure of RP-phases are now briefly introduced. A RP-phase is obtained by inserting a rock-salt type SrO layer in every *n* th strontium titanate perovskite unit cell along the [001] direction (Fig. 2.5) ([Tilley, 77], [Balachandran, 82b], [McCoy, 97]). The resulting phase with the general formula $SrO(SrTiO_3)_n$ exhibits a tetragonal structure. The planar defects can be described as a crystallographic shear of the perovskite structure such that sheets of $TiO_6$ octahedra along (001) are moved and the remaining perovskite layer is sheared by 1/2 [111].

The existence of these Sr-rich phases was recognized for the first time by S. N. Ruddlesden and P. Popper in 1957 [Ruddlesden 57]. Similar types of defects have been reported for A-site-rich $CaTiO_3$ [Ceh, 94], but such phase formation has not been reported in the BaO-$TiO_2$ system [Smyth, 85].

The idealized structure of a few RP-phases such as $SrTiO_3$ ($n$= 8 ), $Sr_2TiO_4$ ($n$=1) and $Sr_3Ti_2O_7$ ($n$=2) are shown in Fig. 2.5. The related lattice parameters are listed in Table 2.1. These oxides can all be regarded as members of a homologous series of oxides with the general formula $Sr_{n+1}Ti_nO_{3n+1}$.

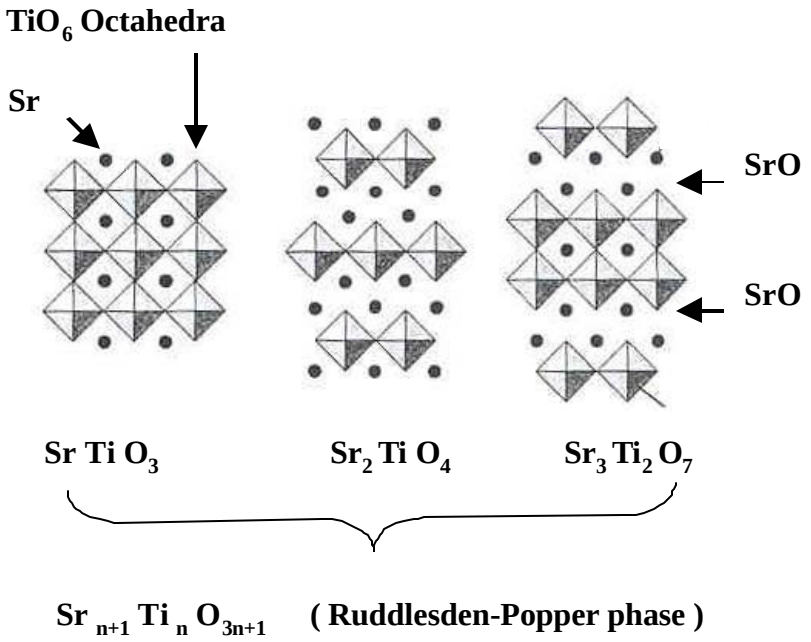


**Fig. 2.5:** Schematic diagram of Ruddlesden-Popper (RP) defect structures.

RP-phases are detectable by diffraction techniques as well as high-resolution transmission electron microscopy (HRTEM). The introduction of *n* SrO-layer in [001] direction, leads to the appearance of *n+1* additional spots in this direction in electron diffraction patterns. In HRTEM images, this is observed as coherent intergrowth of lamellae of the $SrTiO_3$ structure with a thickness of *n* unit cells, localized along planes of SrO. These evidences were very clearly shown by Tilley [Tilley, 77].

**Table 2.1:** Lattice constants of $SrTiO_3$, Ruddlesden-Popper phases $Sr_{n+1}Ti_nO_{3n+1}$ (space group *I*4/mmm) [Szot, 99].

| | $SrTiO_3$ | $Sr_2TiO_4$ | $Sr_3Ti_2O_7$ | $Sr_4Ti_3O_{10}$ | $Sr_5Ti_4O_{13}$ |
|---|---|---|---|---|---|
| ***n*** | ∞ | 1 | 2 | 3 | 4 |
| **a = b [Å]** | 3.992 | 3.983 | 3.935 | 3.927 | 3.922 |
| **c [Å]** | 3.992 | 11.80 | 19.66 | 27.50 | 35.40 |

## 2.3.2. Sintering temperature

The microstructure and particularly the grain sizes of a ceramics may be strongly influenced by the sintering temperature ($T_{sint.}$). According to the phase diagram (Fig. 2.4), the eutectic temperature ($T_{eut.}$) of $SrTiO_3$ is 1430°C. Hence, sintering can occur at two different temperature levels, namely over or below the $T_{eut}$. In many cases, a Ti-excess is introduced into the stoichiometric composition ([Fujimoto, 85II], [Cho, 94]) since this promotes the sintering. However, according to the phase diagram (Fig. 2.4) this also yields a Ti-rich secondary phase. Cho et. al [Cho, 94] discussed in detail the microstructural evolution for the two temperature ranges:

- **$T_{sint.} > T_{eut.}$ :** According to the phase diagram, $TiO_2$-phase appears as a liquid phase which surrounds the grains and grain-growth occurs. This process is known as liquid-phase sintering.
- **$T_{sint.} < T_{eut.}$:** At these temperatures a discrete $TiO_2$ solid-phase is formed during sintering and when the amount of second phase in the GBs and in triple grain junctions is large, grain-growth is inhibited.

## 2.3.3. Oxygen partial pressure during sintering

The oxygen partial pressure during sintering drastically influences the microstructure as well as the electrical properties of ceramics. Sintering in reducing atmosphere, for example in $N_2$+$H_2$ gas mixture or in UHV, enhances the density of ceramics and promotes grain growth ([Wei, 98], [Lee I, 01], [Lee II, 01]). This is explained in the following:

Densification and grain growth are accompanied by the transfer of material and the rate at which it occurs depends on the rate of diffusion of ions. Since in reducing atmosphere oxygen vacancies are the most mobile ionic defects, densification and grain growth occur via fast diffusion of oxygen vacancies.

On the other hand, in oxidizing atmosphere, , the formation of cation vacancies ($V_{Sr}^{''}$) at the GBs during oxidation is assumed to introduce a preferential segregation of donors or positively charged impurities to the GB [Chiang, 90]. The pinning of GBs by these segregants inhibits GB mobility (solute-drag boundary migration) and consequently prevents the grain growth.

Furthermore, the electrical properties of electroceramics depend very sensitively on $p(O_2)$. The dependency is coupled to the defect concentrations, discussed at the beginning of this chapter for donor and acceptor doping. The acceptor doped $SrTiO_3$, for example, exhibits a

transition from *n*-type through ionic to *p*-type conductivity by changing of $p(O_2)$ from very low values ($10^{-20}$–$10^{-10}$ atm.) to oxygen ambient (1 atm.) at 1000-1200 °C. The change of the conduction character with varying oxygen partial pressure is schematically shown for each type of doping in Fig.2.2, and Fig. 2.3.

However, one has to take into account that conductivity and concentration essentially differ by the mobility which is significantly higher for electronic than for ionic defects.

## 2.4 Properties of $SrTiO_3$ surface

$SrTiO_3$ surface has a wide range of applications, for example, as substrate for the growth of different type of thin films, such as high temperature superconductor thin films [Aruta, 01], as well as in the photoelectrolysis [Brook, 87]. Mostly, applications are based on the interaction of the surface with ambient gas at high temperatures, which strongly influence the surface structure, composition (e.g. [Liang, 94]) and electronic properties [Tanaka, 93]. There are numerous studies concerning reconstructuring of (100) and (110) surfaces ([Liang, 94], [Liang, 95], [Szot, 99], [Wei, 01], [Castel, 02], [Gunhold, 03]), but less studies about the (111) surface [Sekiguchi, 98]. In the following, a brief discussion of specific surface orientations and different surface-terminations is given.

**(100) surface**: An ideally stoichiometric $SrTiO_3$ crystal is formed by sequential stacking of neutral SrO and $TiO_2$ layers along the [100] direction (Fig. 2.6a). Independent of the termination, the (100) surface can therefore be considered as a non-polar surface. Usually, vacuum-fractured surfaces show fragments of both types of surface (SrO and $TiO_2$ terminations), but high temperature annealing can provide atomically smooth surfaces of either type ([Polli, 99], [Fu, 02]).

**(110) surface:** In its normal direction, this surface consists of alternating oppositely charged $(SrTiO)^{2+}$ and $O^{2-}$ planes. Therefore, the (110) surface is a polar surface. The sequences of these planes are shown in Fig. 2.6b.

**(111) surface** : Since the perovskite lattice consists of sequences of oppositely charged $(SrO_3)^{4-}$ and $Ti^{4+}$ layers in the <111> direction (Fig. 6c), the (111) surface is also considered as a polar surface. Additionally, the (111) plane and respectively the (111) surface is the closed-packed plane in the perovskite lattice of $SrTiO_3$.

A large number of studies have used numerous surface science techniques in order to understand surface structure variations of $SrTiO_3$ (100), (110) and (111) under different annealing parameters.

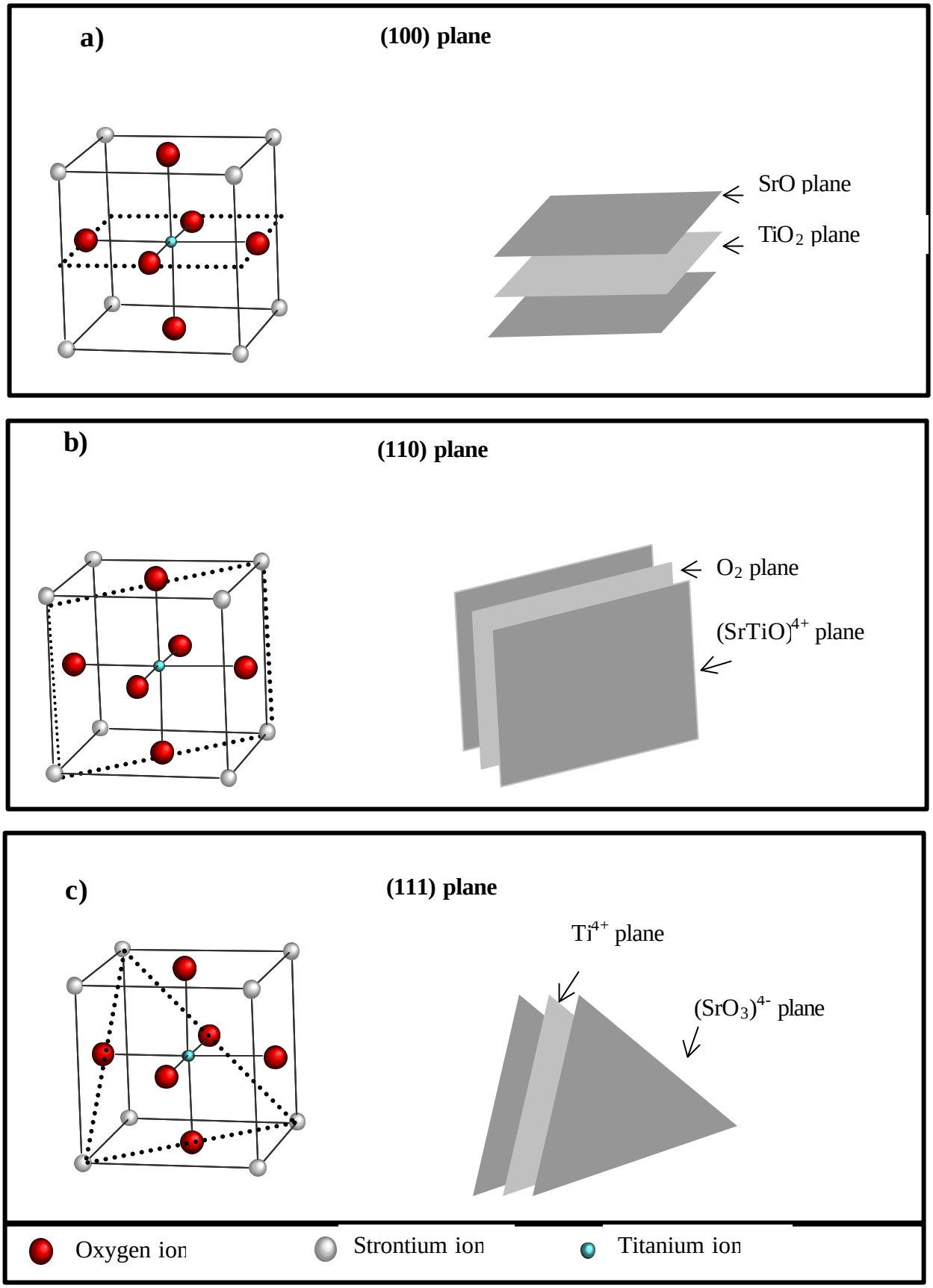


**Fig. 2.6**: $SrTiO_3$ cubic unit cell. **a)** sequence of (100) layers $SrO/TiO_2$; **b)** sequence of (110) layers $SrTiO/O_2$; **c)** sequence of (111) layers $SrO_3/Ti$.

A summary of results published in the literature are presented in Table 2.2. It should be mentioned that the results obtained by different groups are partly contradictory.

**Table 2.2:** Summary of the results obtained by different groups on $SrTiO_3$ surfaces after annealing under different conditions.

| Surface | Observed reconstruction | Surface preparation | Technique | Reference |
|---|---|---|---|---|
| (100), (110) | Row-like structures (RP-phase) | UHV annealing, 650°C | SEM | [Liang, 95] |
| (100), (110) | SrO island | UHV annealing, 1300°C | SEM | [Liang, 95] |
| (111) | $Sr–O_{3-x}$ outermost layer | UHV annealing,, 1180 °C | STM, RHEED | [Tanaka, 96] |
| (111) | Ti outermost layer | UHV annealing,, 1220 °C | STM, RHEED | [Tanaka, 96] |
| (100), (110) | Sr-rich phase (RP-phase, $n = 1$) | $O_2$ annealing, 900 °C | AFM | [Szot, 99] |
| (100), (110) | Ti-rich phase (TiO or $TiO_2$) | UHV annealing, 900°C | AFM | [Szot, 99] |
| La-doped (100) | SrO-rich phases (RP-phase) | $O_2$ annealing, 1380°C | EDX(SEM), AFM, SIMS, UPS | [Meyer, 99] |
| La-doped (100) | SrO islands, overed by $SrO_2$ | Air annealing, 1300°C | UPS | [Wei, 01] |
| (111) | Trench structure | $O_2$ annealing,, 1000 °C | AFM | [Sekiguchi, 98] |
| (111) | Self-similar triangles (Sierpinski gasket) | Air annealing,, 1000 °C | AFM | [Sekiguchi, 98] |
| (111) | $SrO_x$ islands | Ar annealing,, 1000 °C | AFM | [Sekiguchi, 98] |
| (111) | No secondary phase | Air annealing,, 1300 °C | ATM, Auger spectroscopy | [Gunhold, 02] |
| La-doped (100) | $Ti_2O_3$ islands | UHV annealing,, 1300 °C | ATM, Auger spectroscopy | [Gunhold, 02] |

# Chapter 3

# Experimental Methods

Since the grain size of ceramics is in the micrometer range, optical microscopy was applied to analyze the grain shape, grain size, grain size distribution, porosity and secondary-phase formation. In addition, different types of electron microscopy techniques were used to obtain data related to crystallographic and compositional effects. Electrical properties of the ceramics are investigated by means of impedance spectroscopy.
In the following, a short summary to each method is given. Finally, the individual sample preparation necessary for each investigation technique is introduced.

## 3.1 Electron microscopy

Electron microscopy is based on the analysis of elastically and inelastically scattered electrons after passing through the specimen. Fig. 3.1 summarizes *(i)* different scattering processes, *(ii)* the related method of characterization for each process, and *(iii)* also the detected data from the specimen. While scanning electron microscopy (SEM) analyzes the secondary and the back scattered electrons from the surface of the sample, transmission electron microscopy (TEM) characterizes the transmitted electrons.

## I. SEM (Topography studies)

In SEM, the secondary electrons (SEs) are used to build up the image. These are electrons which are ejected by the incident electrons from the conduction or the valence band of the atoms of the specimen. Since SEs are usually assumed to be free electrons (they are not associated with a specific atom), they contain no specific chemical information. Due to their low kinetic energy, they can only escape if they are near the specimen surface and therefore produce an image of the surface and the topology of the specimen. [Williams, 96].

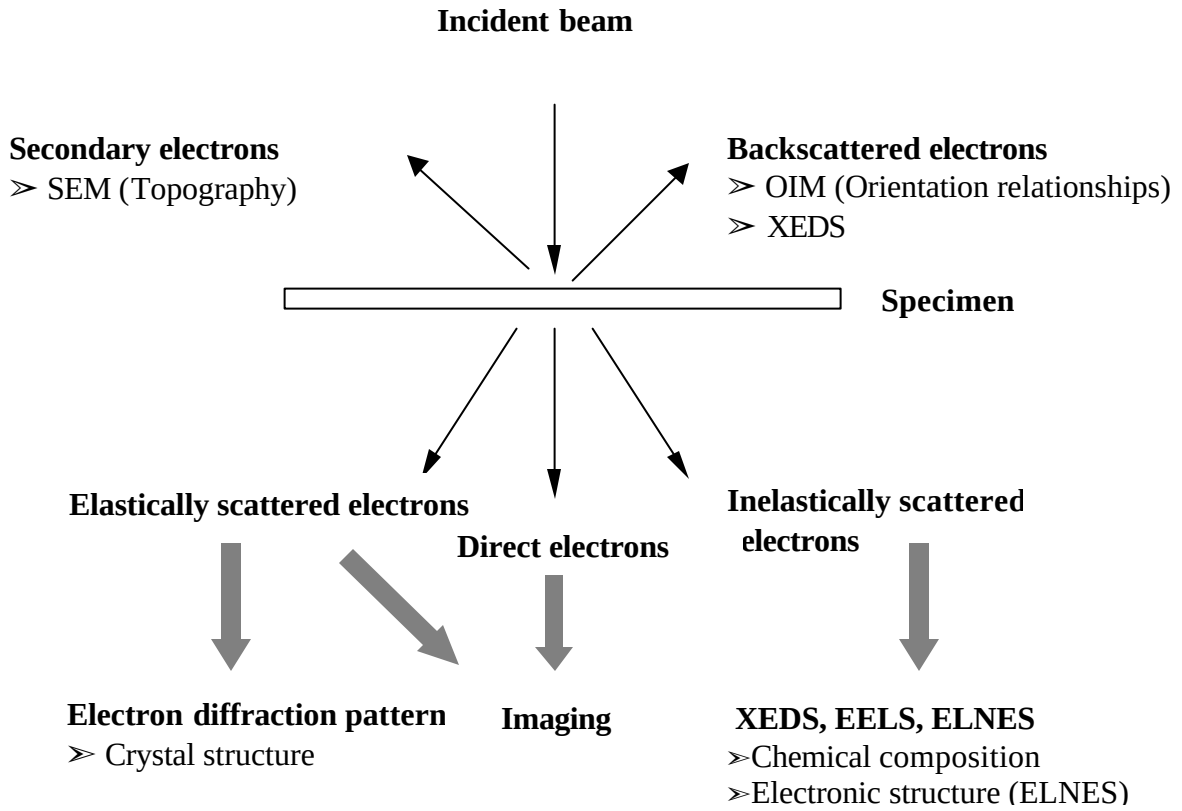


**Fig. 3.1:** Different types of interactions between an incident beam and the crystalline sample. The generated signals are detected and analyzed by different types of detectors. (Here only those processes used for this work, for details see Williams and Carter [Williams, 96]).

## II. Orientation Imaging Microscopy (OIM)

The determination of the orientations of the individual grains in a polycrystalline material can be achieved by using orientation imaging microscopy (OIM) [Schwarz, 20]. By rapidly capturing and analyzing electron backscatter diffraction (EBSD) patterns from the bulk of the sample, OIM produces local orientation measurements and can therefore detect the different orientations of the grains. In the following the formation of EBSD patterns and the resulting OIM map is described.

**EBSD:** The electron beam strikes the sample (tilted by about 70°) and is inelastically scattered in all directions (Fig. 3.2). Some of the scattered electrons move at an angle $\theta_B$ (Bragg angle) to an (*hkl*) lattice plane thus fulfilling the Bragg condition (Fig. 3.3a). Since the scattered electrons move in all directions, they scatter into one of two cones (Kossel cones),

located on either side of the (*hkl*) planes (Fig. 3.3b). The intersection of these cones with the Ewald sphere (see this chapter, section III) appears as a pair of dark and bright lines on the phosphor screen (Fig. 3.3c). A pair of such lines is referred to as "Kikuchi band" and assigned to a given (*hkl*) plane. The assembly of Kikuchi bands forms the so-called electron back scattered pattern (EBSD).

Once the EBSD pattern is imaged on a phosphor screen connected to a CCD (charged couple device) camera, the OIM software identifies the zone axis [*uvw*] (common line of a set of *hkl* planes) and the associated *hkl* planes (Fig. 3.3b,c). The data for each measuring point (Fig. 3.4b) contains three "Euler angles" defining the orientation of the crystal, coordinates (x,y) of the measuring point on the specimen, a quality factor (IQ) defining the sharpness of the diffraction pattern, and a confidence index (CI), indicating the degree of confidence that the indexing is correct. In this manner a large number of crystallographic data from the area of interest can be collected. Since the spatial resolution of the back scattered electron diffraction is typically about 0.2 µm, with variations depending on the atomic number of the sample, the accelerating voltage and the beam current used in SEM, the application of this method is limited to polycrystalline material with a minimum grain size of 0.2 µm.

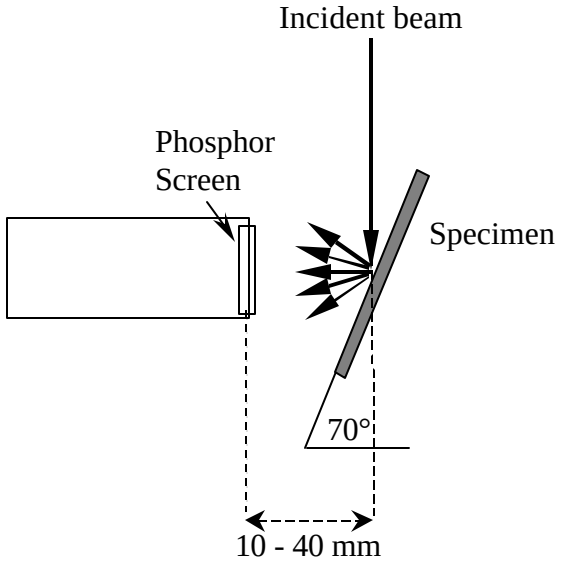


**Fig. 3.2:** Optimal position and tilting of the specimen relative to the phosphor screen and the electron beam for getting maximum signal on the phosphor screen.

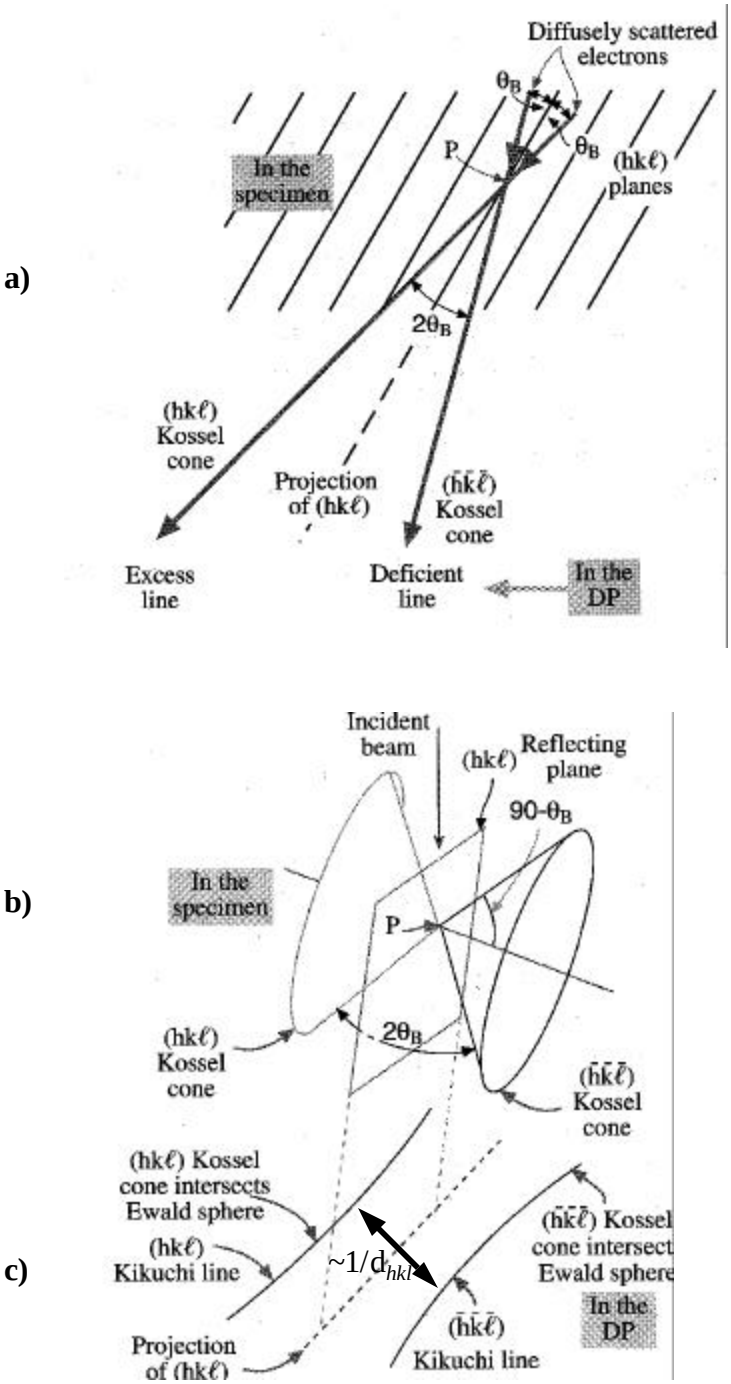


**Fig. 3.3:** Formation mechanism of Kikuchi lines: Diffusely scattered electrons in the sample are **a)** diffracted from (*hkl*) planes under Bragg angles $\theta_B$, **b)** the diffracted electrons form Kossel cones, **c)** the cones intercept the Ewald sphere, creating Kikuchi lines. See Williams and Carter, [Williams, page 292].

Fig. 3.4 shows the OIM map of polycrystalline $SrTiO_3$. It is based upon 3000 local orientation measurements. The colors in the map indicate via stereographic triangle (Fig. 3.4d) the orientations of the grains with respect to a reference direction (e.g. the normal direction of sample: [001]). While the red color, for example, denotes grains with their <001>-direction being aligned parallel to [001], the green color remarks the grains which have their <101>-direction aligned parallel to the [001] and so on. The grain boundaries are realized in the OIM-map in the following way: If two neighbouring points differ in orientation by less than 15° then a dashed line segment indicating a small angle GBs (SAGB) is drawn between two points in the map, but if the misorientation between two points exceeds 15° then a thick line, reflecting a large angle GB (LAGB), is drawn. Furthermore, special boundaries (CSL boundaries) can be derived form these data too. For this reason, a tolerance value is needed. This value gives the permitted deviation from an exact CSL boundary. The fundamental description for the CSL criterion given by Brandon [Brandon, 66] is

$$\text{Tolerance angle} = \frac{K}{\Sigma^n} \tag{3.1}$$

$\Sigma$ denotes the type of CSL boundary. The parameters $K$ and $n$ chosen in this work are those proposed by Brandon ($K$ = 15 and n = *0.5*). After this criterion, as an example, the maximum deviation permitted for a $\Sigma$3 boundary is 8.7°.

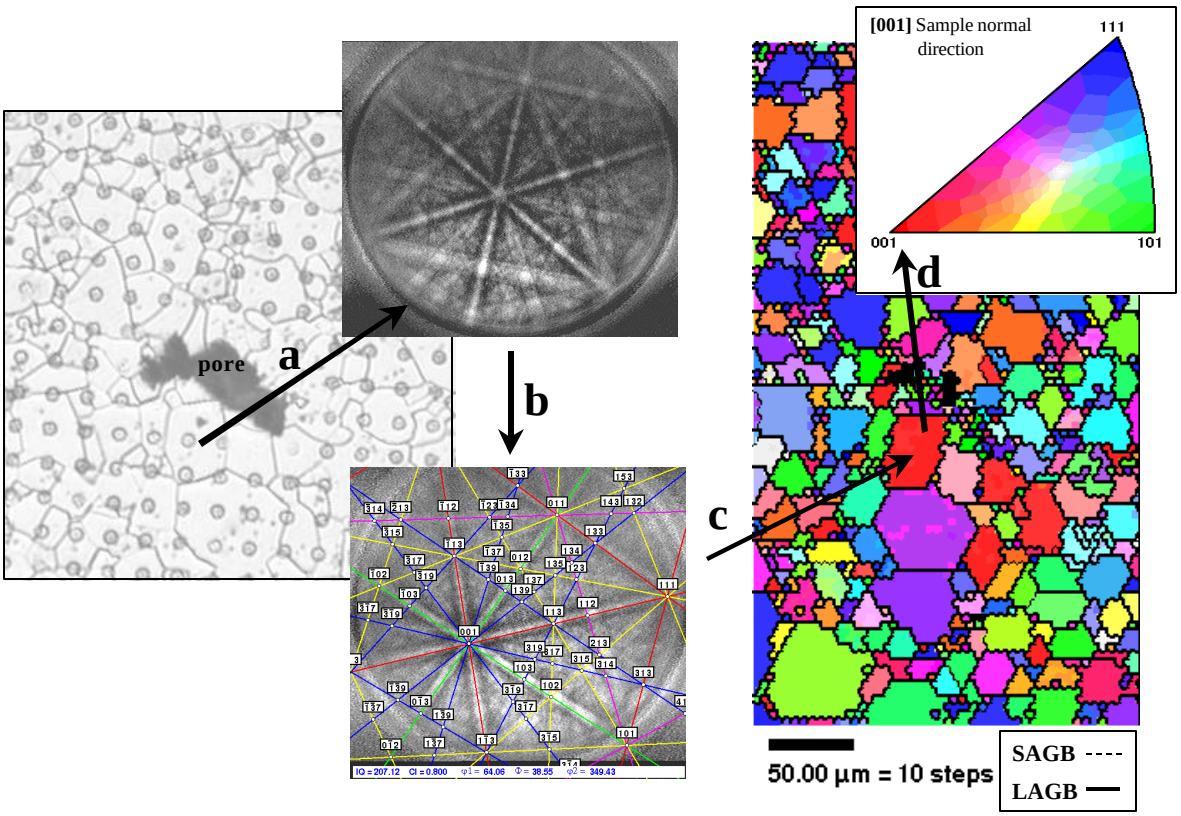


**Fig. 3.4:** The OIM map of a polycrystalline $SrTiO_3$.The dark mark in the sample relates to a pore, which is used to find the specific area of the sample again after tilting of the sample by 70° in the SEM. The arrays of dark discs on the surface relate to the microelectrodes which are used for local electrical measurements. **a)** Several EBSD patterns (number depending on the step size of the measurements) are obtained from the grains, **b)** the automated indexing of the patterns determines the zone axis of the patterns, **c**) the corresponding OIM map of the examined area, where the color of each grain has to be assigned to that in the stereographic triangle **(d)**, which represents the orientation normal to the specimen surface.

## III. Transmission Electron Microscopy (TEM)

TEM deals with the transmitted and under specific angle forward scattered part of electrons after passing through the specimen. Fig. 3.5 illustrates the path of the electron beam in a TEM. The electron beam is produced in the microscope by either a thermionic (e.g. from a Tungsten-or a $LaB_6$-crystal) or a field emission process (e.g. Tungsten) and is accelerated to the desired kinetic energy. It travels through an array of magnetic lenses, the condensor lens system, which provides a parallel or a convergent incident beam on the sample, the sample itself, the objective lens, which produces the image, and additionally intermediate and projector lenses, which rotate the intermediate images and adjust their magnification.

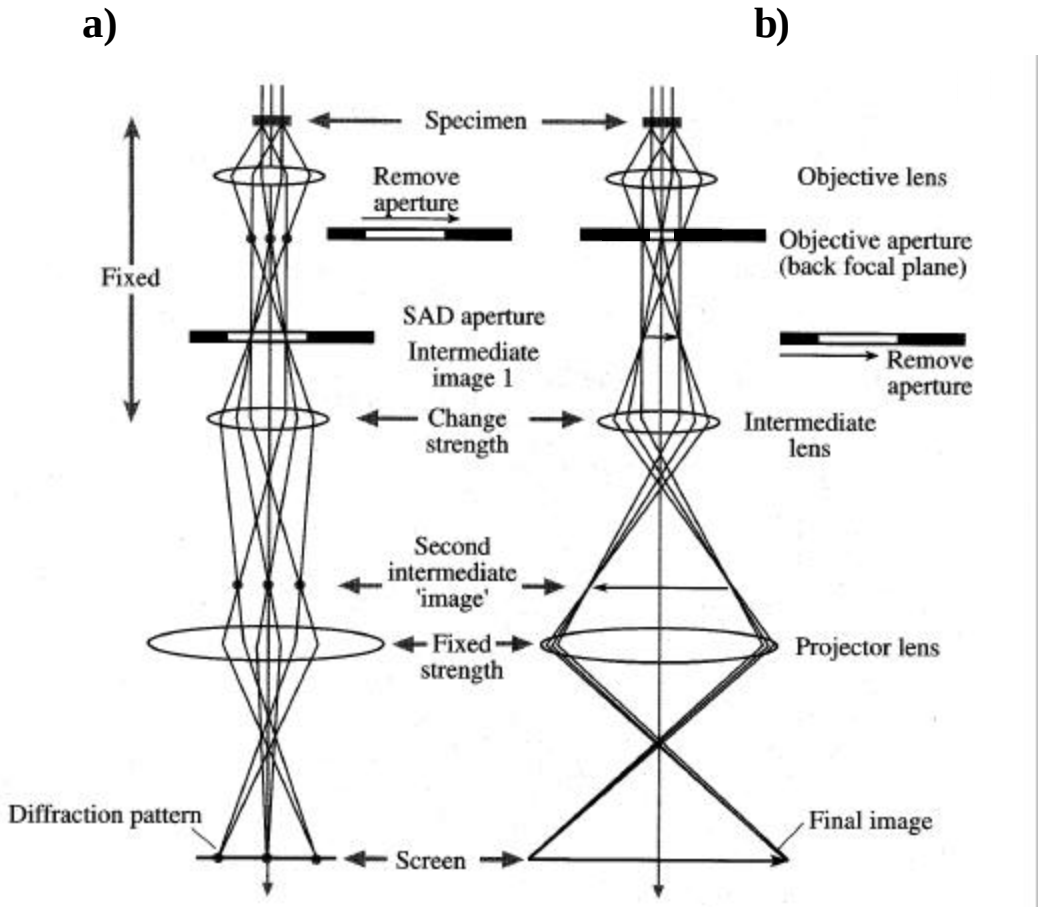


**Fig. 3.5:** Ray diagram of a TEM operating in **a)** Bright-field imaging mode, **b)** diffraction mode [Williams, page 87].

Since the lenses are electromagnetic, changing the strength of the lens by changing the electron current that flows through them leads to a change of the intensity of the illumination, the focus and the magnification of the image. Finally, the intensity of the transmitted electron wave appears as an image or diffraction pattern on the TEM screen by excitation and subsequent emission of photons of the phosphor coating on the screen. Alternatively, a CCD camera, film, image plates or video camera can be used for recording.

### i) Electron diffraction pattern

The elastically diffracted electrons appear on the TEM screen as an array of bright spots (bright intensities) in a particular arrangement and distances depending on the structure of the sample under investigation. Since the direct beam is so intense that it will buckle the specimen and damage the viewing screen, there is a possibility to reduce the illuminated area of the specimen by inserting an aperture (selected area diffraction aperture, SAD) into the back focal plane of the objective lens. Subsequently, this plane is then imaged by the following lenses on the screen.

As an example, Fig. 3.6 shows the electron diffraction pattern of $SrTiO_3$ oriented in the [001] direction.

For understanding electron diffraction patterns, one has to describe the elastic scattering in reciprocal space (Fig. 3.7). In this space each set of parallel atomic (*hkl*) planes is represented by a single point located a distance $1/d_{hkl}$ from the lattice origin. The reciprocal lattice is formed by the collection of all (*hkl*) planes in the crystal. A reciprocal lattice vector $\vec{g}_{hkl}$ is assigned to each point in this space. The vector $\vec{g}_{hkl}$ is defined as a combination of the unit cell vectors (a*, b*, c*) in reciprocal space as follows:

$$\vec{g}_{hkl} = h\,\mathrm{a}^* + k\,\mathrm{b}^* + l\,\mathrm{c}^* \qquad (3.2)$$

where *h*, *k*, and *l* together define the (*hkl*) plane and

$$\vec{\mathrm{a}}^* = \frac{\vec{\mathrm{b}}\times\vec{\mathrm{c}}}{\Omega}; \qquad \vec{\mathrm{b}}^* = \frac{\vec{\mathrm{c}}\times\vec{\mathrm{d}}}{\Omega}; \qquad \vec{\mathrm{c}}^* = \frac{\vec{\mathrm{a}}\times\vec{\mathrm{b}}}{\Omega}\ ; \qquad \Omega = \vec{\mathrm{a}}\cdot(\vec{\mathrm{b}}\times\vec{\mathrm{c}}) = \text{ unit cell volume.}$$

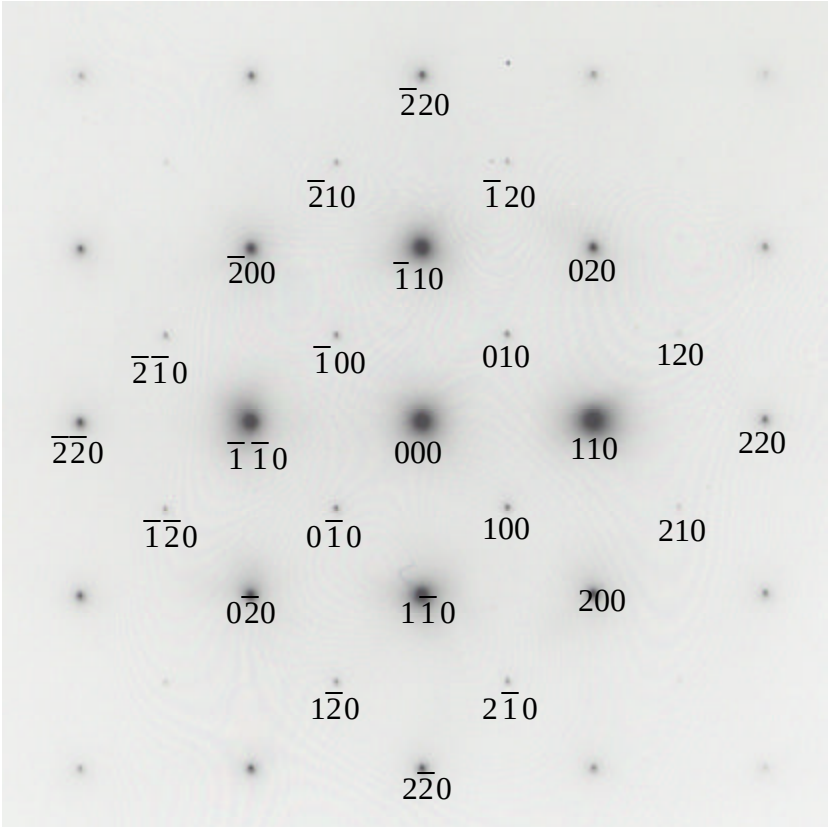


**Fig. 3.6:** Diffraction pattern of $SrTiO_3$ in [001] zone-axis. Each spot is due to electron scattering by a specific *(hkl)* plane.

Elastic scattering is described in reciprocal space by the condition

$$\left|\vec{k}_D\right| = \left|\vec{k}_I\right| \tag{3.3}$$

in which $\vec{k}_I$ and $\vec{k}_D$ denote wave vectors ($\left|\vec{k}\right| = 2\pi/\lambda$) of the incident and the diffracted electrons. By construction of a sphere with radius $\left|\vec{k}_I\right|$ in reciprocal space (Ewald sphere) that passes through the origin of the reciprocal lattice, some of the reciprocal lattice points intersect the surface of the Ewald sphere. These lattice points satisfy the following condition

$$\vec{k}_D - \vec{k}_I = \vec{g}_{hkl}. \tag{3.4}$$

Eqs. 3.3 and 3.4 are known as Laue-condition. Accordingly, reciprocal lattice points which intersect the Ewald sphere fulfill the Laue-condition and give rise to diffraction with the characteristic scattering amplitude (A). In kinematic approximation with consideration of the curvature of the Ewald sphere, the observed intensities ($I_g$ = intensity at $\vec{g}$) in the electron diffraction pattern for a thin foil are determined by [Hirsch, 65]

$$I_g = \left|A_g\right|^2 = \left|u_g\right|^2 \frac{\sin^2(\pi\ t\ s_g)}{s_g^{\ 2}} \qquad (3.5)$$

in which $u_g$ is proportional to the Fourier-coefficient of the electrostatic crystal potential $V(\vec{r})$ at $\vec{g}$ , t is the thickness of the sample and $s_g$ is the excitation error (= $1/2\,|\vec{g}\,|$). Since it is impossible to produce a perfectly parallel incident beam, the diffraction spots have a certain non zero diameter, reflecting the convergence angle of the electron beam.

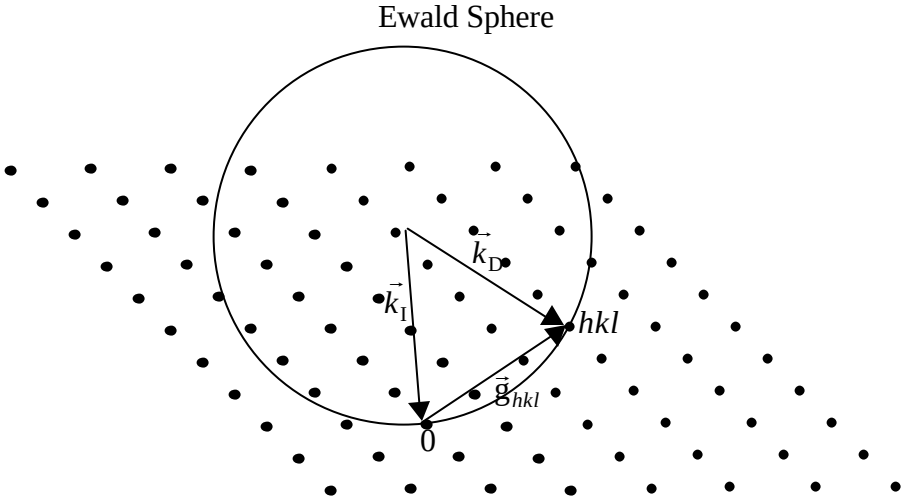


**Fig. 3.7:** Intersection of the Ewald sphere (radius $\left|\vec{k}_I\right|$) with the reciprocal lattice.

Reciprocal lattice points that lie on the Ewald sphere fulfil the Laue condition.

### ii) Image formation

In conventional TEM different image modes are chosen by inserting the objective aperture in the diffraction plane and thereby selecting only certain beams to contribute to the image. Depending on the chosen spot, two basic imaging modes are used. If the central spot (000-spot) is selected, which contains mainly unreflected electrons, a bright-field (BF) image is formed (Fig. 3.8a), and if any other spot (diffracted beam) is considered, a dark-field (DF) image (Fig. 3.8b) results. The dark-field method is for example used for determining the Burgers vector ($\vec{b}$) of dislocations using the relation $\vec{g} \cdot \vec{b} = 0$ [Williams, page 407]. For high resolution TEM (HRTEM), one uses objective aperture large enough to include several diffraction beams.

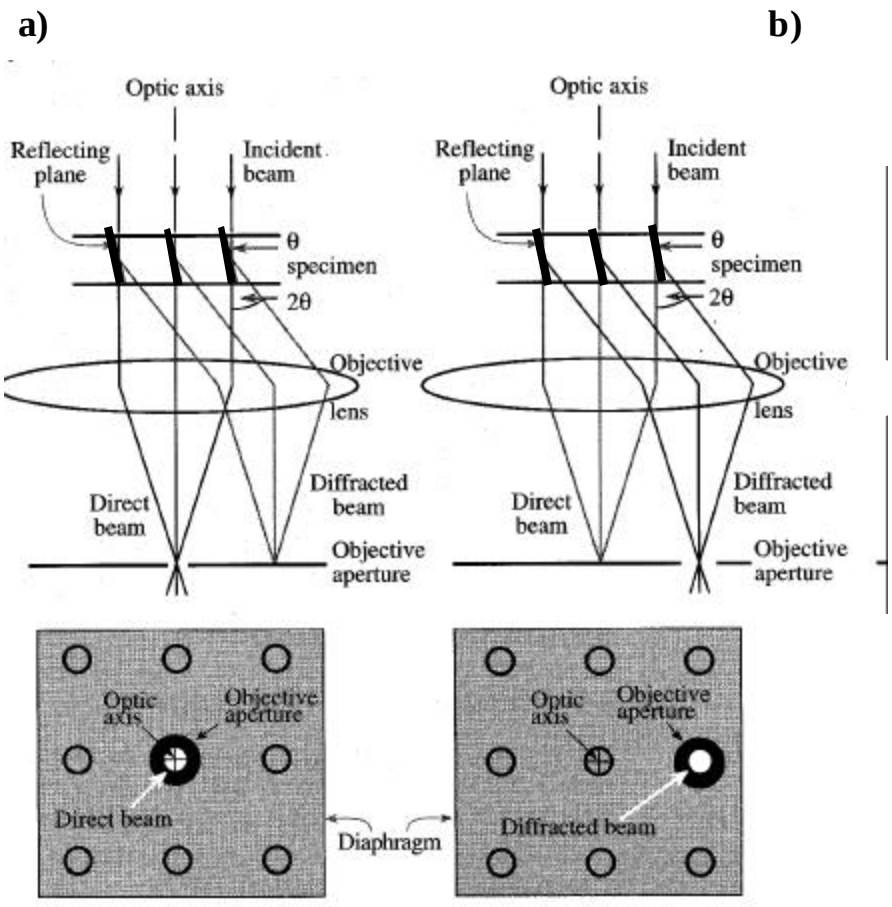


**Fig. 3.8:** Image formation in TEM by positioning of objective aperture in the back focal plane of objective lens by choosing **a)** the direct beam for the bright-field imaging or **b)** a diffracted beam for dark-field imaging (The planes being imaged are highlighted) [Williams, page 143].

### iii) X-ray Energy Dispersive Spectroscopy (XEDS)

By XEDS in a TEM the local chemical composition of the sample can be determined. The principle of XEDS is based on the following process: If more than a minimum amount of energy, the ionization energy, is transferred by an incident electron to a core electron (e.g. K shell), this electron is ejected from its shell, leaving a hole in the core. The resulting ionized atom can return to its lowest energy state by filling the hole with one electron from the outer shells (e.g. L shell). This transition is accompanied by the emission of a photon, with a kinetic energy equal to the energy difference of two electron shells involved (in this example, E(X-ray) = |E(K shell) – E(L shell)|). Since each element has its own electronic configuration and related energy levels, the detected X-ray emission from the sample is a direct evidence for the presence of a specific atomic species in the sample. The process of X-ray emission is shown schematically in Fig. 3.9.

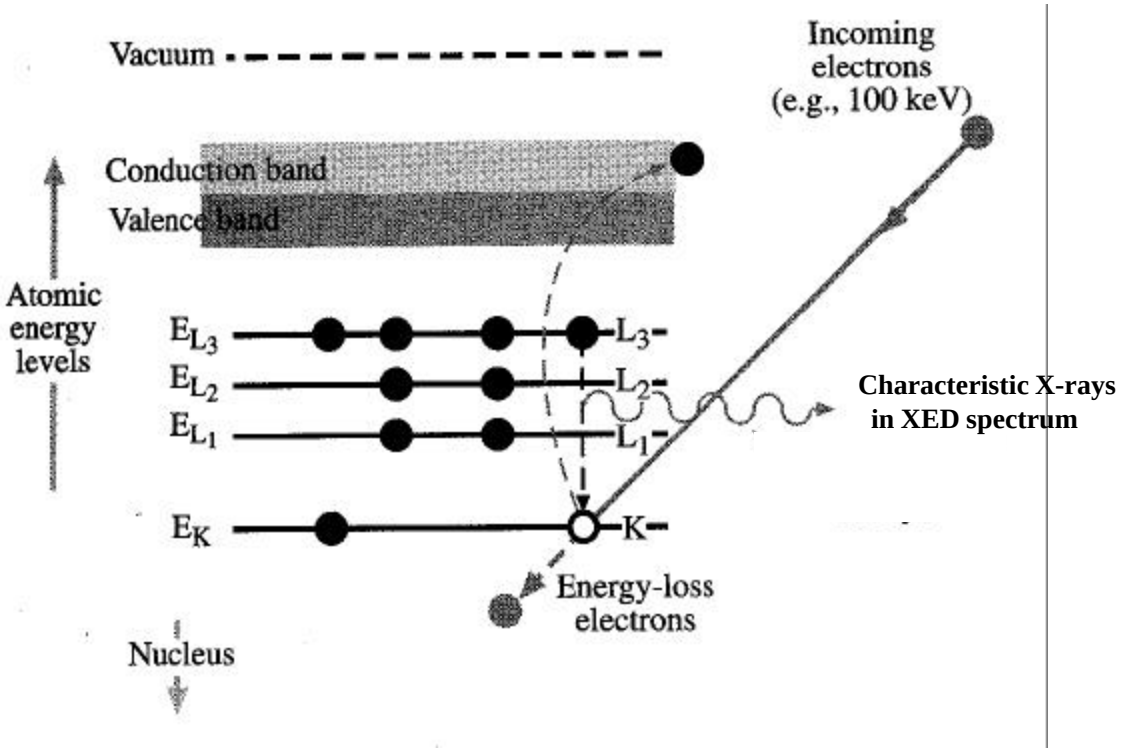


**Fig. 3.9:** The principle of XEDS: Characteristic X-ray ($K_\alpha$–line in this figure) produced by an ionization process. The energy of this emission is unique for each atomic species in the specimen.

An XED spectrum represents the intensity (photon counts) versus energy of the emitted X-rays. Peaks in the spectrum arise from the presence of certain elements in the sample. The XEDS spectrum of the bulk $SrTi_{0.95}Nb_{0.05}O_3$ sample investigated in this study (Fig. 3.10) shows all dominant peaks. For the chemical analyzis of reduced as well as reoxidized samples the following peaks are considered: Sr $K_{\alpha-}$line at 14.16 keV, Ti $K_{\alpha-}$line at 4.5 keV, and Nb $L_{\alpha-}$line at 2.16 keV.

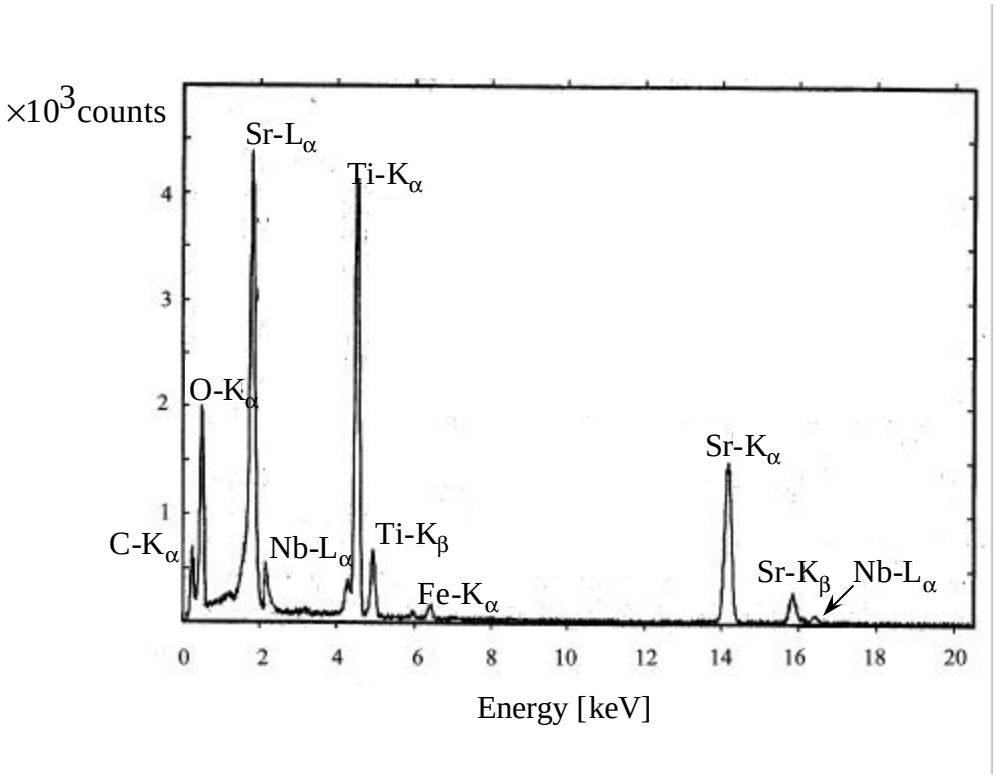


**Fig. 3.10:** XED spectrum of Nb-doped (5 mol%) $SrTiO_3$.

## 3.2 Impedance spectroscopy

The different electrical behavior of the bulk and the GBs in electroceramics materials (section 2.2) can be distinguished by impedance spectroscopy ([Bauerle, 69], [Denk, 97], [Abrantes, 20]). In this method an alternating current is applied to the sample and frequency–dependent resistance data are measured. For the evaluation of these data, bulk and GB are represented by two serial RC elements (resistor (R) in parallel with a capacitor (C)) (Fig. 3.11). The impedance (Z) of each RC element is

$$Z = \left(\frac{1}{R} + i\omega C\right)^{-1} = \frac{R}{1 + i\omega RC} \qquad (3.6)$$

(ω denotes the angular frequency) and yields one semicircle in the complex impedance plane (real impedance Z versus imaginary part) with R being the diameter of the semicircle. Each RC element exhibits a specific peak frequency known as ‘‘relaxation frequency’’ ($\omega_r$) and given by

$$\omega_r = \frac{1}{RC}. \tag{3.7}$$

This frequency corresponds to the maximum value of the imaginary part of the impedance. Because of the different contributions to the capacities of the bulk and the GB ($C_{gb} >> C_{bulk}$), the two RC elements usually have different $\omega_r$. In the following the existence of two semicircles in a typical spectrum of a polycrystalline material is explained. For low frequencies, the current has to pass both resistances and $R_{bulk} + R_{GB}$ results. Increasing of the frequency leads to a dielectric ‘opening’ of the large capacitance, i.e., $C_{gb}$ short-circuits $R_{gb}$, the impedance decreases and describes – due to the phase shift between the current and the applied voltage- an arc in the Z-plane that can be related to the GB. At medium frequencies, the impedance of the RC-element of the GB is negligible compared to that of the bulk and the impedance is just given by $R_{bulk}$. A further frequency increase, finally, opens the capacitance $C_{bulk}$ and causes a high-frequency arc related to the bulk. In this way, the impedances of the bulk and the GBs can be separated by varying of the frequency of the ac input signal.

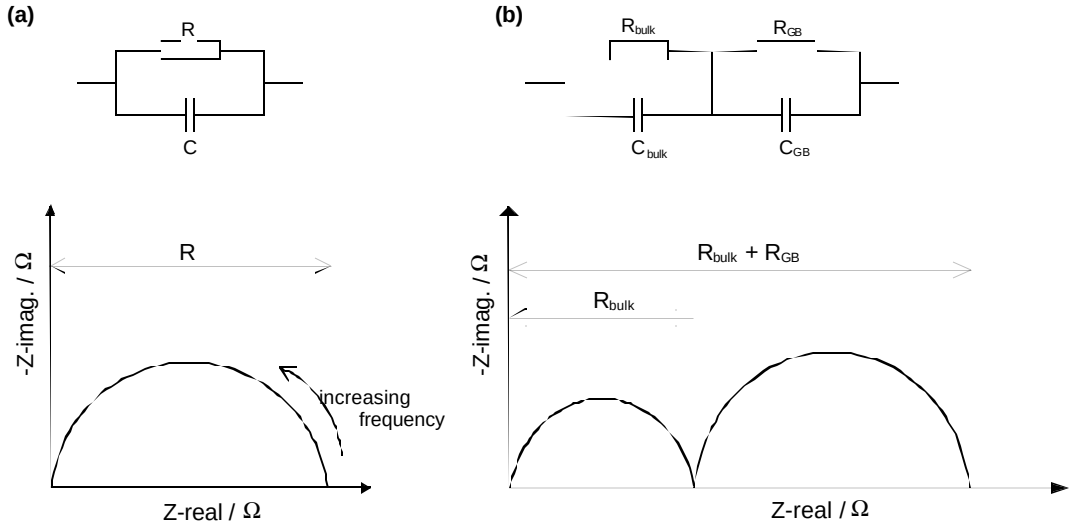


**Fig. 3.11:** Impedance spectra in the Z plane for **a)** one RC element and **b)** two RC elements related to bulk and GB contributions.

# Chapter 4

## Experimental

Owing to the following reasons polycrystalline **"Sr $Ti_{0.95}$ $Nb_{0.05}$ $O_3$"** specimens have been chosen for investigating the reoxidation behavior of donor-doped titanates.

**1)** Since the defect chemistry of titanates such as $SrTiO_3$, $BaTiO_3$ etc. are controlled by the same defect reactions [see chapter 2], reoxidation studies could be performed on donor-doped $SrTiO_3$ as well on donor-doped $BaTiO_3$. However, the ferroelectric property of $BaTiO_3$ at room temperature ($T_{Curie}$=130 °C) and the interaction of ferroelectric domains with the internal electric fields due to space charge layers located at GBs (Eq. 2.14), might affect the effects due to the reoxidation. Therefore, it is preferable to choose $SrTiO_3$ which exhibits paraelectric properties at room temperatures ($T_{Curie}$ = -55 °C) thus avoiding the above mentioned complications.

**2)** Preparation of a stoichiometric composition is of great importance. Otherwise, the existence of a secondary phase caused by non-stoichiometry may lead to additional complications (see section 2.3.1).

**3)** Polycrystalline samples make it possible to simultaneously study the oxidation behavior of different oriented surfaces.

In subsequent, the preparation route of $Sr\ Ti_{0.95}\ Nb_{0.05}\ O_3$ ceramics including powder preparation and sintering are introduced.

## 4.1 Preparation of polycrystalline $SrTi_{0.95}Nb_{0.05}O_3$ materials

Polycrystalline $SrTi_{0.95}Nb_{0.05}O_3$ samples were prepared by the so called mixed oxide route. Highly pure $SrCO_3$, $TiO_2$ and $Nb_2O_5$ powders (99.999% Fa. Aldrich) with particle sizes in the range of 1 µm to 5 µm were used as starting powders.

A mixture of these powders (10 g) are provided with a batch compositions of (7.93g) $SrCO_3$ + (4.08g) $TiO_2$ + (0.36 g) $Nb_2O_5$. The mixture was milled using dry zirconia balls in the planetary milling machine for 6 hours at the rotation speed of 130 rotations/min. The resulting powder represents a homogenous mixed powder with particle sizes of 250 to 300 nm. The powder is calcined at 1100 °C under air for 1 hour. Upon calcination, the mixed powder transforms into $SrTi_{0.95}Nb_{0.05}O_3$ perovskite single phase due to the following reaction:

$$SrCO_3 + (1-x)TiO_2 + (\frac{x}{2})Nb_2O_5 \rightarrow SrTi_{1-x}Nb_xO_3 + CO_2 \uparrow \quad (x = 0.05\ ). \qquad (4.1)$$

X-ray diffraction (XRD) analysis of the calcined powder confirmed the formation of the single phase perovskite (Fig. 4.1).

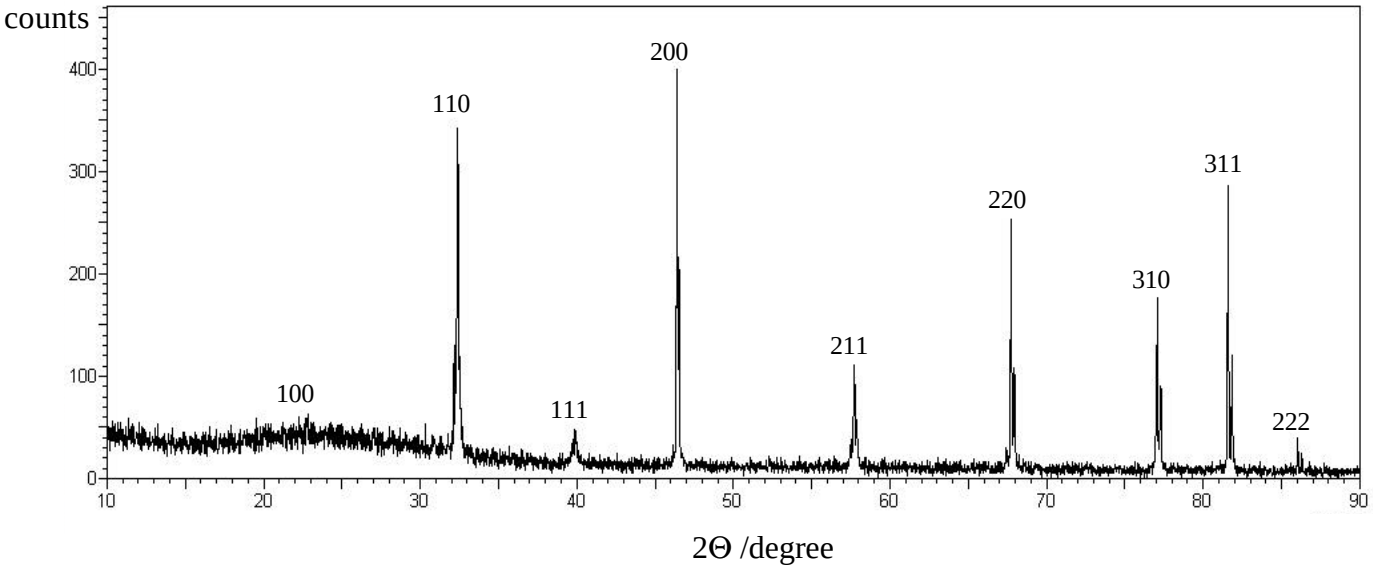


**Fig. 4.1:** XRD spectrum of the calcined powder $SrTi_{0.95}Nb_{0.05}O_3$. This spectrum fits very well to the spectrum known for perovskite phase $SrTiO_3$.

The calcined powder was ground again for one hour and a dense pellet of the powder (green body) is made by isostatic pressing under 680 MPa for 15-20 minutes. Afterwards, high temperature annealing under two different $p(O_2)$ is successively carried out. These are carried out as follows:

**1. Sintering under reducing condition:** The green compacted pellet is sintered at 1630 °C under a reducing atmosphere (a mixture of 5% $H_2$ and 95% Ar). In order to promote densification and grain growth, a long sintering duration (15 hours) and low heating and cooling cycles (50 °C/hours) were used for the sintering. Because of the low oxygen partial pressure of this gas-mixture at such a high sintering temperature (~ $10^{-20}$ bar), the resulting specimen is referred to as "reduced sample". A XRD analysis again confirmed the existence of a single phase perovskite structure after sintering.

**2. Secondary high temperature annealing:** The reduced sample was cut into slices of equal thickness of about 500 μm and one surface of each slice was polished to high optical quality (the details of preparation are noted in appendix A). The polished reduced samples experienced a second annealing at 1200 °C in oxygen atmosphere (1 bar) for 30 hours. In contrast to the slow heating/cooling rate for reduction (50 °C/hours ), a higher heating/cooling rate (600 °C/hour) was chosen for reoxidation.

## 4.2 Instruments

Morphological and structural aspects were investigated by different imaging methods such as optical microscopy (LEICA, DMRM), atomic force microscopy (AFM: MultiMode, Digital Instruments, in the contact mode), scanning electron microscopy (SEM: LEO 438VP) and transmission electron microscopy (TEM: JEOL 2000FX). The compositional changes upon reoxidation were determined by means of X-ray energy dispersive spectroscopy (XEDS) installed at the TEM and at STEM (VG HB501). For the determination of the different orientations of the crystallites of the polycrystalline sample, an orientation imaging (OIM) software program (TexSEM Lab.) interfaced to the SEM was used.

The sample preparation routes for each type of microscopic investigation are described in Appendix A. Electrical characterization of the reduced as well as the reoxidized samples were performed by impedance spectroscopy at room temperature. The impedance analyses were performed using an impedance converter combined with a Solatron 1260 frequency response analyzer in the frequency range from 1 Hz to 1 MHz. The applied electrodes and their preparation are introduced in Appendix A.

## 4.3 Characterization of the reduced polycrystalline $SrTi_{0.95}Nb_{0.05}O_3$ (reference sample)

### a) Microstructure

The reduced polycrystalline $SrTi_{0.95}Nb_{0.05}O_3$ sample (Fig. 4.2) exhibits a deep dark gray-color (see section 4.4b). The grain size varies from 20 to 200 μm. The occurrence of a bimodal grain size in polycrystalline samples is a well known problem if ceramics are prepared by the mixed oxide route ([Gülgün, 99], [Olsson, 89], [Blendell, 99]). This is mainly caused by the inhomogeneous particle size of the mixed powder obtained from dry milling. The density of the ceramic is 97% of its theoretical value. The composition of the sample determined by induction-coupled plasma analysis (ICP) is presented in Table 4.1.

Although the starting powders were of high purity (99.999%), a considerable level of unavoidable impurities is recognized. The impurities Zr and Si originate from the preparation procedure of the ceramics by using Zr-balls for milling and sea sand ($SiO_2$) for cleaning the milling components such as milling balls and the corresponding container (see section 4.1).

SEM (Fig. 4.2) and TEM investigations showed that the reduced sample was free of secondary phases.

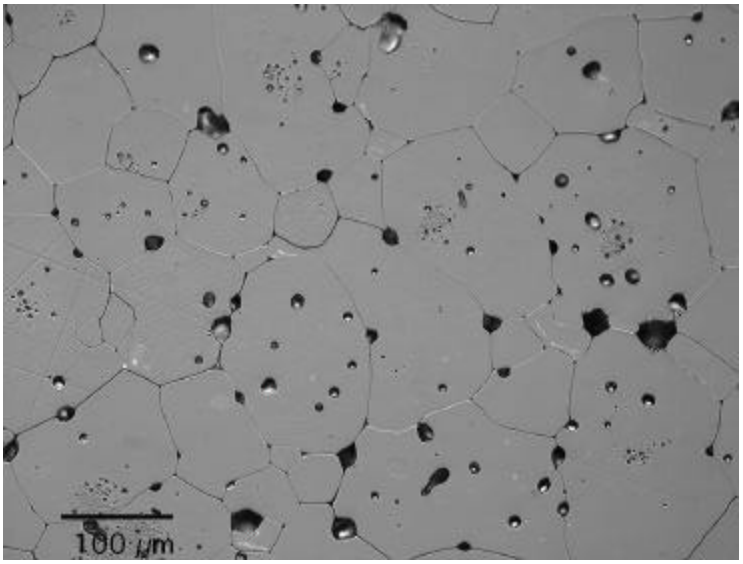


**Fig. 4.2:** Optical micrograph of the polycrystalline sample with the nominal stoichiometry of $SrTi_{0.95}Nb_{0.05}O_3$ sintered under reducing atmosphere.

**Table 4.1:** Composition of the sample derived from ICP analysis.

| Element | Sr | Ti | Nb | Si | Zr | Fe | Mn |
|---|---|---|---|---|---|---|---|
| (wt%) | 45.6±0.6 | 23.5±0.3 | 2.45±0.05 | 1.79±0.09 | <0.02 | <0.005 | <0.002 |

**Table 4.2:** Composition of the sample (at.%) considering only the main elements.

| **[Sr]** | **[Ti]** | **[Nb]** |
|---|---|---|
| (50.19±0.66) at.% | (47.3±0.6) at.% | (2.51±0.05) at.%. |

The resulting stoichiometry of the sample is:

$$\mathbf{Sr_{1\pm 0.01}\ Ti_{0.94\pm 0.01}\ Nb_{0.05\pm 0.01}O_3}$$

which is in good agreement with the nominal composition ($SrTi_{0.95}Nb_{0.05}O_3$). The lattice constant of the unit cell (a) of the reduced polycrystalline material determined by electron diffraction study is:

$$\mathbf{a_{\ reduced} = (3.855\pm 0.015)\ Å}$$

The smaller lattice constant of the reduced ceramic, compared to that of the pure $SrTiO_3$ (a = 3.905 Å, [JCPDS]), can be attributed to the high level of Nb doping (5 at.%) introduced to the samples. Considering the octahedral configuration of $TiO_6$, the replacing of $Ti^{4+}$ ions with the higher charged ions like $Nb^{5+}$ results in a stronger attraction between the anions and the cations and consequently leads to the contraction of the unit cell. Moos et al. [Moos, 97a] also reported a decrease of the lattice constant of single crystalline $SrTiO_3$ with increasing donor concentration (La).

### b) Electrical characterization of the reduced samples

The deep dark gray-color of the reduced polycrystalline $SrTi_{0.95}Nb_{0.05}O_3$ samples originates from the compensation of the donor doping by electrons (Eqs. 2.8, 2.9). The semiconducting behavior was examined by impedance spectroscopy. The measured very small dc resistance of 0.6 Ω may be caused by the connection wires.

# Chapter 5

# Topography of the Surface of Nb-doped polycrystalline $SrTiO_3$ after reoxidation

The mirror polished surface of reduced polycrystalline $SrTi_{0.95}Nb_{0.05}O_3$ samples exhibited dramatic topographical changes after reoxidation for 30 hours at 1200 °C. In the following these observations are reported and discussed in detail.

## 5.1 Island formation on the surface

A new phase appeared as islands on the surface of polycrystalline $SrTi_{0.95}Nb_{0.05}O_3$ (Fig. 5.1). The islands exhibit a pronounced facetting and a wide range of shapes: rectangular, triangular, trapezoidal or irregular and show nicely oriented surfaces. Shape, size, orientation and frequency of the islands vary strongly along the entire surface. According to AFM studies (Fig. 5.2), the lateral extensions of the islands are generally several micrometers. Their heights mostly vary in the range of few hundred nanometers.

The AFM studies reveal, besides islands, also droplet-like features on the surface (Fig. 5.3). The droplet-like microstructures, which do not show any faceting, lie either isolated on the surface or along the edges of the islands. Their lateral extension is about 150 nm and their height is about 20 nm. We suppose that droplets characterize the early stage of the islands, which grow during oxidation to the islands. Szot et. al [Szot, 99] also observed droplet-like features on (001) surface after annealing at 1100 °C for 24 hours. They proposed that prolonged annealing should lead to the agglomeration of these drops thus giving rise to larger islands.

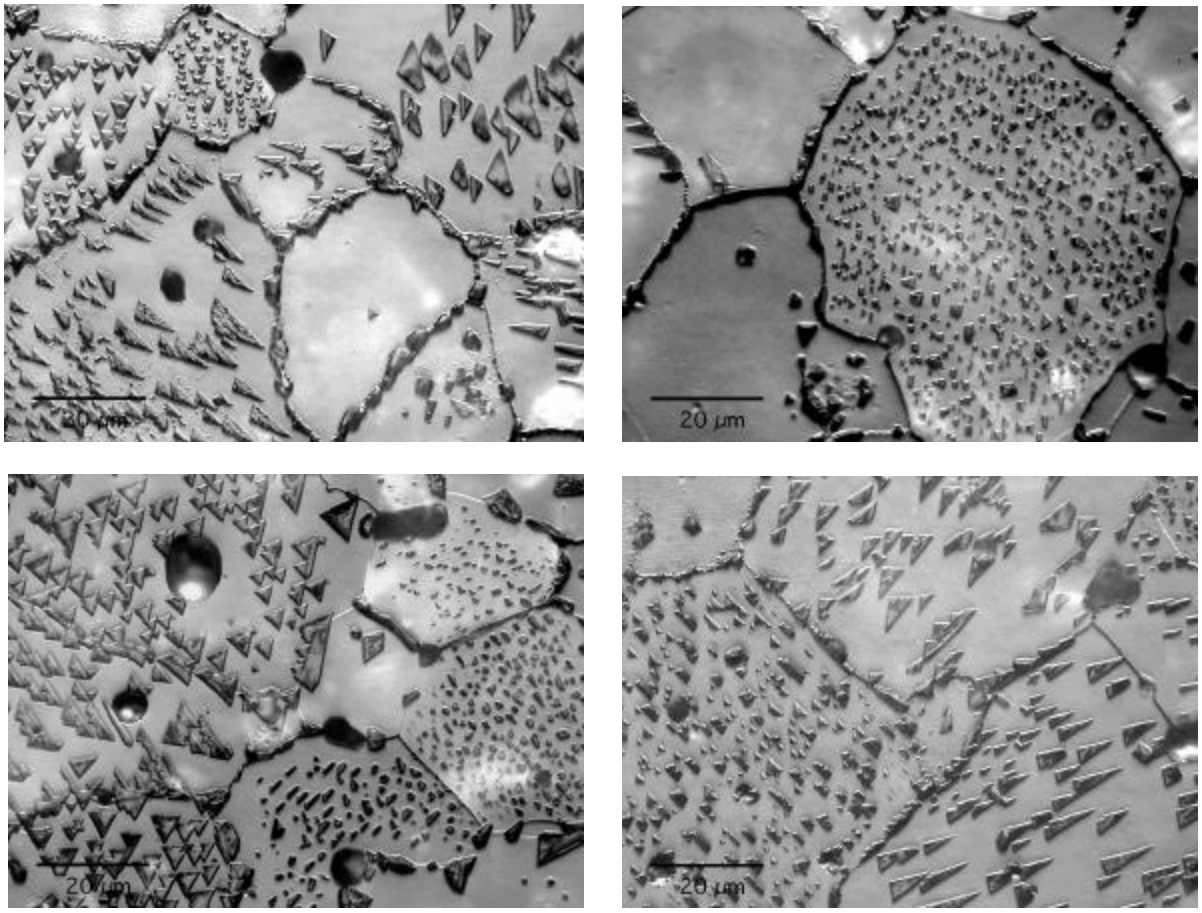


**Fig. 5.1.:** Optical micrographs of the reoxidized surface of polycrystalline $SrTi_{0.95}Nb_{0.05}O_3$ reveal islands on the surface. Islands exhibit different shapes, sizes, densities, and lateral directions on the different oriented grains.

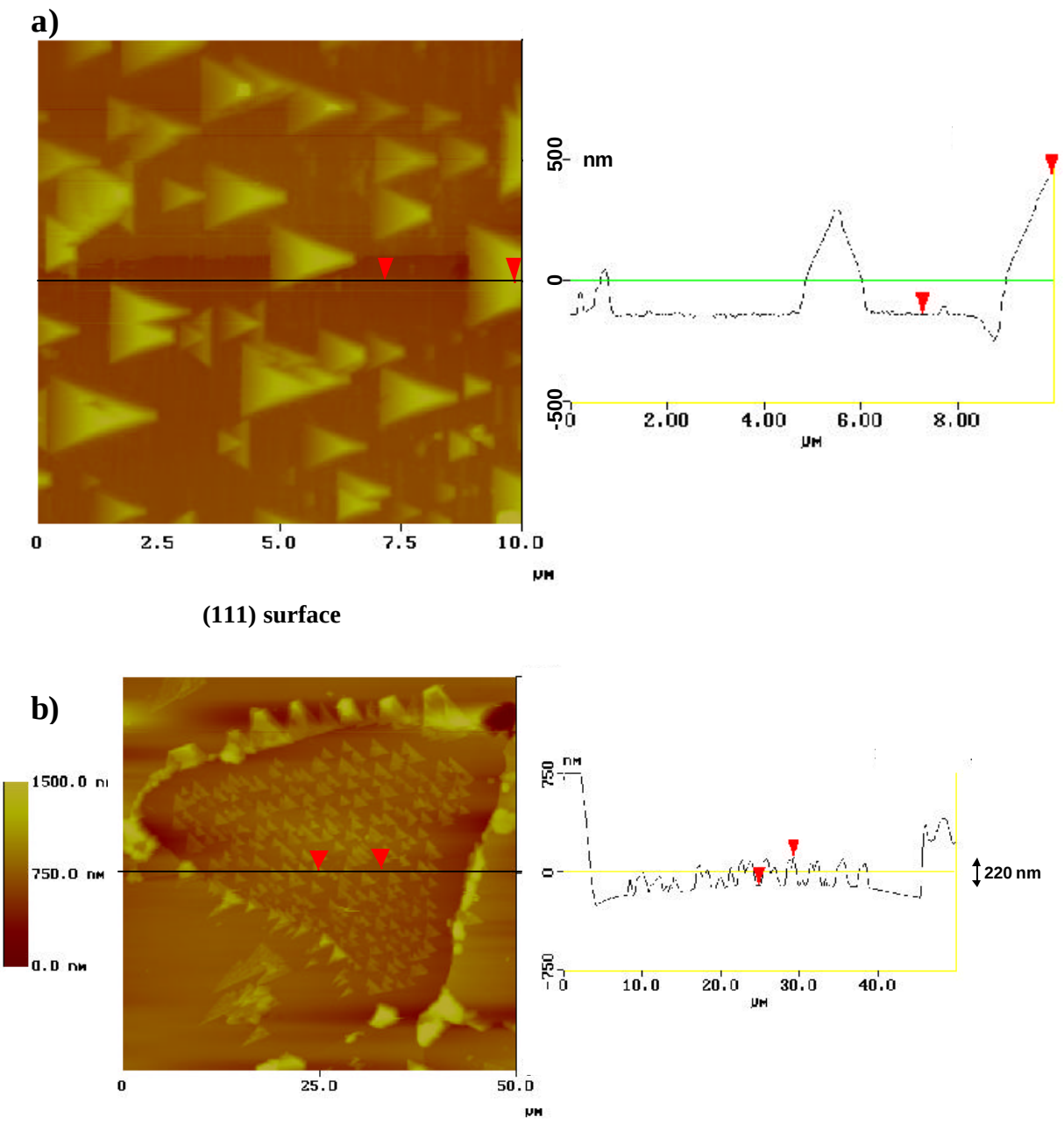


**Fig. 5.2:** AFM images of the islands **a)** on the (111) surface. The average height of the islands is about 500 nm. **b)** The height of the islands are markedly different on the grains and on the intersection of the GBs with surface. While the islands on top of the grains are generally only several hundred nanometers in hight, their heights in the GB region mostly exceed one micrometer.

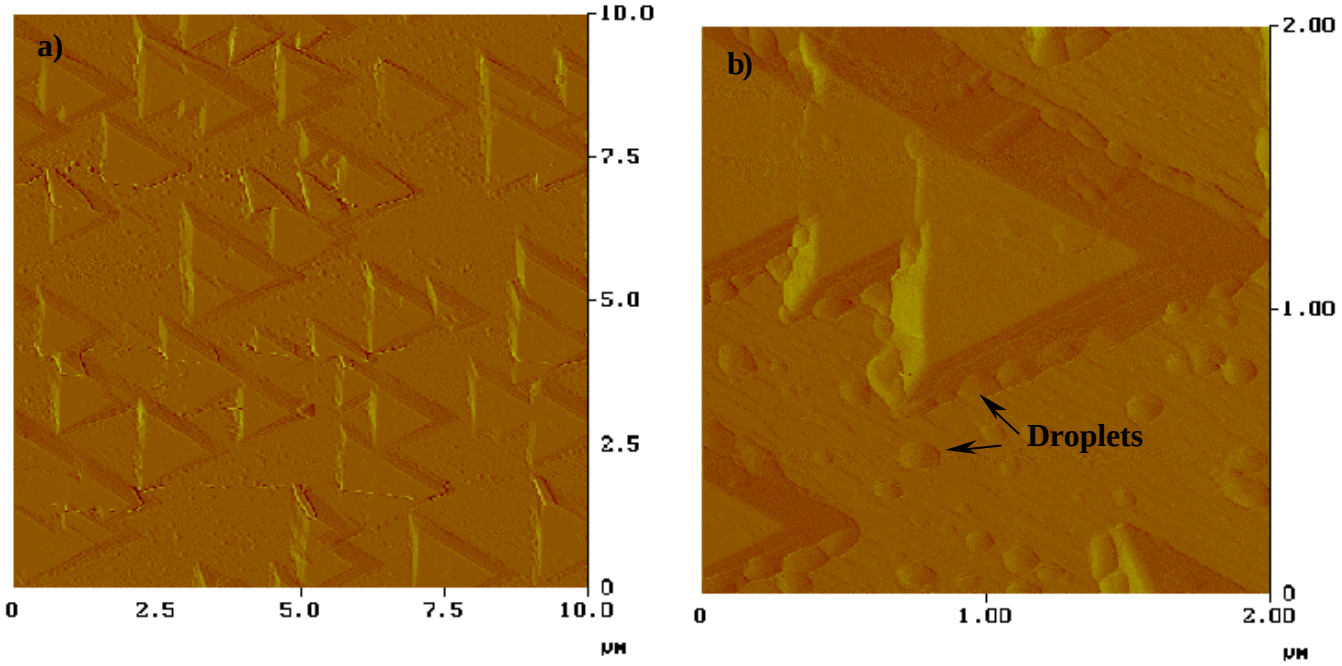


**Fig. 5.3:** AFM image of **a)** the islands with regular triangular shape and a height of about 200 nm (see Fig. 5.2b). The islands are rearranged in a trench structure. **b)** Higher magnification shows droplet like features indicating the initial stage of island growth.

## 5.2 Dependence of island density on the orientation of Surface

From the optical micrographs (Fig. 5.1), one can clearly recognize that the geometry, size, frequency, and lateral direction of the islands on top of the grains significantly vary from grain to grain. In order to find a correlation between these properties and the orientations of the corresponding grains, an OIM map of a large area of the reoxidized surface was generated. Figs. 5.4 and 5.5 show the optical micrograph (including 250 grains) and the corresponding OIM map ($400\times700\mu m^2$) of the surface of the reoxidized sample. The OIM map is based on 13600 local orientation measurements. The colours in the map indicate -via a stereographic triangle (Fig. 5.5, inset)- the orientations of the grains with respect to a reference direction (i.e. the normal direction of sample, which is [001]). Accordingly, the red color, for example, denotes the grains with their <001> direction aligned parallel to the reference direction. The result, which is partly represented in Fig. 5.6, reveals that different grain orientations prefer different island properties in terms of shape, lateral direction and frequency. In the following, the orientation dependency of the island frequency is discussed in more detail.

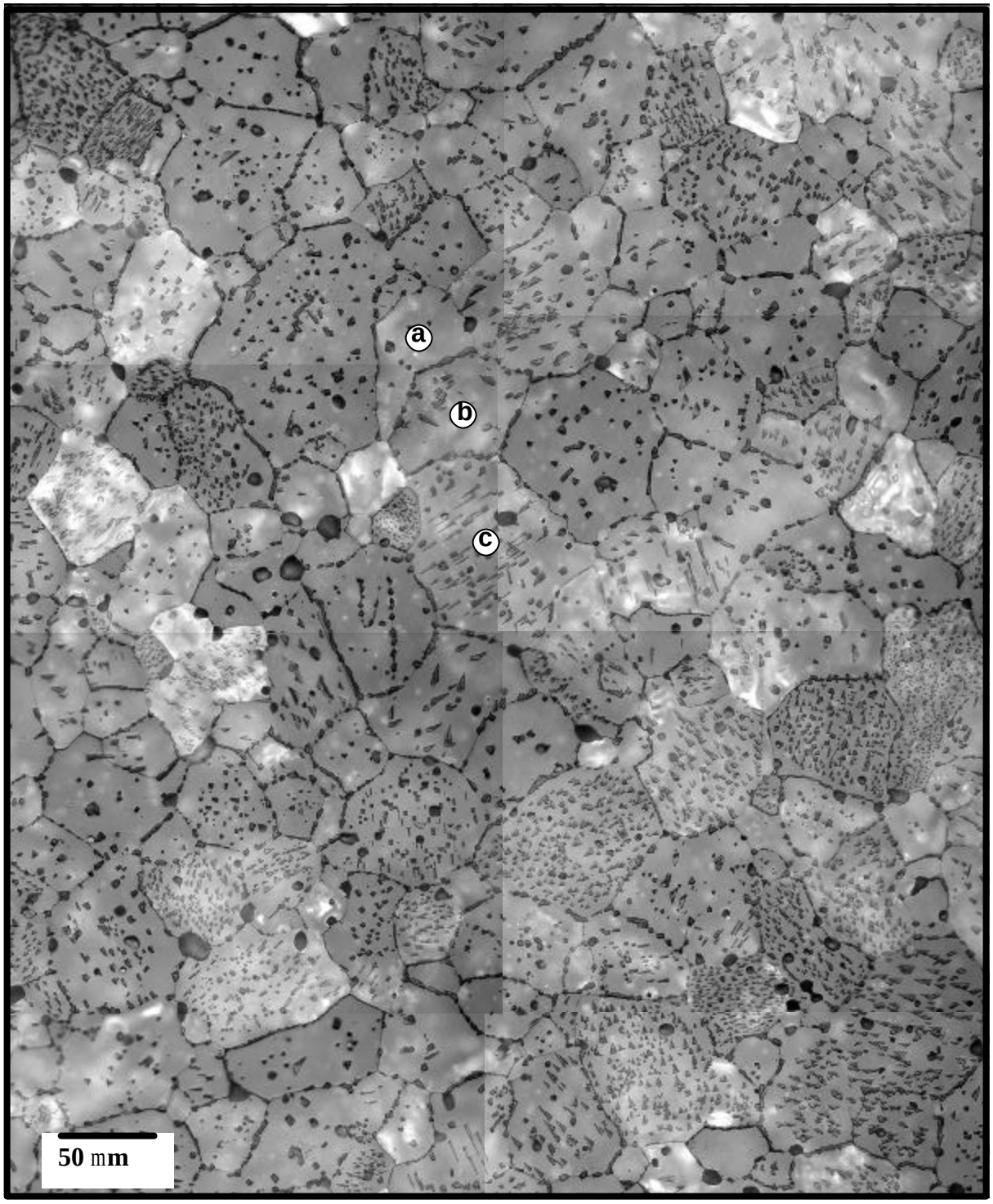


**Fig. 5.4:** Optical micrograph of the surface of polycrystalline $SrTi_{0.95}Nb_{0.05}O_3$ sample after reoxidation. The map includes more than 250 grains. The grains marked with '**a**', '**b**' and '**c**' are also indicated in the OIM map (Fig. 5.5).

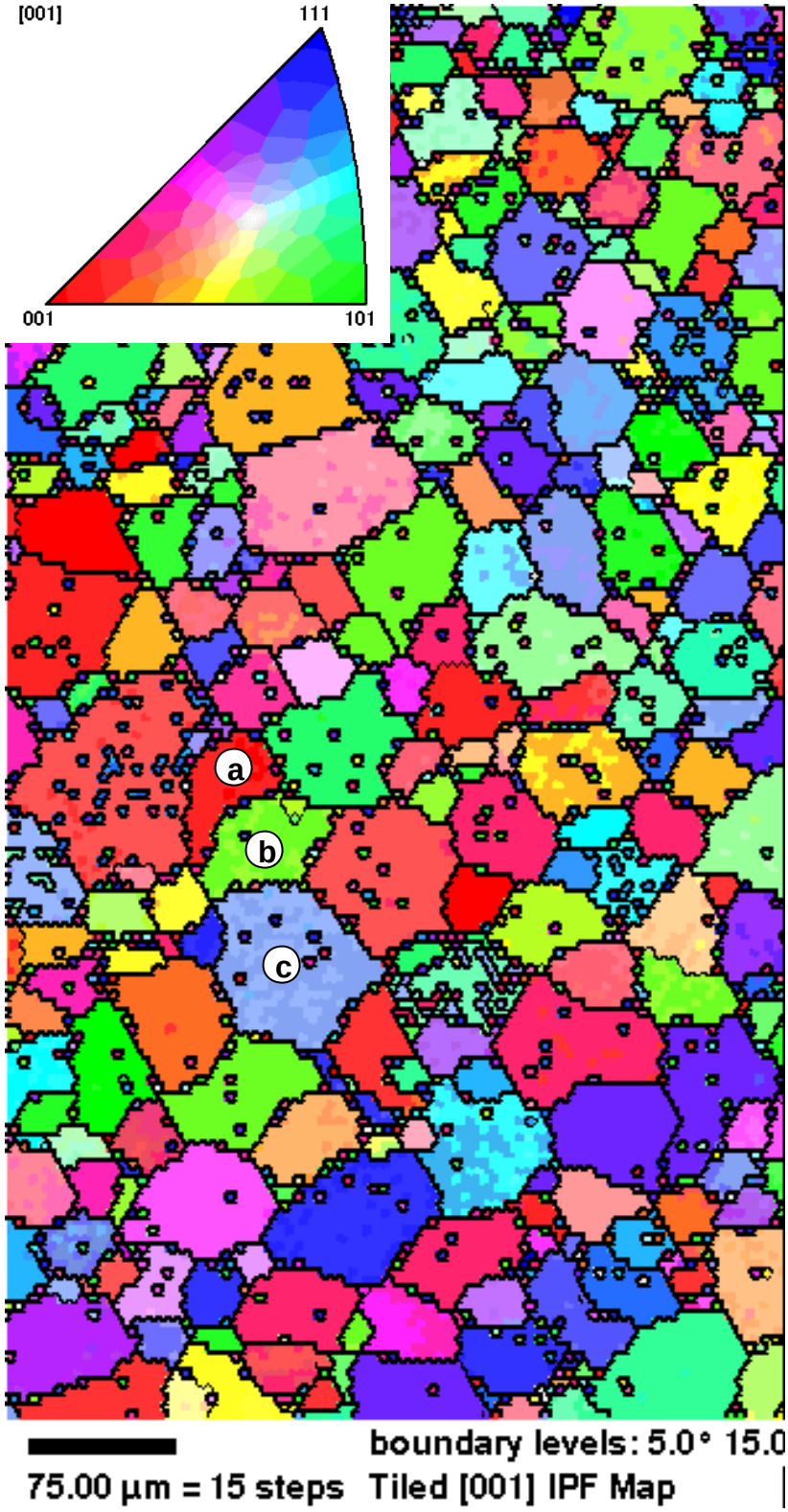


**Fig. 5.5:** OIM map of the reoxidized surface. The color of each grain is assigned to that in the stereographic triangle (inset) and represents the orientation of the grain. The correlation of the OIM map with the optical micrograph (Fig. 5.4) is visible via the marked grains as '**a**', '**b**' and '**c**'.

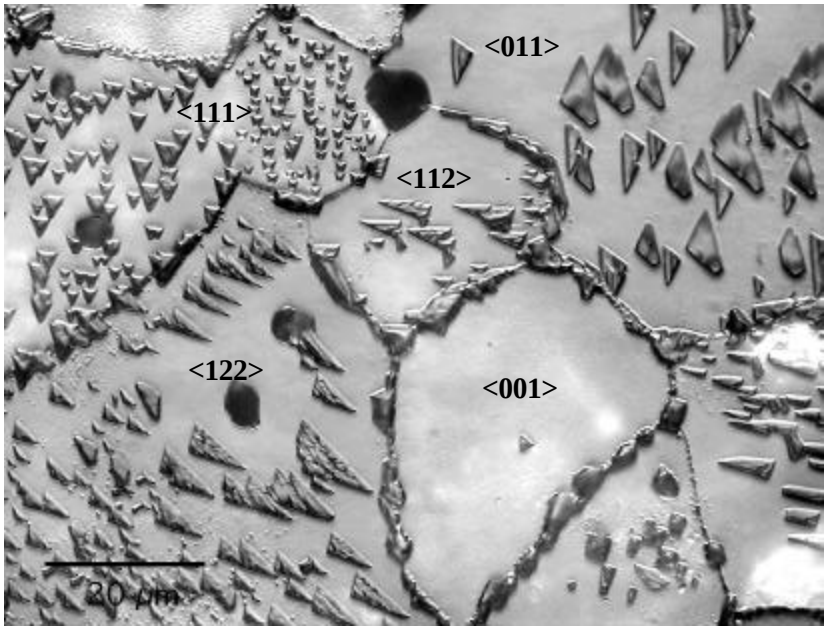


**Fig. 5.6:** Distribution of the islands on the surface of the reoxidized polycrystalline sample. The shape, the frequency and the lateral direction of the islands are characteristic for each kind of surface orientation. The surface orientations were determined from OIM measurements. Orientation deviations up to 5° were permitted.

The island frequency for a given surface orientation is expressed as the areal density of the islands ($\rho$ = area of all islands / total area of the underlying grain). This can be evaluated with the aid of a quantitative metallography software program (LEICA QWIN). The results are presented in a standard orientation triangle (Fig. 5.7), where the surface orientations are denoted as <*hkl*> and the related island density as $\rho$ (%). A clear correlation between the surface orientation and the island density can be found and can be described in terms of three levels of island density:

- A low island density ($\rho$ = 5%) is found for <001>, <013> and <114> surface orientations.
- A moderate island density ($\rho \cong 15\%$) results for <011>, <133> and <123> surface orientations.
- A high island density ($\rho \cong 20–30\%$) can be related to <111>, <112>, <122> surface orientations.

The island densities of all investigated surfaces are included in Fig. 5.7. It turns out that for those surface orientations which deviate by less than 20 degrees from one of the main surfaces, i.e. surfaces locating at the corners of the orientation triangle, the island density is nearly constant (only <012> deviates from this rule). For example, the island density for the {112} and {122} surfaces is (22±3)% and (21±4)% respectively, which are close to the density of the {111} surface which is (27±5)%. The {114}, {013} surfaces locating close to the <001> orientation, on the other hand, are much less densely covered with islands (5±2%). There seem to be very sharp boundaries separating at least three groups of surface orientations with respect to the island formation.

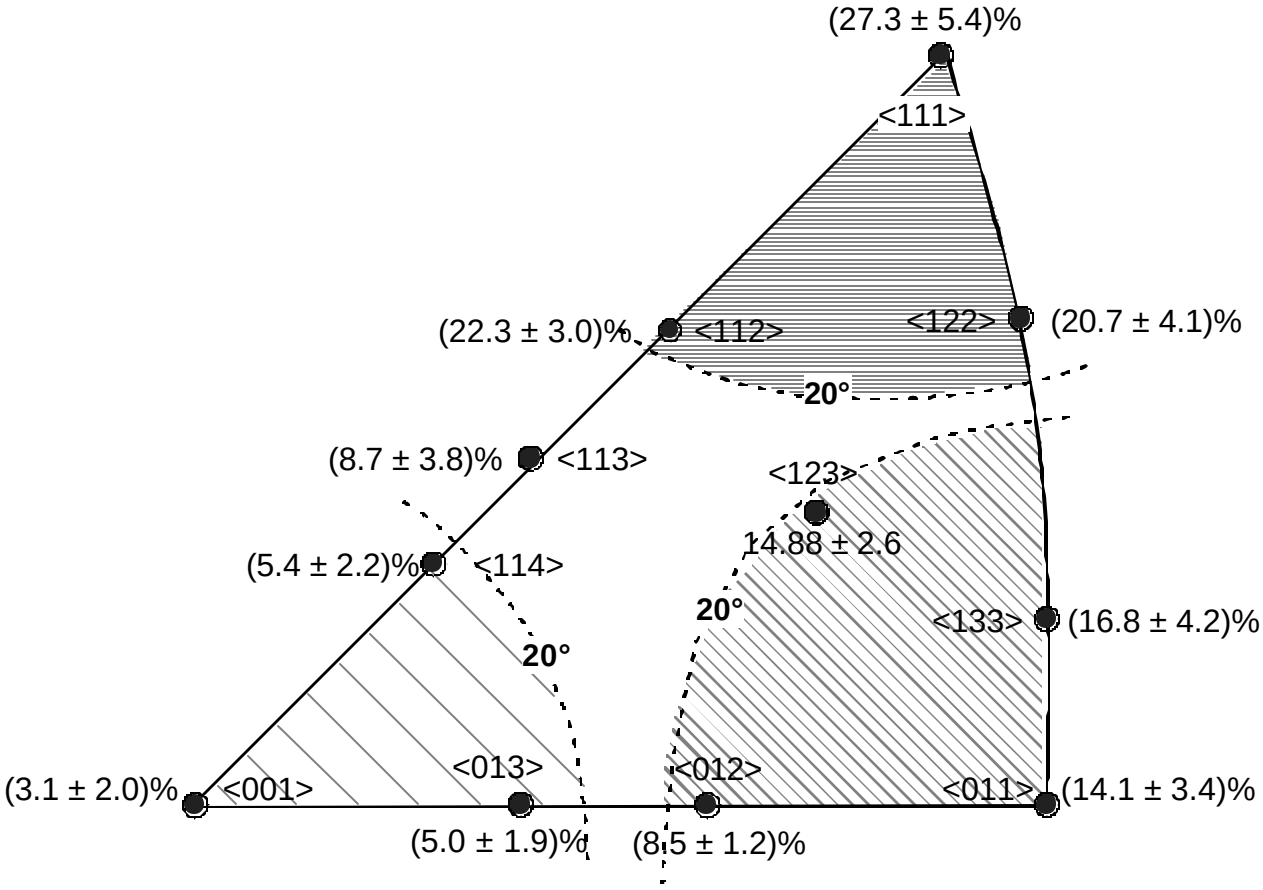


**Fig. 5.7:** Dependence of the island density on the surface-orientation. Different orientations of the surface are presented in the standard orientation triangle. The surfaces are classified in three orientation regions with similar island density (striped regions) (island density of (012) surface deviates from this classification). Each region consists of a main surface (located at the corner of the orientation triangle) and the surfaces with orientation deviations up to 20°. (113) surface was not classified. Orientation deviations up to 5° were permitted.

## 5.3 Preferential lateral orientations of the islands

The optical micrographs (Fig. 5.1) show that the islands are faceted and have characteristic orientation relationships with respect to the surface orientation of the underlying grains. The facet orientations are determined for the three basic surface orientations, i.e. (001), (011), (111) by OIM and are sketched in Fig. 5.8. In each case the crystallographic orientation is shown below the images as it was obtained from OIM measurements. These contain the surface orientation indicated by [*hkl*] and two in-plane vectors denoted by [*uvw*] and [*pqr*]. It is worth mentioning that these orientations might deviate from the ideal orientations up to ±5 degrees which was the 'acceptance range' in the OIM measurements.

A reason for the very specific relation between island faceting and surface orientation can not be given yet.

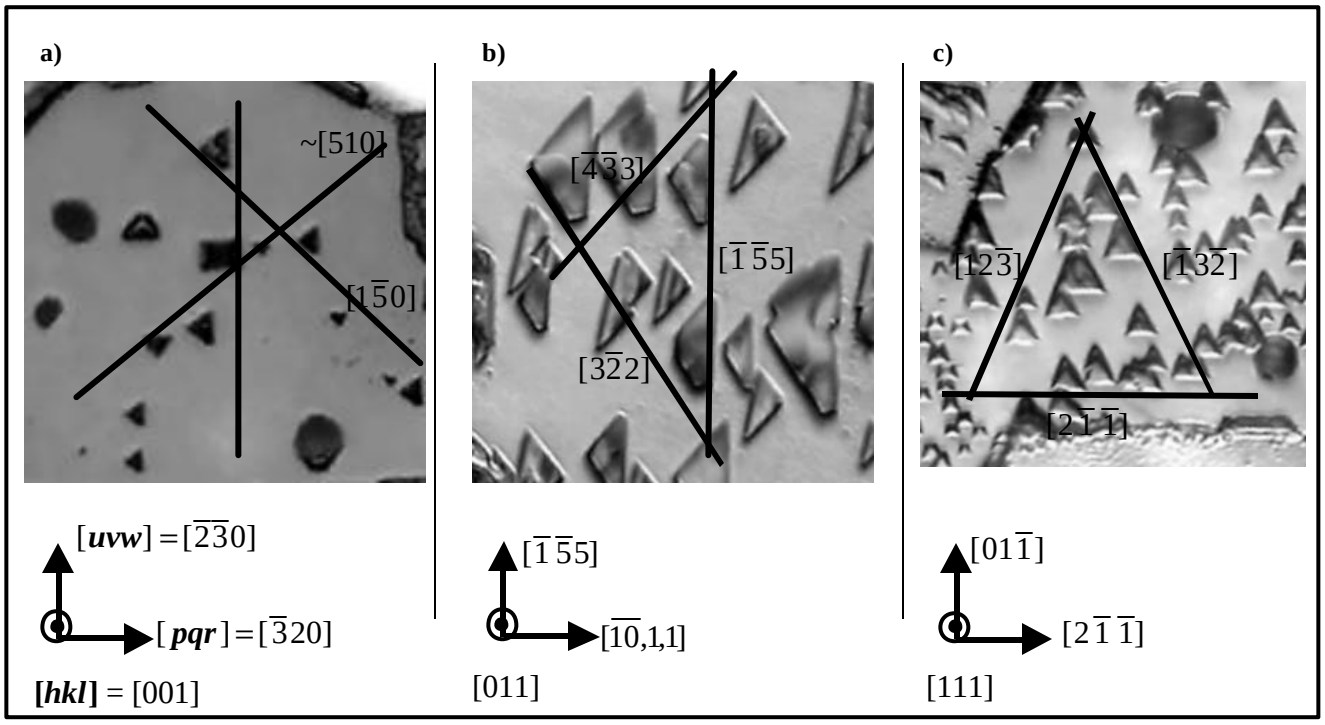


**Fig.5.8 :** Common lateral directions of the islands on the **a)** <001>-surface, **b)** <011>-surface and **c)** <111>-surface. Direction deviations up to 5° were permitted.

## 5.4 Island formation on the grain boundaries

As it was shown in Fig. 5.2, the island formation takes place on top of the grains of the polycrystalline sample as well as along the intersection of the GBs with the surface. The density of islands along the GB intersections is very inhomogeneous. Often the GBs are completely covered by islands while other GBs are completely free of islands. To find a connection between the type of the GBs (small angle and large angle GBs) and the corresponding island formation tendency, OIM measurements were performed. For this reason, three types of GBs are distinguished depending on the misorientation of the neighboring grains. These are small angle GBs (SAGB), coincidence site lattice boundaries (CSL) and general GBs ($\Sigma$>50).

The different tendency of GBs for island formation is classified qualitatively in the four categories: strong (S), partial (P), weak (W) and immune (I). As an example Fig. 5.9 examplifies this categorization. A summary of all experimental data are given in Appendix B (Table B1). More than 100 GBs were evaluated based on the OIM map (Fig. 5.5) and the corresponding optical micrograph (Fig. 5.4). As it is expected for ceramics materials, the majority of the investigated GBs are of the general type [Chiang, 97]. However, no systematic relation is found between the misorientation of the neighboring grains and the oxidation behavior of the corresponding GB. This could probably be due to the fact that by OIM only the misorientation of the corresponding grains is measured but not the inclination of the GB planes (the direction of the normal vector to the GB plane). However, it remains to be shown that the inclination of the GB planes plays the same decisive role in the island formation as in the case of the surfaces (section 5.2).

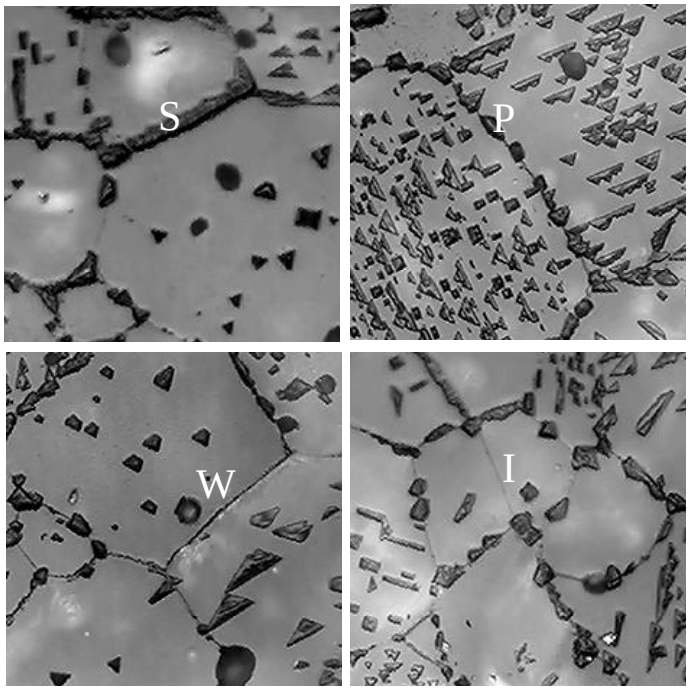


**Fig. 5.9:** Different island formation tendencies along the intersections of the GBs with the surface: strong (S), partial (P), weak (W), and immune (I).

## 5.5 Interpretation of island formation

Obviously the process of reoxidation leads to the formation of secondary phases on the surfaces. We assume that the early stage of the secondary phase formation is characterized by droplet-like features which do not show any facetting. The coalescence and the growth of the droplets during reoxidation then leads to the islands. Such an island formation on the surface of single crystalline $SrTiO_3$ after annealing at high temperatures under reducing as well as oxidizing atmosphere is reported by several groups (see Table 2.2). Our studies, however, show for the first time that the areal density of the islands significantly depends on the surface orientation of the grains. If the island density ($\rho$) is used as an indicator for the oxidation tendency of a surface, the following conclusions can be drawn for the three main surface orientations:

- The <001> surface shows the lowest oxidation tendency ($\rho \sim 3\%$ ).
- The <011> surface has a moderate oxidation tendency ($\rho \sim 15\%$).
- The <111> surface exhibits the highest oxidation tendency ($\rho \sim 30\%$).

This can be understood in terms of the different polarities of the surfaces. Since polar surfaces are characterized by a high surface energy, the process of surface oxidation, i.e. the formation of a second phase, can lead to a reduction of the surface energy. This interpretation is based on thermodynamic and considers the energetic changes upon secondary phase formation. Another reason for the different reoxidation behavior might be related to the kinetics of the reoxidation reaction (Eq. 2.12). This reaction includes gaseous ($O_2$) and ionic species ($Sr^{2+}$) as well as electrons and the reaction rate can strongly be influenced by the chemical potentials at the surface and the energy of electronic surface states.

The (111) surface of $SrTiO_3$ is a highly polar surface due to the charged uppermost layer ($(SrO_3)^{4-}$- or $Ti^{4+}$-termination of the surface, Fig. 2.6) which results in a high surface energy and can thus be expected to exhibit a high oxidation tendency. This is confirmed by the experiments. The close-packed arrangement of $Sr^{2+}$ and $O^{2-}$ ions in the (111) plane may also enhance the reactivity of this plane. On the other side, the (001) surface is a non-polar surface (SrO or $TiO_2$ termination, Fig. 2.6) and thus exhibits a lower surface energy and therefore lower oxidation tendency. Concerning the (110) plane, there is a higher net surface charge compared to the (001) surface but a lower one compared to the (111) surface, which may explain the moderate oxidation tendency of this surface. The oxidation tendency of any other surface can be predicted by determining the orientation neighborhood of this surface to a main surface (misorientations up to 20°). Then, the given surface shows the similar island formation tendency as the main surface.

A more quantitatively relation between island density and surface energy can be given by comparing the data measured here with experimentally determined surface energies of $SrTiO_3$ at 1400°C in air [Sano, 03]. As can be seen in Fig. 5.10 a fairly good accordance between both studies results. Plotting the island density versus the surface energy (Fig. 5.11) again points to a direct relationship between the surface energy and the island density and thus the oxidation tendency.

Hence this study reveals a quantitative estimation of the island formation tendency for differently oriented surfaces in polycrystalline $SrTiO_3$ reoxidized at 1200°C.

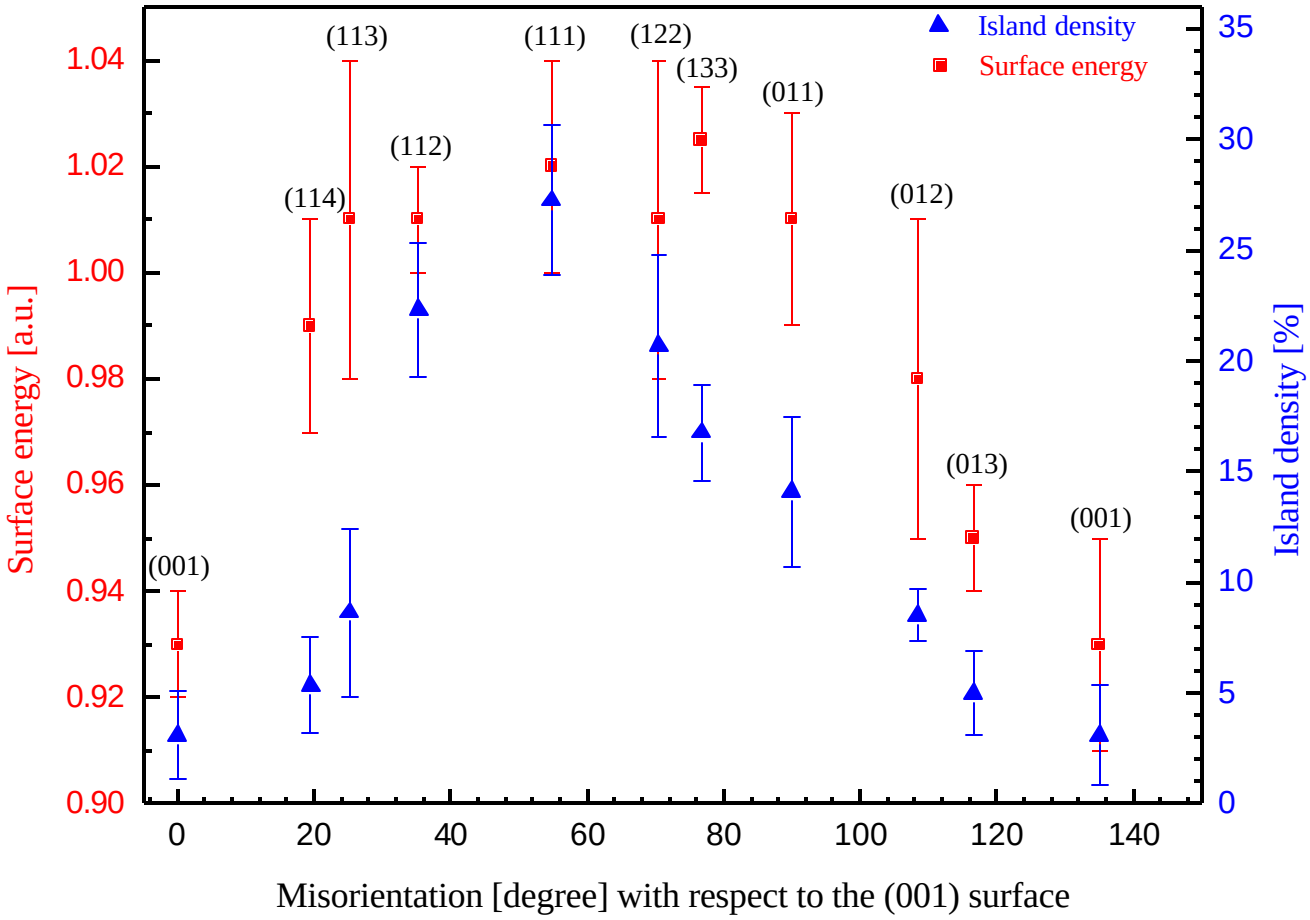


**Fig. 5.10:** Comparison of the orientation dependency of the island density (from this study) with the orientation dependency of the surface energy measured by using capillary vector reconstruction method [Sano, 03]. The plots are around the perimeter of the standard stereographic triangle, from (001) to (111), then to (011), and back to (001) (see Fig. 5.7).

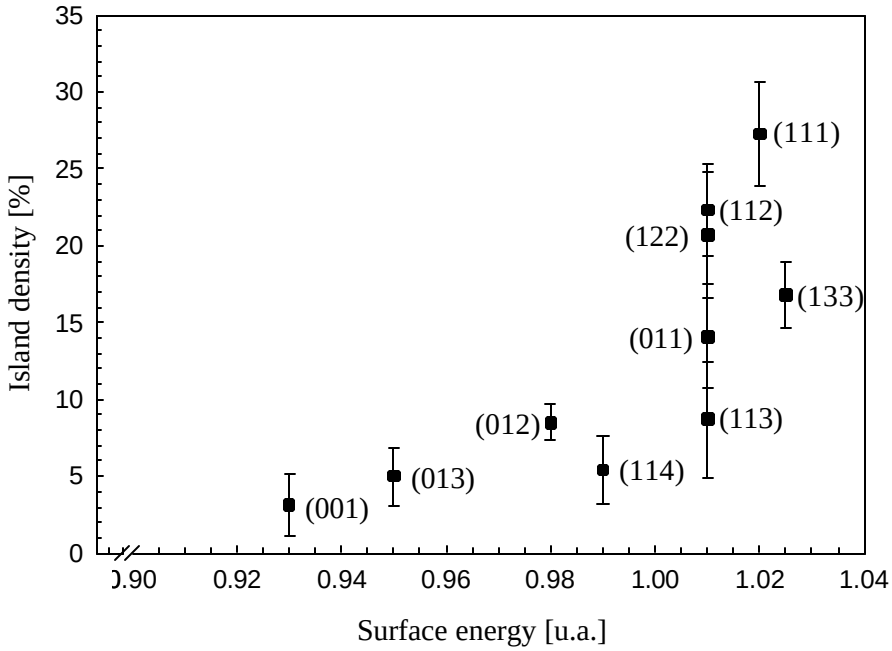


**Fig. 5.11:** The relation between island density and surface energy [Sano, 03]

## 5.6 Structure and composition of the islands

TEM investigations was performed on cross-sectional TEM specimens of the islands allow us to study the structure and chemical composition of the islands by application of electron diffraction and EDX, respectively. TEM preparation of islands for specific surface orientations of a polycrystalline sample is extremely difficult. In addition, the different ion milling rate of the islands compared to that of the substrate made the TEM preparation particularly difficult. Therefore the surfaces on which islands are investigated, i.e., $(\bar{2}30)$ and $(\bar{1}20)$ surfaces, are not deliberately chosen but resulted by accident.

### 5.6.1 Islands on the $(\bar{2}30)$ surface

The TEM micrograph (Fig.5.12) shows two islands with different heights on top of the $(\bar{2}30)$ surface. The larger island reveals a height of 200-250 nm and the smaller one has a height of 40 nm.

#### a) Electron diffraction study of the $(\bar{2}30)$ island

The diffraction pattern of the larger $(\bar{2}30)$ island resulted from the whole area of the island (the applied SAD aperture at TEM JEOL 2000FX was 320 nm in diameter). The diffraction patterns could be taken in [001] and [111] projections. The SAD patterns (Fig. 5.12b, c) revealed that the island is ‘‘single-crystalline’’. In addition, the absence of super-reflections in these patterns is an indication for the absence of a secondary phase in the island.

The almost identical electron diffraction patterns in the [001] and [111] projections obtained from the larger island (Fig. 5.12b,c) and the bulk (Fig. 5.12a, d) directly beneath the island, suggest the same crystallographic structure for both the island and the bulk.

The main difference between the SAD patterns of the island and the bulk can be recognized as the different intensities of the 100 reflections, which are weaker in the bulk than in the island. This difference could be an indication of a change of site-occupancy in the lattice of the island compared to the bulk. This suggestion will be further discussed by means of XEDS measurements (section 5.6.1b). However, we can also not exclude that this difference is caused by a thickness difference between bulk and island, although this is not very likely because the two diffraction patterns were taken from regions very close to each other.

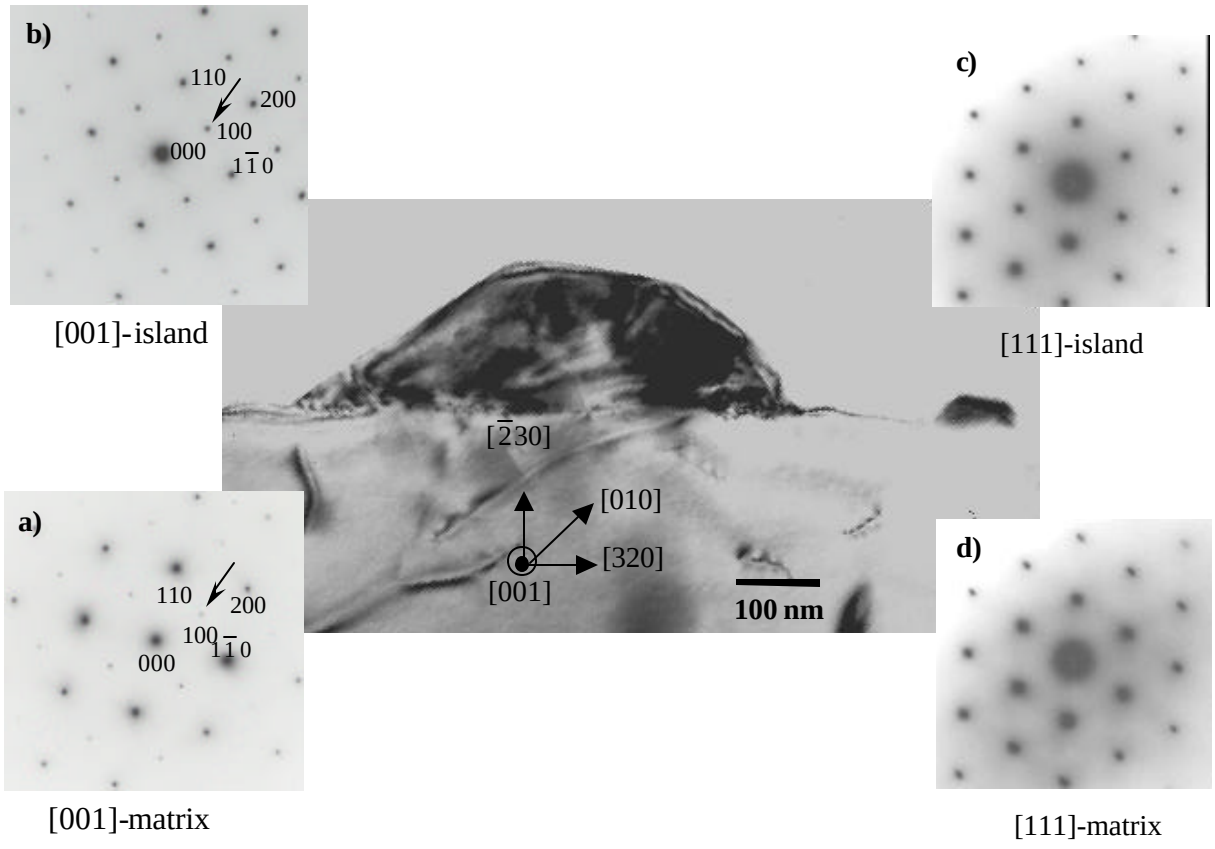


**Fig. 5.12:** Bright-field TEM micrograph ( $\vec{g} = 0\bar{2}0$ ) of the cross section of the islands. Electron diffraction pattern in [001]- projection from **a)** the bulk and **b)** the "larger" island. Electron diffraction pattern in [111]-projection from **c)** the island and the **d)** bulk.

The lattice constants of the island ($a_{island}$) and the region beneath the island ($a_{beneath\ island}$) evaluated from the related diffraction patterns are

$$a_{island} = (3.911 \pm 0.01)\ \text{Å} \quad ; \quad a_{beneath\ island} = (3.902 \pm 0.01)\ \text{Å}$$

The lattice mismatch between the island and the region beneath the island is thus

$$\frac{a_{island} - a_{beneath\,island}}{a_{beneath\,island}} = (0.23 \pm 0.014)\%$$

and suggests, in conjunction with same crystal structure of the island and the bulk, an epitaxial growth of the islands.

### b) Chemical composition of the ($\bar{2}30$) island

Successive chemical analyses was performed by using XEDS(STEM) perpendicular to the surface and in the growth direction of the island. The XED spectra were gathered from an area of 3×4 $nm^2$. The investigations reveal a gradual increase of the Sr and simultaneously a gradual decrease of the Ti concentration in the growth direction of the island (Fig. 5.13). While the bottom of the island (near the island/bulk interface) shows a slight Sr excess ($Sr/(Ti+Nb) = 1.124 \pm 0.2$), the top of the island contains mainly Sr cations ($Sr/(Ti+Nb) = 9.2 \pm 2.3$). The concentration of Nb seems to be constant within the experimental error.

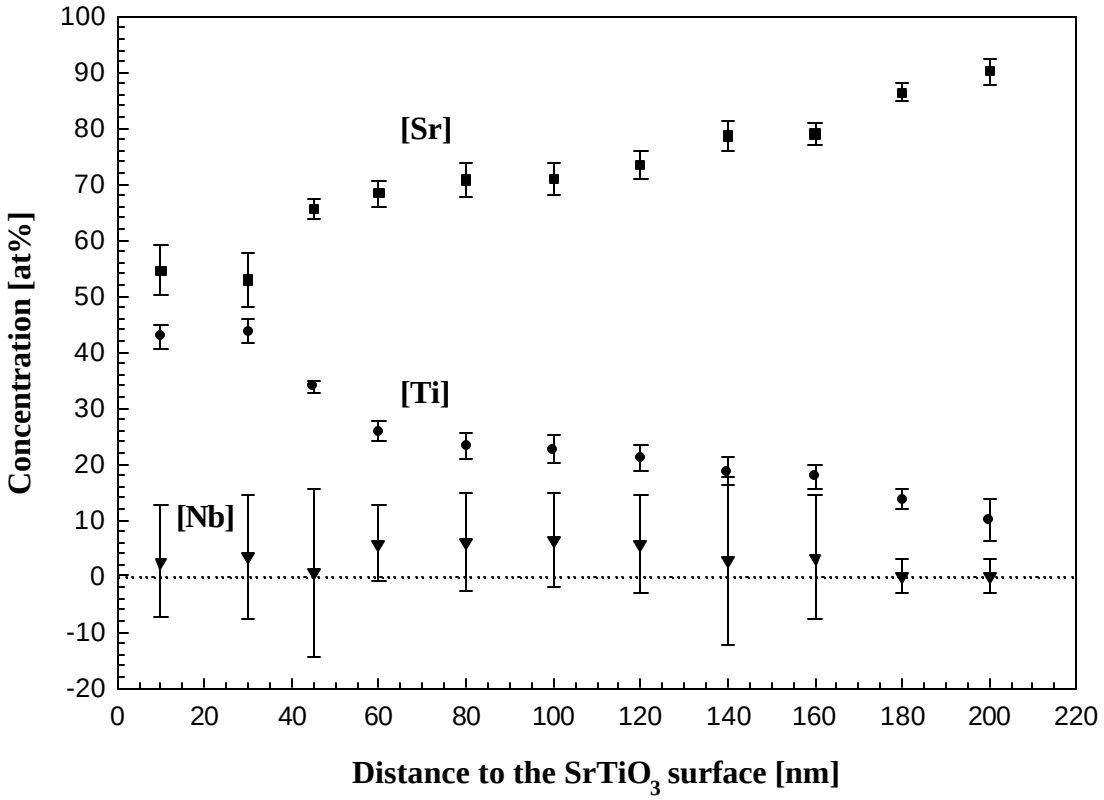


**Fig. 5.13:** Composition profile of the island (larger island in Fig. 5.12) in the growth direction derived from successive XEDS(STEM). The spectra were gathered from an area of 3×4 $nm^2$.

An extrapolation of the Ti concentration versus island height (Fig. 5.14) indicates a penetration depth for Ti ions into the island of about 230 nm which is approximately the length of the island.

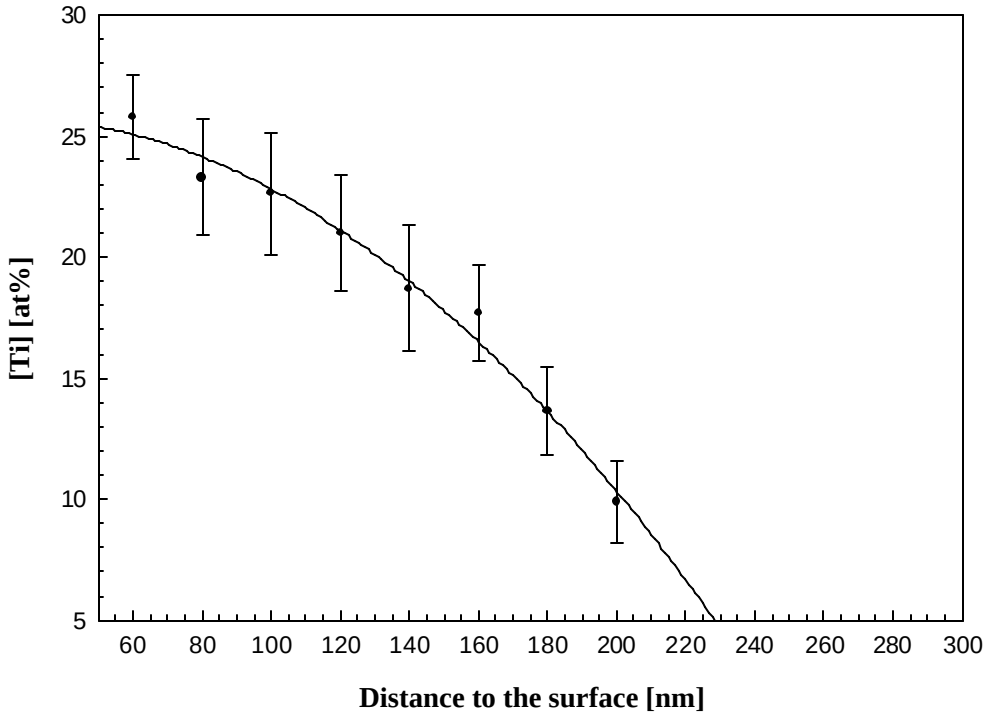


**Fig. 5.14:** Extrapolation of the Ti concentration over the island height. The fitting curve is a second order polynomial. The abscissa value of the fitting curve is 230 nm.

## c) Discussion of the island structure on the ($\bar{2}30$) surface

Considering the XEDS results (Fig. 5.13), the following scenario is suggested for the growth, chemical composition and structure of the island: Close to the $SrTiO_3$ surface (up to about 40 nm), the island is composed of pure $SrTiO_3$. With increasing island height, the $Ti^{4+}$ content decreased gradually by substituting $Ti^{4+}$ ions by $Sr^{2+}$ ions but leaving the perovskite lattice structure unperturbed. This results in an increase of $Sr_{Ti}^{''}$ defects and the composition of the island $Sr_1Ti_{1-x}(Sr_{Ti}^{''})_xO_{3-x}$, which requires $V_O^{\bullet\bullet}$ in order to maintain the charge neutrality condition.

The identical diffraction patterns of the island and the matrix with only the changing of the

spots-intensities of the electron diffraction pattern from the matrix into the island (Fig. 5.12a, b) and also the slightly larger lattice constant of the island compared to the matrix beneath the island (ca. 0.2%, see section 5.6.1a), also support the suggestion of substitution of the smaller $Ti^{4+}$ by larger $Sr^{2+}$ ions. Close to the surface of the island, $Ti^{4+}$ ions are almost completely replaced by $Sr^{2+}$ cations (x=1) and thus a strontium oxide results that still exhibits perovskite structure; it might be described as $Sr_1\ Sr_1\ O_{3-1}$, i.e. $Sr_2O_2$.

The formation of rock salt like SrO (a = 5.16 Å) or $SrO_2$ (a = b = 3.56 Å; c = 6.62 Å) close to the island surface is excluded. Since this should lead to additional reflections in the diffraction pattern which is not in accordance with the measured diffraction data. Hence the perovskite type $Sr_2O_2$ accompanied with oxygen vacancies is suggested even though it has not been reported as a stable strontium oxide phase. It must be emphasized that because of the high cooling rate during reoxidation (600°C/h), the specimen is still in a nonequilibrium state and existance of $Sr_2O_2$ could be described as a metastable phase. The $Sr_2O_2$ phase may be stabilized in a thin layer on top of the island to avoid additional interfacial energies.

## 5.6.2 Islands on the $(\bar{1}20)$ surface

The TEM micrograph (Fig. 5.15) shows an island with a height of about 900 nm on the $(\bar{1}20)$ surface. The island/matrix interface displays a network of dislocations at the interface. This could partially be caused by the rotation of the island against the matrix of about 6.3° as determined by electron diffraction studies. On top of the island a high density of dislocations is also observed. The internal stresses in the top part of the island might be released by the formation of these dislocations.

### a) Electron diffraction study of the $(\bar{1}20)$ island

In contrast to the island on the $(\bar{2}30)$ surface (see section 5.6.1) there is a significant difference between the diffraction patterns of the $(\bar{1}20)$ island and the matrix. While the matrix shows the expected structure of $SrTiO_3$ in the [001]-projection (Fig. 5.15b), the island generates diffraction pattern caused by a simple cubic structure in the same projection with a slight tetragonality (Fig. 5.15a).

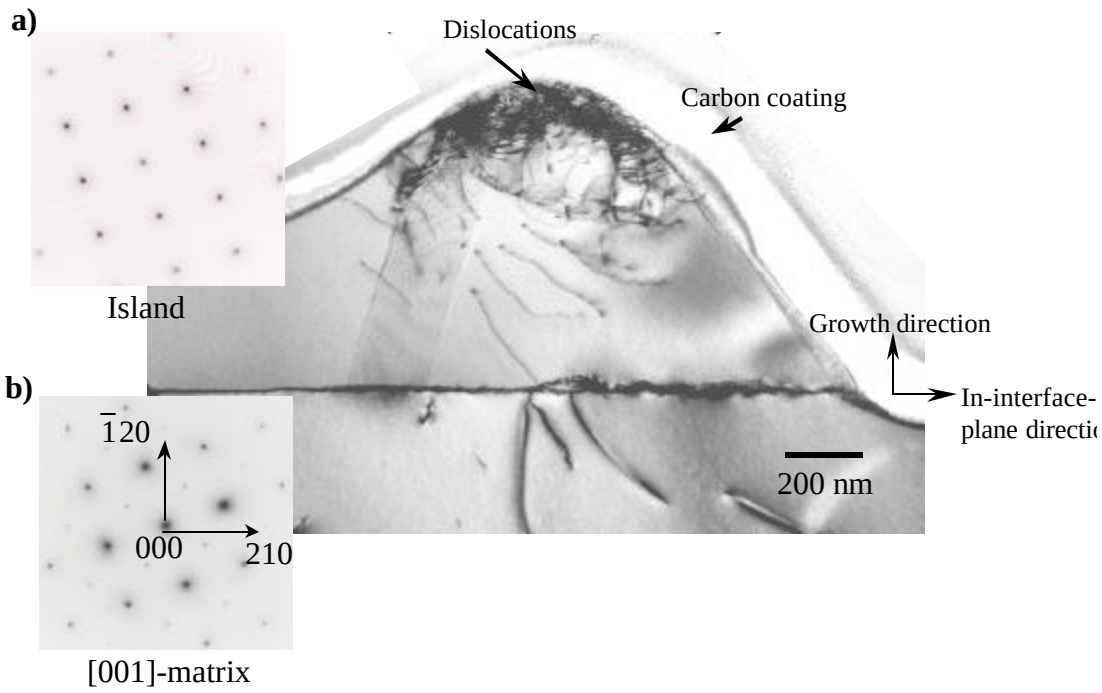


**Fig. 5.15:** Bright-field TEM micrograph ( $\vec{g} = 0\bar{1}1$ ) of an island on the ( $\bar{1}20$ ) surface. Island and matrix revealed a misorientation angle of 6.3° about the [001] zone-axis. **a)** Electron diffraction pattern of the island. **b)** Electron diffraction pattern of the bulk.

Successive electron diffraction patterns were recorded every 100 nm starting in the matrix beneath the island and continuing along the growth direction of the island (the diameter of the selected area aperture using in this experiment was 110 nm at SESAM (Sub-eV-sub-Ångstrøm-Microscope)). The inverse lattice-plane distances ($1/d_{hkl}$) are measured from the diffraction patterns for both the matrix and the island (Fig. 5.16). According to these measurements, there is a sharp change in the lattice-plane distance and thus in the crystal structure at the $SrTiO_3$/island interface. Moreover, within the island the lattice distance in the growth direction differs significantly from that in the interface plane direction. This points to a tetragonal unit cell of the island, which could be caused by the distortion of the lattice during the growth of the island

However, over the whole region of the island, the lattice distances in both directions remain constant within the experimental uncertainty. This suggests a unique structure of the island which will be discussed in section 5.6.2c.

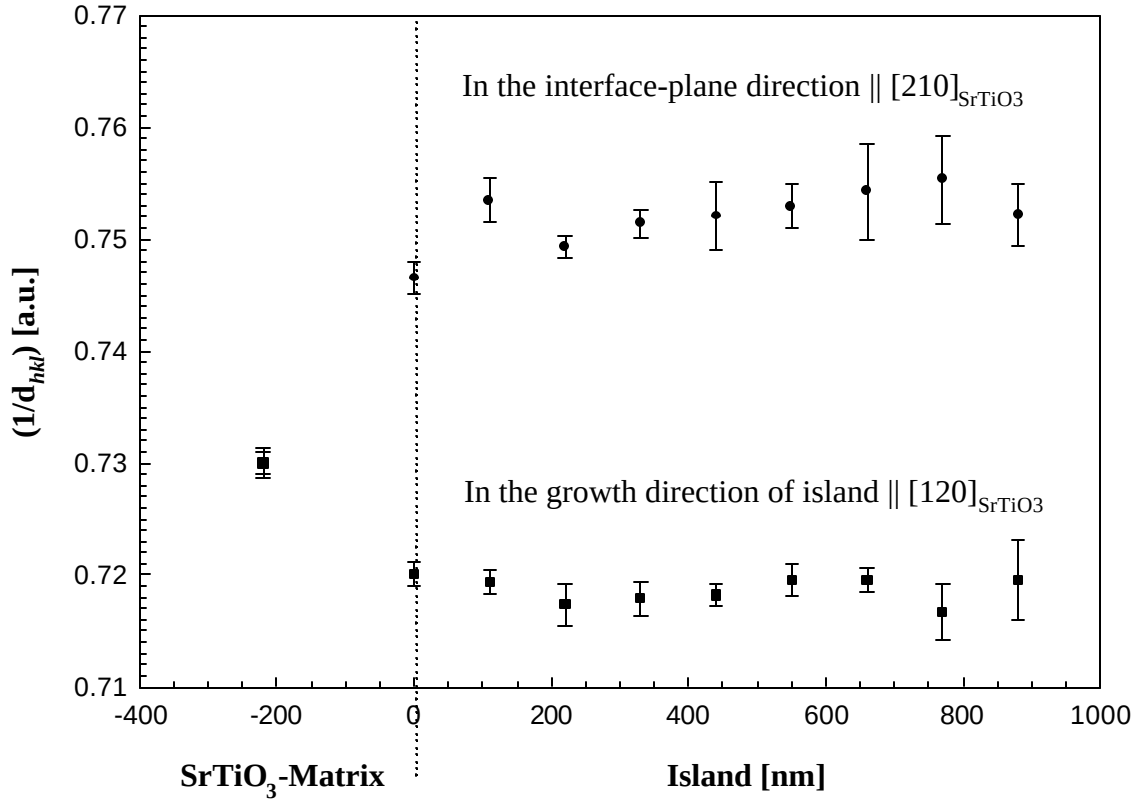


**Fig. 5.16**: Inverse lattice-plane spacing in the matrix and in the $(\bar{1}20)$ island derived from successively recorded diffraction patterns with a step size of 100 nm starting in the matrix beneath the island and continuing along the growth direction of the island.

## b) Chemical composition of the $(\bar{1}20)$ island

The chemical composition of the island was measured near the interface, in the center, and close to the top of the island (Fig. 5.17). The measurements reveal that the entire island consists almost exclusively of $Sr^{2+}$ cations. This is again in contrast to the island on the $(\bar{2}30)$ surface (see Fig. 5.13). Since the first measurement (in Fig. 5.17) was taken at a distance of about 150 nm from the interface, $Ti^{4+}$ ions in the region close to the interface can not be excluded. However, the drastic change of the diffraction pattern in the island and very close to the island/matrix interface supports the assumption of $Ti^{4+}$ ions absence even at the beginning of the island.

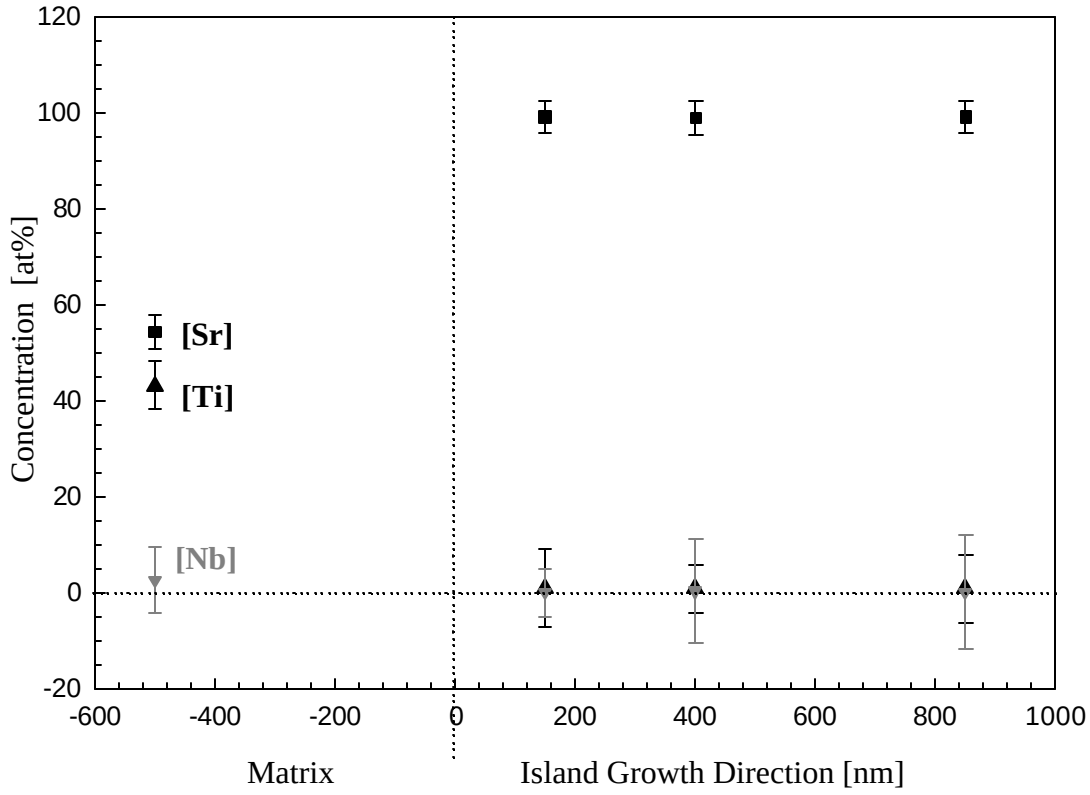


**Fig. 5.17:** Chemical composition of the island with the height of about 900 nm on the $(\bar{1}20)$ surface as well as the matrix beneath island.

## c) Discussion of the island structure on the $(\bar{1}20)$ surface

Considering the fact that the entire $(\bar{1}20)$ island contains only $Sr^{2+}$ cations, one may ask about the crystal structure of the corresponding $SrO_x$. The known possible $SrO_x$ compounds are SrO (rock salt structure, space group *Fm3m*, a = 5.16 Å) and $SrO_2$ (calcium carbide structure, space group I4/mmm, a = b = 3.563 Å, c= 6.616 Å, [Königstein, 98]). In the following both structures are discussed for the explanation of the composition of the $SrO_x$ island.

**1)** Suppose rock salt-like SrO on top of the $SrTiO_3$-matrix (cube-on-cube relation) and interpreting the diffraction pattern of the island (Fig. 5.15a) as the [001]-projection of SrO, the common directions for the both phases in the interface-plane and the growth direction are

$$[001]_{SrO} \parallel [001]_{SrTiO3} \quad ; \quad [6\bar{2}0]_{SrO} \parallel [210]_{SrTiO3}$$

$$[260]_{SrO} \parallel [\bar{1}20]_{SrTiO3}$$

**2)** Suppose $SrO_2$ would be located on top of the $SrTiO_3$-matrix (tetragonal-on-cube relation), the diffraction pattern of the island (Fig. 5.15a) would correspond to the [001] zone axis of $SrO_2$ and therefore the common directions in the interface-plane and the growth direction are

$$[001]_{SrO2} \parallel [001]_{SrTiO3} \quad ; \quad [420]_{SrO2} \parallel [210]_{SrTiO3}$$
$$[\bar{2}40]_{SrO2} \parallel [\bar{1}20]_{SrTiO3}$$

Based on these assumptions, the interface plane for both possible phases would be: SrO (260), $SrO_2$ ($\bar{2}40$) and $SrTiO_3$ ($\bar{1}20$).

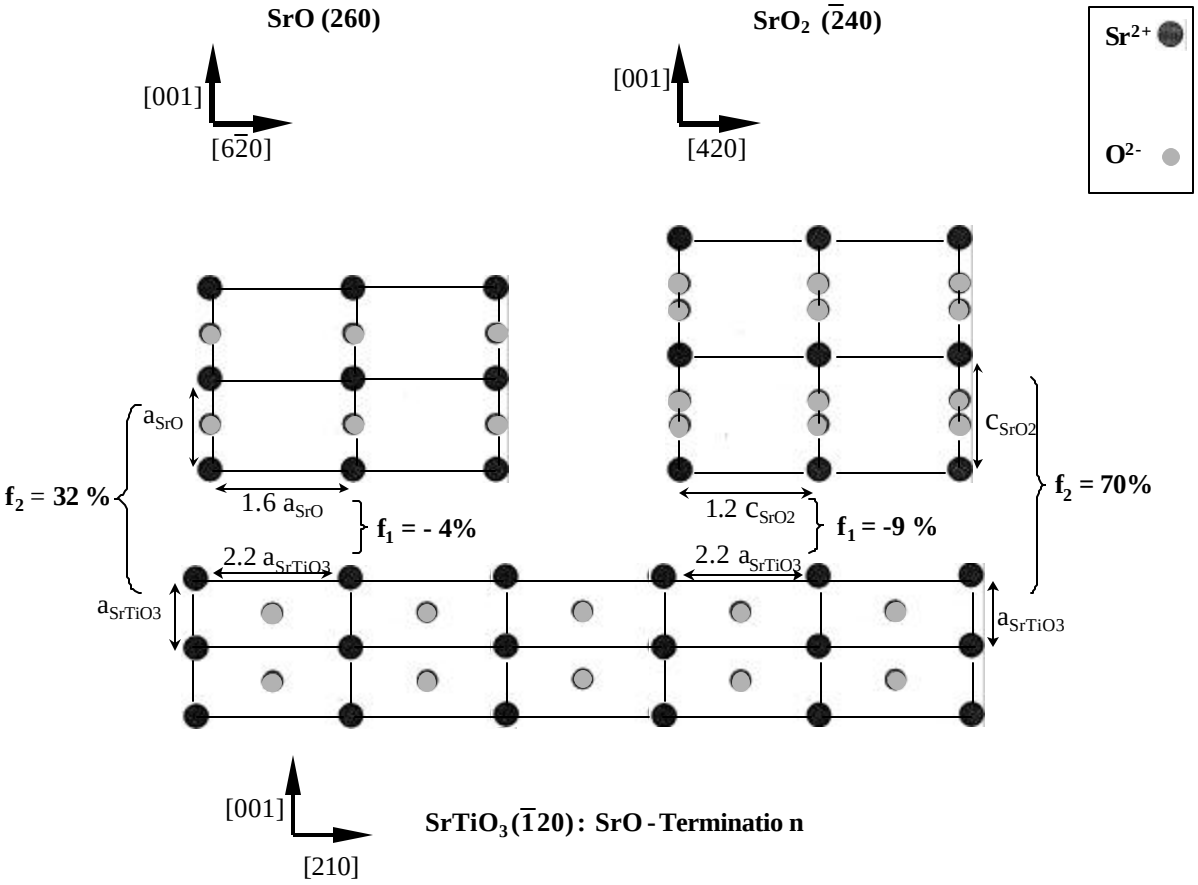


**Fig. 5.18:** Atomic configurations of SrO (260), $SrO_2$ ($\bar{2}40$) and $SrTiO_3$ ($\bar{1}20$) planes. The lattice mismatches ($f_1$, $f_2$) correspond to a face to face contacting of SrO and $SrO_2$ to $SrTiO_3$. The common directions in the interface-plane for each phase are also shown.

A comparison of the atomic configuration of SrO (260) and the $SrTiO_3$ $(\bar{1}20)$ reveals lattice mismatches ($f_1$ and $f_2$) of 4% and 32%, respectively, in the interface plane. In the case of $SrO_2$ $(\bar{2}40)$ on top of the $SrTiO_3$ $(\bar{1}20)$, the lattice mismatches are rather larger (9%, 70%) (Fig. 5.18).

Under these circumstances, it is most likely that the growth of SrO on $SrTiO_3$ is energetically more favorable and SrO is thus suggested as the composition of the island.

# Chapter 6

## Microstructure of bulk Nb-doped polycrystalline $SrTiO_3$ after reoxidation

In the previous part, it was shown that annealing of reduced polycrystalline $SrTi_{0.95}Nb_{0.05}O_3$ at high temperature (1200 °C) under oxygen atmosphere (reoxidation) over a time of 30 hours leads to dramatic topographical changes on the surface of the polycrystal namely the formation of Sr-rich islands on the surface with characteristic shapes and densities. In this part, the influence of reoxidation on the grain interior and GBs of the region beneath the surface is reported.

### 6.1 Grain interior in the reoxidized region

After reoxidation, an optically transparent area developed with an extension of about 50 to 70 µm beneath the surface (bright contrast in Fig.6.1). The optical transparency of this area indicates that a strong decrease of the electron concentration occured, i.e. for a change of the compensation mechanism from electronic (ref. Eq. 2.19) to ionic compensation (ref. Eq. 2.10). This region is therefore referred to as ‘‘reoxidized region’’. At larger distances from the surface (~100 µm), the material is optically no transparent (dark contrast in Fig. 6.1). This region is still reduced and is expected to be semiconducting (Eq. 2.8). The brightness on the edges of the pores and some grains in Fig. 6.1 probably origins from the strong light reflection by the inclined edges and GBs.

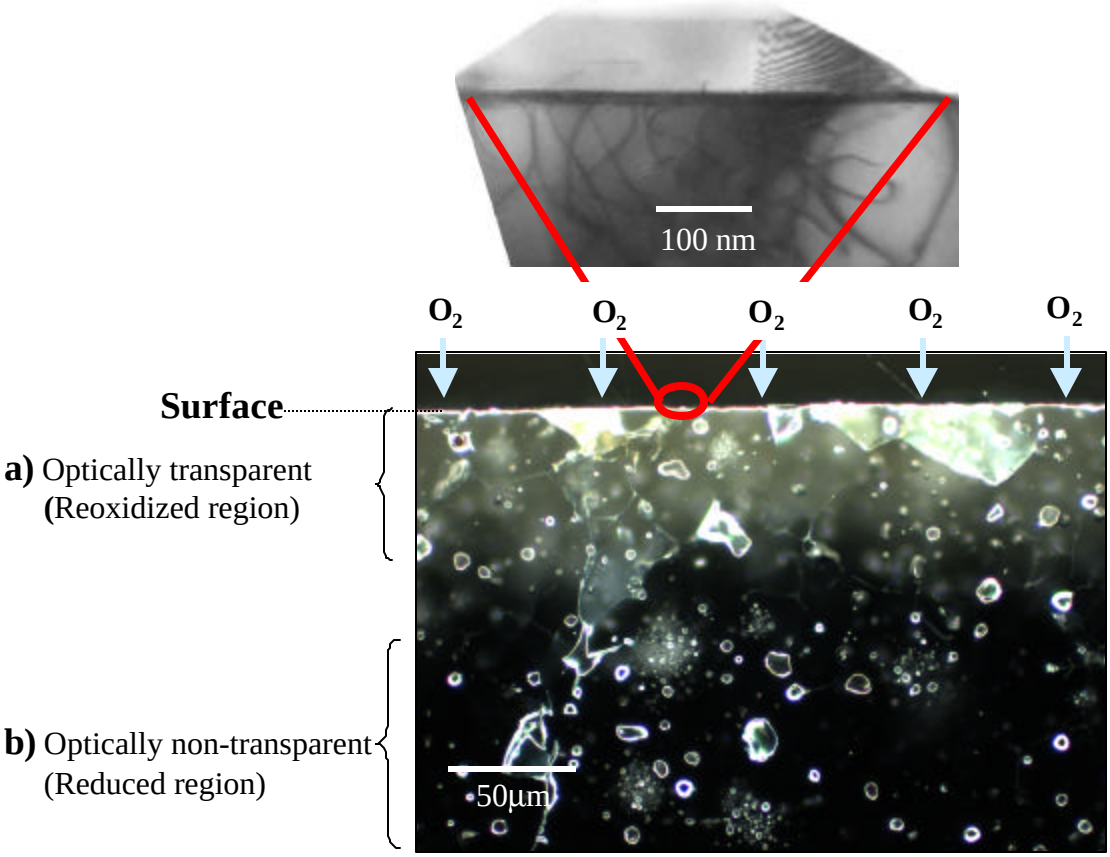


**Fig. 6.1:** Dark-field optical microscopy image of the cross-section of reoxidized polycrystalline $SrTi_{0.95}Nb_{0.05}O_3$ sample. The inset (TEM micrograph) shows an island on top of the surface. **a**) Optically transparent area with an extension of ~ 50-70 µm directly beneath the surface resulting from the reoxidation. **b**) The region far from the surface is still reduce. (The brightness on the edges of the pores and some grains probably origins from strong light reflection by the inclined edges and GBs.)

### a) Electron diffraction study of the reoxidized region

The lattice parameters of the reoxidized and the reduced region were examined by electron diffraction and the results are listed in Table 6.1. The smaller lattice constant of the reduced region (-1.3%) compared to that of the pure $SrTiO_3$ has already been discussed in section 4.3 and was assigned to the high level of Nb doping. The larger lattice constant of the reoxidized region compared to that of the reduced sample (1.6%) and to the pure $SrTiO_3$ (0.3%) will be discussed in terms of the chemical composition data of the reoxidized region in the next section.

**Table 6.1:** Lattice constants (a) of the reoxidized and the reduced region and their variations in comparison to the pure $SrTiO_3$ ($\Delta a / a_{SrTiO3}$).

| Lattice constant | Reduced region | Reoxidized region | $SrTiO_3$ [JCPDS] |
|---|---|---|---|
| a (Å) | 3.855 ± 0.05 | 3.917 ± 0.01 | 3.905 |
| $(\Delta a / a_{SrTiO3})$ [%] | -1.3% | +0.3% | - |

### b) Chemical composition of the reoxidized region

Successive chemical analysis has been performed by EDX(TEM) from the surface (which was free of islands) through the reoxidized layer, down to the reduced region (Fig. 6.2). These experiments revealed the following features:

Sufficiently far from the surface (80-100 µm below the surface), i.e. in the reduced region, we measured, as expected, the same stoichiometry ([Sr] / ([Ti] + [Nb]) = 1.1 ± 0.05) as in the completely reduced sample (reference sample) within the experimental error. On the other hand, pronounced concentration profiles of the $Sr^{2+}$ and $Ti^{4+}$ cations are found in the reoxidized region. While directly beneath the surface an enrichment of $Sr^{2+}$ and a deficiency of $Ti^{4+}$ cations are determined relative to the reduced region, this concentration difference becomes smaller by gradually approaching the reduced region.

In a depth of ca. 50 µm even the reverse case, i.e. a reduced $Sr^{2+}$ concentration and an enhanced $Ti^{4+}$ level was found. The concentration of $Nb^{5+}$ ions shows no significant change in this region.

Owing to experimental reasons (strongly increasing thickness of the TEM sample), these data could not be obtained along a single line perpendicular to the $SrTiO_3$ surface but corresponds to laterally varying positions. Also further measurement data of the region with less $Sr^{2+}$ concentration (in a depth of ca. 50 µm) could, unfortunately, not be obtained and hence neither the thickness of this region nor the maximum $Sr^{2+}$ deficiency could be measured. Nevertheless, it is worth emphasizing that such a concentration profile of $Sr^{2+}$ cations was not expected since in literature a lower Sr-content (i.e. the formation of $V''_{Sr}$) is assumed. The observed chemical heterogeneity in the reoxidized region can be interpreted in terms of a **"kinetic demixing"** of $Sr^{2+}$ and $Ti^{4+}$ cations.

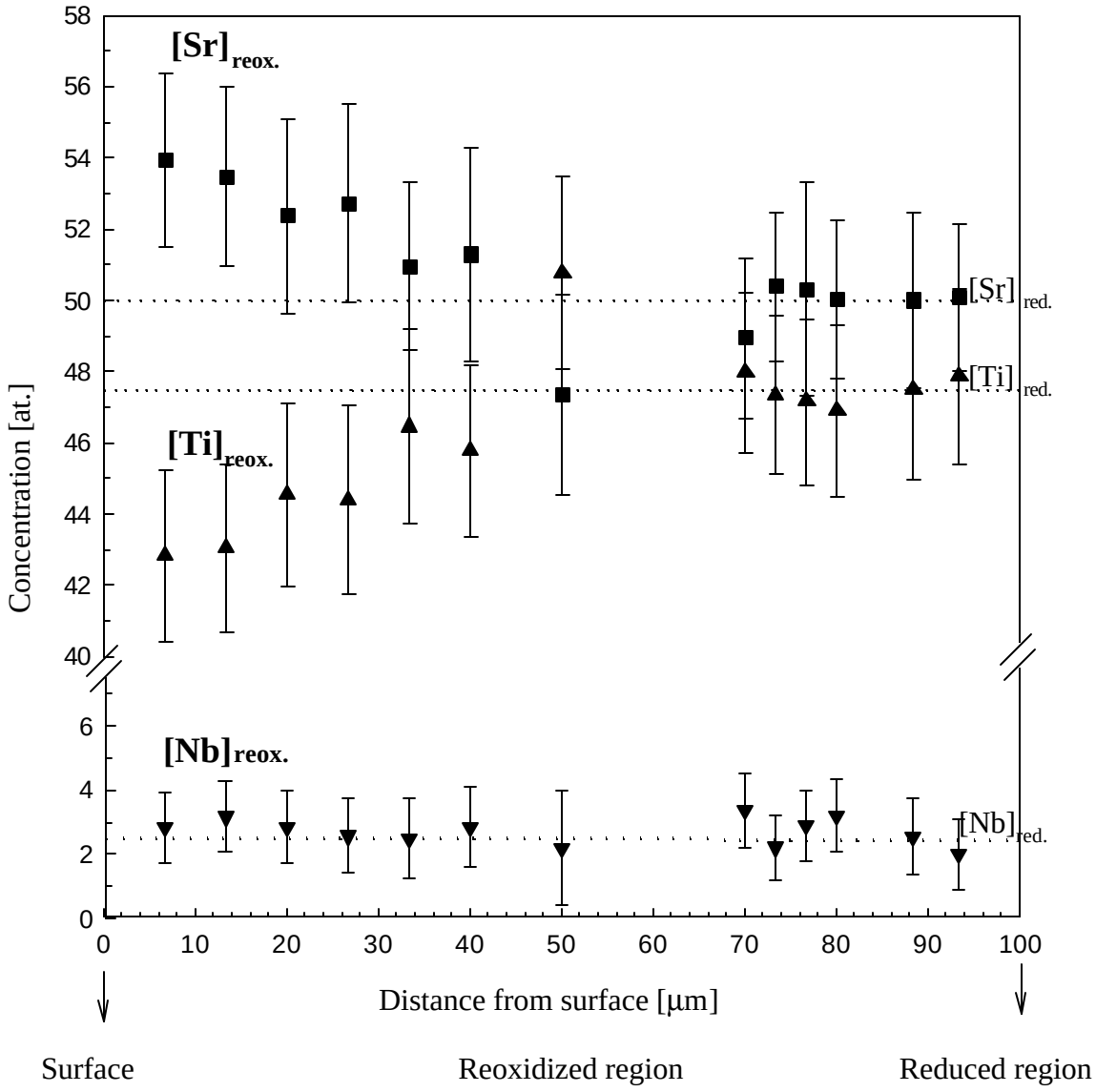


**Fig. 6.2:** Evolution of the cationic composition beneath the surface up to the reduced region as measured by EDX (TEM). While the $Nb^{5+}$ concentration is almost constant, $Sr^{2+}$ and $Ti^{4+}$ cations undergo demixing in the reoxidized region. The dashed lines relate to the concentrations of cations in the reduced sample (The data are normalized to the data of the reduced sample: [Sr] = 50 at%; [Ti] = 47.5 at%; [Nb] = 2.5 at%).

### c) Discussion of kinetic demixing in $SrTiO_3$ and the defect chemical consequences

Kinetic demixing is defined as the compositional separation of an initially homogeneous oxide (A, B)O, due to different cationic mobilities under a common driving force. The driving forces may be an oxygen potential gradient [Schmalzried, 79], a temperature gradient [Monceau, 91], or an electric field gradient [Teller, 97] in the bulk. In our study, there was no evidence of additional phases in the reoxidized region of the sample under TEM investigation; rather a chemical heterogeneity in terms of a spatial separation of $Sr^{2+}$ and $Ti^{4+}$ cations in $SrTiO_3$ was found.

The driving force for the "kinetic demixing" of $Sr^{2+}$ and $Ti^{4+}$ cations is the strong oxygen chemical potential difference between the surface, which is in contact with the outer atmosphere ($p(O_2)$ ~1 bar), and the reduced bulk (corresponding to $p(O_2) \sim 10^{-20}$ bar). The prerequisite for kinetic demixing in a chemical potential gradient is a different mobility of cations: since a high chemical potential of oxygen corresponds to a high cation vacancy concentration (see Fig. 2.2), an oxygen potential gradient leads to a diffusion of cations from low to high $p(O_2)$. The more mobile cation, however, diffuses faster towards the higher oxygen chemical potential side than the less mobile one and a chemical inhomogeneity results. In $SrTiO_3$, $Sr^{2+}$ ions as the more mobile cation ([Tien, 67], [Eror, 81]), [Chan 81], [Moos, 97]) can therefore be assumed to "segregate" to the near-surface region.

However, from this scenario one might explain an enhanced (relative) Sr/Ti ratio but not a pure presence of $Sr^{2+}$ compared to the reduced region This rises the question of site occupancy during reoxidation at 1200 °C. Partly substitution of $Ti^{4+}$-ions by $Sr^{2+}$ ions ($Sr_{Ti}^{''}$) could explain the absolute $Sr^{2+}$ enrichment. Such a process would suggest that, the compensation of $Nb_{Ti}^{\bullet}$ ions in this region may occur by $Sr_{Ti}^{''}$ rather than by $V_{Sr}^{''}$. The larger lattice constant in this region compared to that of the reduced region (Table 6.1) can also be explained by the presence of $Sr_{Ti}^{''}$ defects in this region.

Since the mass balance of $Ti^{4+}$ and $Sr^{2+}$ ions has to be fulfilled in the entire sample, then the increased $Sr^{2+}$ concentration (probably via $Sr_{Ti}^{''}$) in the upper side of the reoxidized region (near the surface) has to be counterbalanced through an increased $Ti^{4+}$ concentration in another region of the specimen. Such an increased $Ti^{4+}$concentration is found in a depth of ca. 50-70 µm below the surface (bottom side of reoxidized region). Owing to the lack of more data-points and the fact

that lateral inhomogeneities play also a role, a quantitative check of the mass balance is not possible. The increased $Ti^{4+}$concentration in this region suggests that $Ti_{Sr}^{\bullet\bullet}$ species might be counterbalanced either by $V_{Sr}^{''}$ or by further electrons despite an unchanged crystal structure. It would therefore be interesting to measure locally the conductivity of the inhomogeneous region in future measurements.

The described model suggests that charge compensation by $Sr^{2+}$ on $Ti^{4+}$-sites has to be considered in donor doped $SrTiO_3$, in addition to electron compensation of $Nb_{Ti}^{\bullet}$ (reduced sample) and $V_{Sr}^{''}$ compensation (leading to the formation of Sr-rich phases). Such a charge compensation mechanism has not been observed yet in perovskite-type oxides. It should be emphasized that the kinetic demixing is a phenomena that only occurs in nonequilibrium situations (e.g. under $p(O_2)$ gradients). It is therefore not in contradiction with the general assumption that $V_{Sr}^{''}$ are the dominant ionic defects. After complete reoxidation of the entire sample such Sr/Ti-profiles are therefore assumed to vanish.

## 6.2 Grain boundaries of Nb-doped polycrystalline $SrTiO_3$ after reoxidation

### 6.2.1 Microstructure

A straightforward way to display the microstructural changes of the polycrystalline sample after reoxidation, is the study of fractured reoxidized samples. While the reduced samples show a transgranular fracture (Fig. 6.3a), the reoxidized samples fractured intergranularly (Fig. 6.3b). The intergranular fracture of reoxidized sample is most probably caused by the presence of secondary phases on the GB planes, which were formed during the oxidation process. These secondary phases can readily be revealed at GBs (Fig. 6.3b).

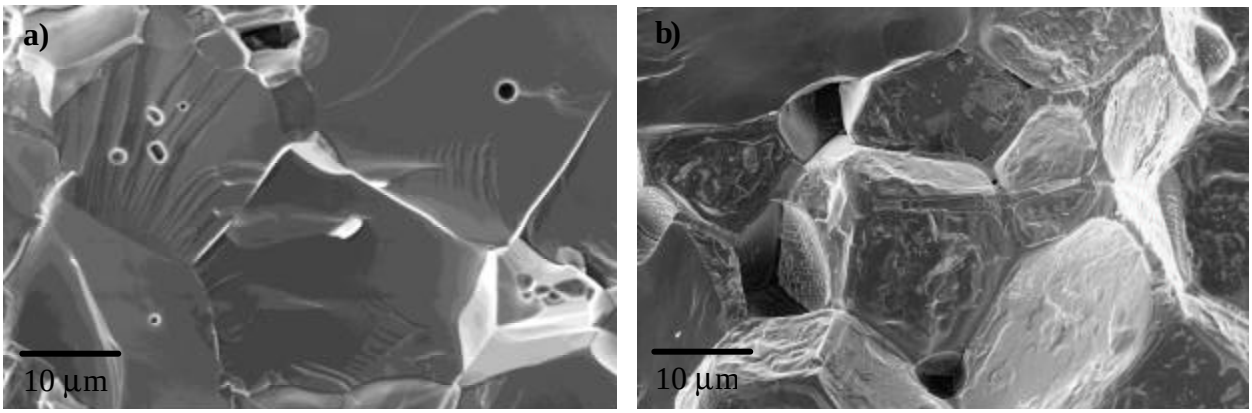


**Fig. 6.3:** SEM micrographs of fractured polycrystalline $SrTi_{0.95}Nb_{0.05}O_3$. **a)** Reduced sample exhibits a transgranular fracture. **b)** Reoxidized sample shows a intergranular fracture. The rough surfaces of the grains are due to the secondary phase formation during reoxidation.

Secondary phases also appear in the SEM micrograph of the polished reoxidized sample as a bright contrast at the GBs as well as at the triple grain junctions (arrow in Fig. 6.4). This is in contrast to the reduced samples, which are free of secondary phases (see section 4.2).

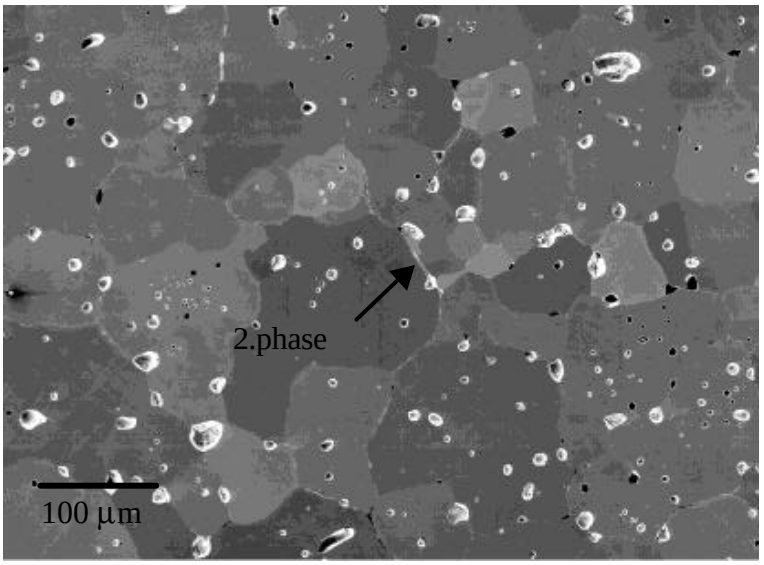


**Fig. 6.4:** SEM micrographs of the cross sectional view of the reoxidized sample after polishing. Bright contrasts at some of the GBs correspond to the secondary phases due to reoxidation.

### a) Electron diffraction study of the secondary phase

Fig. 6.5 shows the TEM micrograph of a secondary phase located at a triple grain junction. The diffraction pattern of the secondary phase is taken in [100]-zone axis (Fig. 6.5b). Additional spots along the [001] direction can be seen. These spots are not present on the diffraction pattern of the neighboring bulk (Fig. 6.5a). The existence of this super-reflections is examined by imaging in [210]-zone axis after tilting the sample in the corresponding direction. In this zone-axis, the super-reflections appear also in [001] direction of $SrTiO_3$ (Fig. 6.5c).

The electron diffraction pattern of the precipitate fits (Fig.6.5 b) very well to that of $Sr_2TiO_4$ (RP-phase; n=1) reported by Tilley [Tilley, 77]. Assuming that the secondary phase is $Sr_2TiO_4$, then the lattice constants of the secondary phase can be derived from the related diffraction pattern (Fig. 6.5b, c) are

$$a = b = (3.983 \pm 0.014)\ \text{Å} \quad ; \quad c = (11.65 \pm 0.23)\text{Å}$$

These data fit very well to literature values of $Sr_2TiO_4$ (Table 2.1). Owing to the lack of data, the existence of other members of the RP series ($n$ = 2, 3, ...) can not be excluded.

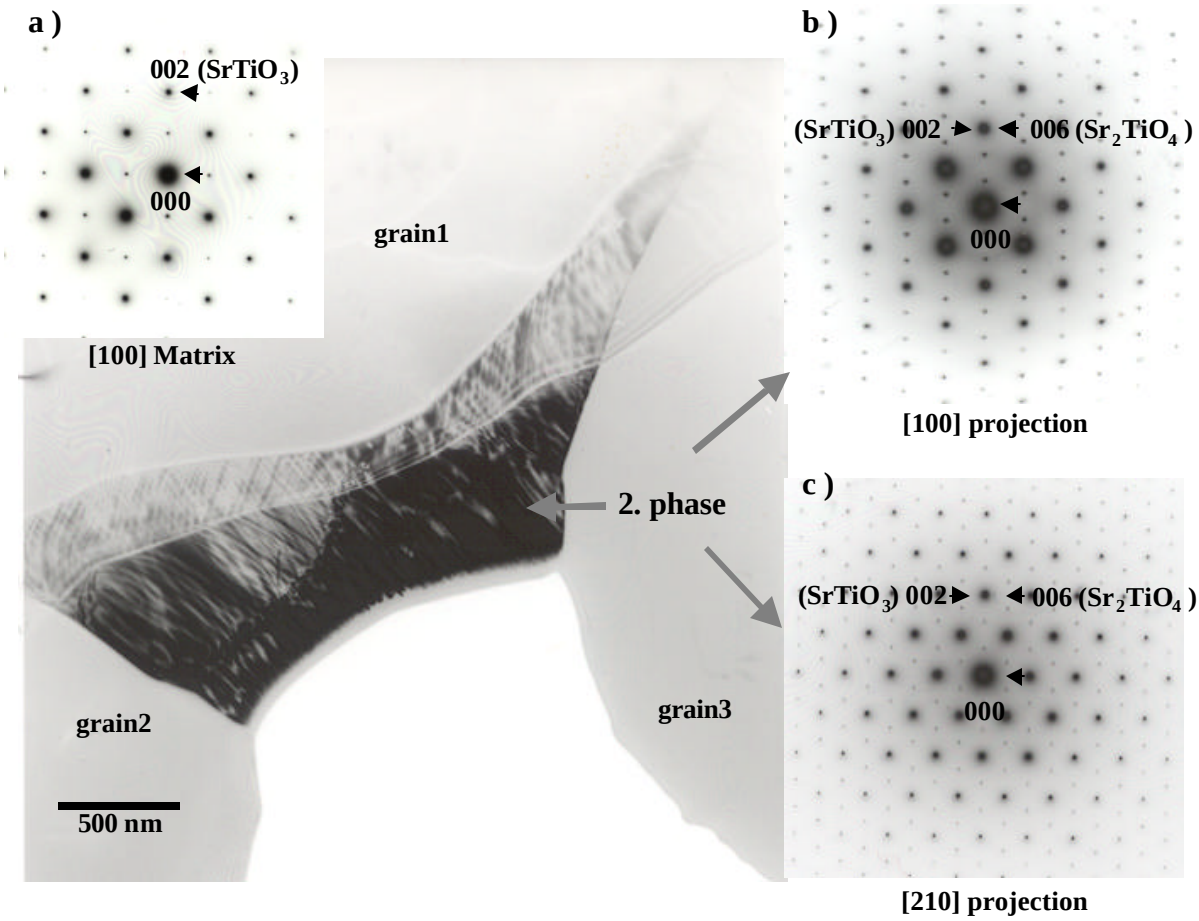


**Fig. 6.5:** Bright-field TEM micrograph of the bulk of the reoxidized $SrTi_{0.95}Nb_{0.05}O_3$ sample viewed along the [100]-zone axis. Secondary phase is present at the triple junction. Insets show electron diffraction patterns of **a)** the matrix in [100]-zone axis, and of the secondary phase in **b)** [100]-zone axis and **c)** [210]-zone axis.

The electron diffraction patterns of $SrTiO_3$ and $Sr_2TiO_4$ were calculated for kinematical condition (Fig. 6.6a,b). The calculations were performed by applying "Ideal Microscope" software (EM lab). These results match within the experimental errors with those obtained from the experiments (Fig. 6.5a,b).

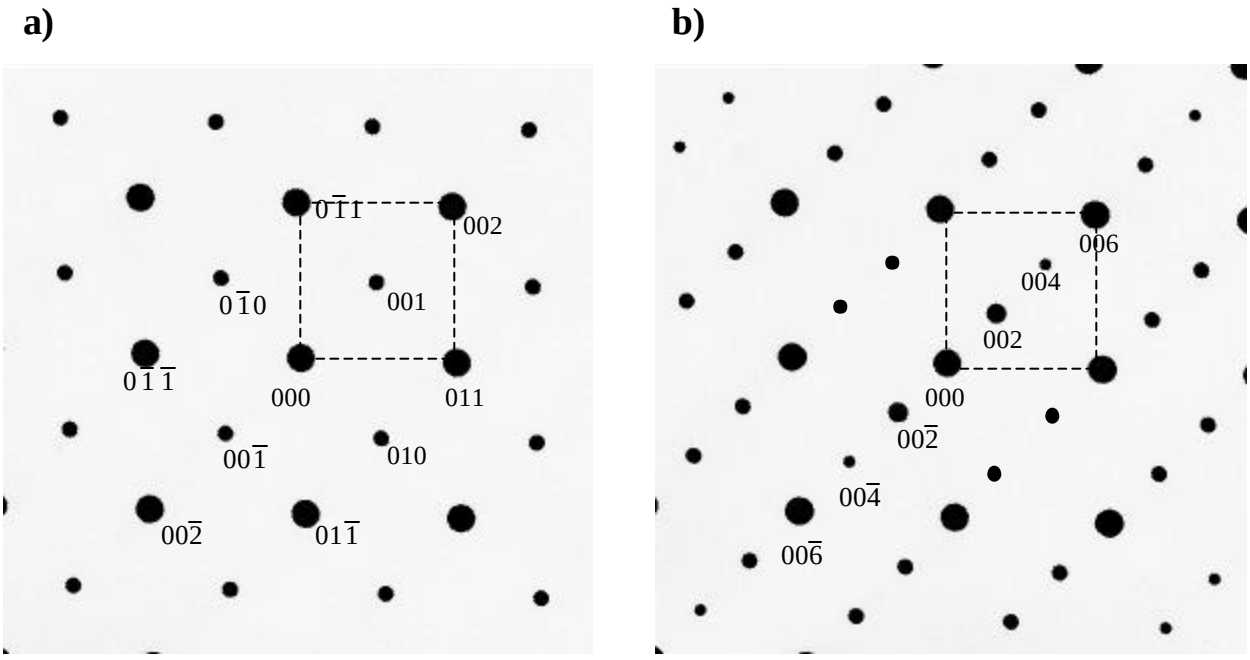


**$SrTiO_3$**: [100] projection **$Sr_2TiO_4$**: [100] projection

**Fig. 6.6:** Simulated diffraction pattern under kinematical condition along the [100]-zone axis of **a)** $SrTiO_3$ and **b)** $Sr_2TiO_4$ (RP- phase, $n$= 1). (The necessary data to produce the unit cell of $SrTiO_3$ and $Sr_2TiO_4$ are derived from Table 2.1).

Several authors ([Daniels, 76], [Moos, 97], [Menesklou, 99], [Meyer, 02]) predicted the formation of Sr-rich intergrowth layers inside the material as a consequence of the change of the charge compensation mechanism for donors from **electronic**, which takes place in the reduced state of the sample, to the **metal vacancy (**$V_{Sr}^{''}$**)** compensation, taking place in the reoxidized state. However, an experimental proof for the formation of a RP-phase have not been given yet.

The above mentioned observation of $Sr_2TiO_4$ intergranular phase (RP-phases with $n$=1) in the reoxidized $SrTi_{0.95}Nb_{0.05}O_3$ samples is thus the first explicit evidence for a Sr-rich secondary phase at GBs after reoxidation.

## 6.2.2 Electrical characterization of reoxidized samples

The impedance spectrum of the reoxidized sample at room temperature is shown in Fig. 6.7. It consists of a single arc with a finite high frequency intercept. The high-frequency intercept (at 1 MHz, see inset in Fig. 6.7) exhibits a small impedance of 5 Ω, which corresponds to the part of the sample which is still reduced or only slightly reoxidized. The contributing semicircle could not be measured since its relaxation frequency exceeds the upper limit of the equipment frequency (1 MHz).

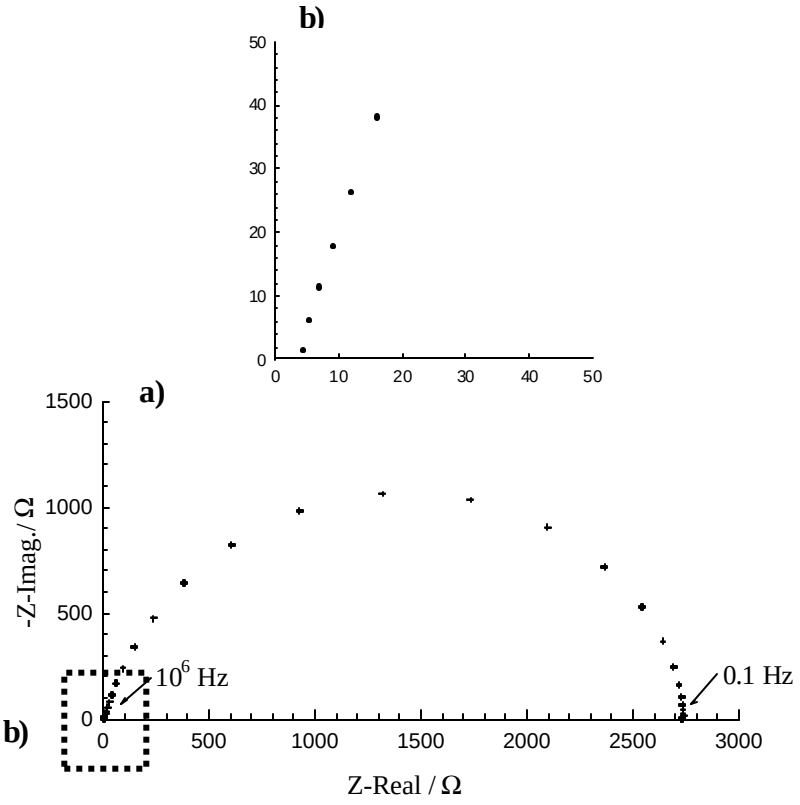


**Fig. 6.7:** Impedance spectrum of the reoxidized $SrTi_{0.95}Nb_{0.05}O_3$ sample, measured at room temperature and in the frequency range of 0.1 to $10^6$ Hz. **a)** The low-frequency intercept of spectrum shows a resistance of ~ 2700 Ω due to the reoxidation of the grain interior. **b)** The high-frequency intercept (inset) exhibits a residual impedance of 5 Ω.

The low-frequency arc with a diameter of ca. 2700 Ω reflects the resistance of the reoxidized region, which is much higher than that of the reduced sample (0.5 Ω, see section 4.3). The smoothly depressed semicircle can easily be understood by the inhomogeneous composition of the reoxidized part (different diffusion profiles etc. see Fig. 6.2). However, from the corresponding capacitance it can be concluded that the measured resistance is caused by the reoxidized grain interiors rather than by the GBs.

## 6.3 Concluding remarks

According to the observations presented in this thesis there exists, besides $Sr^{2+}$ segregation at the surface leading to the islands (see chapter 5), two possibilities for ionic compensation of the Nb-dopant in the bulk of the material: *i)* precipitation of a Sr-rich phase at GBs (RP-phase) and *ii)* $Sr^{2+}$ on $Ti^{4+}$ sites.

The entire reoxidation process of $SrTiO_3$ is thus rather complicated. Close to the surfaces with high oxidation tendency (e.g. (111) surface), it is probably the segregation of $Sr^{2+}$ ions to the surfaces leading to $V_{Sr}^{''}$ in the surface-near region and thus to an ionic compensation of dopants in this region. One can estimate the depth of the ionic compensation region beneath the surface assuming a given surface of area "A" being covered by SrO-islands with an areal density of "$\rho_{island}$" and an average height of "$h_{island}$". This surface then hosts $[4 \cdot \rho_{island} \cdot A \cdot h_{island} / (a_{SrO})^3]$ Sr-ions which corresponding to $[1 \cdot A \cdot h_{SrTiO3} \cdot 0.025 / (a_{SrTiO3})^3]$ Sr-ions coming out from a depth of "$h_{SrTiO3}$" beneath the surface and leaving equivalent amount of $V_{Sr}^{''}$ behind in the bulk. The factor 0.025 stands for a complete $V_{Sr}^{''}$ compensation (2.5%) of Nb-dopants and the numbers four and one denote the number of Sr ions existing in the SrO and $SrTiO_3$ unit cell, respectively. The thickness of the ionic compensation region under, for example, a (111) surface with a covering of 30% by SrO-islands (Fig. 5.7) and an average island height of 500 nm (Fig. 5.2) is therefore ~10 µm. Since a smooth decrease of the $V_{Sr}^{''}$ concentration rather than a sharp "box-like" profile is realistic, the islands on such a (111) surface might correspond to a reoxidized region of several 10 µm.

Beneath the surfaces with low oxidation tendency and possibly also "deep" in the crystal, however, either the site exchange ($Sr_{Ti}^{''}$) driven mainly by a gradient of oxygen chemical

potential perpendicular to the surface, or the $Sr^{2+}$ segregation to the GBs (RP-phase) dominate. This probably leads to vertically and laterally inhomogeneous concentrations and conductivities distributions and would be an interesting task to further analyze these inhomogeneities by structural, chemical and electrical measurements.

# Chapter 7

## Summary

This works addressed the phenomena that take place upon high-temperature annealing (1200°C, under oxygen atmosphere) of (5 at.%) Nb-doped polycrystalline $SrTiO_3$ ($SrTi_{0.95}Nb_{0.05}O_3$) sintered initially in a reducing atmosphere. Reoxidation leads to dramatic structural and compositional changes both on the surface as well as in the grains interior beneath the surface and at the GBs. The main findings are summarized in the following:

### 1. Island Formation on the Surface

After oxidation for 30 h, the polished surface of an initially reduced polycrystalline sample is partly covered by micro-crystalline secondary phases referred to as “islands”. Depending on the surface orientation of the underlying grain, the islands show characteristic shapes, specific orientation relationships with the surface and strongly different densities (area of all islands/total area of the underlying grain). OIM measurements revealed that, with respect to the tendency of island formation, surface orientations can be divided in three classes.

- (111) surfaces and similarly oriented surfaces such as (122) and (112) have a high island density ($\rho$ = 30%).
- (001) surfaces and similarly orientated surfaces such as (013) and (114) exhibit low island density ($\rho$ = 5%).
- (011), (133) and (123) surfaces show a moderate island density ($\rho$ = 15%).

Each class includes one of the main surface orientations, i.e. (001), (011) and (111), but also higher indexed surfaces with an inclination of less than 20° compared to the low indexed surface.

The density of the islands on the surface can be used as an indicator for the tendency of a surface towards oxidation. This means that the (111), (001) and (011) surfaces have high, low and moderate oxidation tendency, respectively. The (111) surface, being polar, possesses a high surface energy, which might be lowered by the formation of secondary phase upon

oxidation. This may explain the high island density of the (111) surface. On the other hand, (001) being a non-polar surface, has a low surface energy, which may explain the low oxidation tendency. Concerning the (011) surface, there is a higher net surface charge, compared to the (001) surface, but a lower charge compared to the (111) surface, and this may account for the moderate oxidation tendency of this surface. The existence of the three classes of surface orientations mentioned above means, that the oxidation tendency of any other surface can be predicted by determining the orientation neighborhood of this surface to a main surface (misorientations up to 20°). Once the adjacent main surface is specified, then the given surface shows the similar island formation tendency as this main surface.

The structures and the compositions of the islands vary significantly from each other. This is examined for two islands on (023) and (012) surfaces and yields the following results: The island with a height of almost of 250 nm located on a (023) surface shows an electron diffraction pattern that is identical to that of the matrix (but having more intense 100 super-reflections). This suggests that the island has a perovskite structure. According to EDS analysis, the island shows a compositional gradient in the growth direction. Near the interface it exhibits a stoichiometric composition similar to that of the matrix. However, in the growth direction the $Sr^{2+}$ concentration increases at the expense of $Ti^{4+}$ ions. Assuming that the perovskite structure of the island is retained, this increase corresponds to the gradual substitution of $Ti^{4+}$ with $Sr^{2+}$ ions via the formation of $Sr_{Ti}^{''}$ defects and $V_O^{\bullet\bullet}$ counter defects in the growth direction. A continuous change from $SrTiO_3$ to $Sr_2O_2$ through the formation of $Sr(Ti_{1-x}Sr_x)O_{3-x}$ ($0 \leq x \leq 1$, x increases in the growth direction of the island) is therefore suggested.

On the other hand, an island with a height of 900 nm located on a (012) surface exhibits a different electron diffraction pattern compared to that of the matrix. The fact that the EDS analysis of this island revealed the presence of $Sr^{2+}$ ions only and, in addition, a good fitting of the experimental lattice-plane spacing of the island with literature data for SrO. Therefore it is most likely that this island exists as a distorted SrO with SrO (260) as the interface-plane which is parallel to $SrTiO_3$ (012). The growth of SrO (260) on the $SrTiO_3$ (012) surface is then accompanied by lattice mismatches of 4% in $[210]_{SrTiO3}$ and ~30% in $[001]_{SrTiO3}$ directions.

These studies show for the first time the relation between island formation (oxidation tendency of the surface) and surface orientation as well as the chemical and structural properties of the islands. Future investigations have to show, in how far the orientation of a surface determines the island structure and composition.

## 2. Kinetic demixing in the region beneath the surface

After reoxidation, an optically transparent layer, the so-called “reoxidized region”, was found beneath the surface with a thickness of about 50-70 μm. A pronounced demixing of cations is found in this region: an enrichment of $Sr^{2+}$ cations close to the surface (the region with high chemical potential of oxygen corresponding to higher $p(O_2)$) is counterbalanced by $Ti^{4+}$ excess on the other side of the reoxidized region, away from the surface (the region with lower chemical potential of oxygen corresponds to a lower $p(O_2)$). At a first glance this is surprising since one might expect a Sr-depletion close to the surface corresponding to the expected change from electronic to ionic charge compensation of the dopant. However, the strong oxygen chemical potential gradient between the surface and the bulk interior acts as the driving force for a kinetic demixing. The prerequisite for such a demixing are different cation mobilities which is the case for $SrTiO_3$. Since the $Sr^{2+}$ cations are more mobile than all other cations, an enrichment of $Sr^{2+}$ cations in the region with higher chemical potential of oxygen, namely in the near-surface region is therefore in accordance with this model. These measurements present the first experimental evidence for a kinetic demixing in $SrTiO_3$ during reoxidation. It is concluded that in the near-surface region excess $Sr^{2+}$ cations replace $Ti^{4+}$-sites and result in $Sr_{Ti}^{\bullet}$ defects which compensate the charge of $Nb_{Ti}^{\bullet}$. The lattice parameter is larger in the near-surface region compared to that of $SrTiO_3$ (0.3%). This is also in accordance with this model. This means that, in addition to the conventionally discussed charge compensation mechanism ($e'$ or $V_{Sr}^{''}$), this study shows for the first time that also anti-site defects ($Sr_{Ti}^{\bullet}$) can lead to a compensation of the donor dopant in $SrTiO_3$. On the other hand, far away from the surface (deeper side of the reoxidized layer), the excess $Ti^{4+}$ cations occupy $Sr^{2+}$ lattice sites and result in $Ti_{Sr}^{\bullet\bullet}$ defects. Hence, in this region the electrons and/or $V_{Sr}^{''}$ provide the charge compensation of $Nb_{Ti}^{\bullet}$ and of $Ti_{Sr}^{\bullet\bullet}$.

## 3. Formation of Ruddlesden-Popper phase at grain boundaries

After reoxidation, a Sr-rich secondary phase ($Sr_2TiO_4$) could be identified at the triple junctions in the bulk. This material is derived from the appearance of additional reflections in [001] direction in the electron diffraction pattern of the secondary phase for both, the [100] and [210] zone-axis. $Sr_2TiO_4$ belongs to the homologous series $Sr_{n+1}Ti_nO_{3n+1}$, which are well

known as Ruddlesden-Popper Phases. Owing to the lack of data, the existence of the other members ($n$ = 2, 3, ...) can neither be proved nor excluded. This is the first explicit evidence of the existence of a RP-phase inside $SrTiO_3$ caused by reoxidation. Several authors (e.g. [Daniels, 76], [Moos, 97b]) predicted the existence of these phases as a consequence of the change in the charge compensation from electronic into $V_{Sr}^{''}$ but could not provide an experimental proof.

In summary, this study has lead to a much better understanding of the chemical, structural and defect chemical phenomena occurring at the surface and in the bulk of reduced donor-doped $SrTiO_3$ during reoxidation.

# Zusammenfassung

Nb-dotiertes (5 At.%), polycrystallines $SrTiO_3$, das in einer reduzierenden Atmosphäre gesintert wurde, zeigt bei weiterer Temperaturbehandlung bei 1200°C unter Sauerstoffatmosphäre (Reoxidation) erhebliche strukturelle und chemische Veränderungen. Diese erfolgen sowohl an der Oberfläche, in den oberflächennahen Körnern und an den Korngrenzen.

## 1. Inselbildung

Auf der polierten Oberfläche einer reduzierten, polykristallinen Probe bilden sich nach 30-stündiger Oxidation „Inseln“ mikrokristalliner Größe. Form, Häufungsdichte und laterale Anordnung der Inseln zeigen dabei eine charakteristische Abhängigkeit von der Orientierung der Oberfläche. Mit Hilfe von OIM-Messungen konnten drei Klassen von Oberflächenorientierungen unterschieden werden, die sich hinsichtlich der Inselbildung signifikant unterscheiden:

- (111)-, (122)- und (112)-Oberflächen zeigen eine hohe Inseldichte.
- (001)-, (013)- und (114)-Oberflächen zeigen eine geringe Inseldichte.
- (011)-, (133)- und (012)-Oberflächen zeigen eine mittlere Inseldichte.

Jede dieser drei Gruppen besteht aus einer niedrig orientierten Oberfläche (d.h. (001)-, (011)- oder (111)-Oberfläche) und höher indizierten Oberflächen mit einer Orientierungsabweichung bis zu 20°.

Da die Häufungsdichte der Inseln als Maß für die Oxidationsneigung der Oberflächen gelten kann, zeigt eine (111)-Oberfläche die höchste, eine (001)-Oberfläche die niedrigste und eine (011)-Oberfläche eine mittlere Oxidationsneigung. Diese Beobachtung läßt sich wie folgt beschreiben. Die (111)-Oberfläche ist eine polare Oberfläche, deren hohe Oberflächenenergie durch Bildung einer zweiten Phase während der Oxidation vermindert werden kann. Dagegen ist die (001)-Oberfläche eine nicht-polare Oberfläche mit entsprechend niedrigerer Oberflächenenergie und Oxidationsneigung. Die (011)-Oberfläche hat verglichen mit der (001)-Oberfläche eine höhere, verglichen mit (111)-Oberfläche aber eine niedrigere effektive Ladungsdichte. Dies erklärt die moderate Oxidationsneigung dieser Oberfläche.

Struktur und Zusammensetzung der Inseln unterscheiden sich in Abhängigkeit von der Oberflächenorientierung in signifikanter Weise. Dies wurde für je eine Insel auf der (023)-

bzw. (012)-Oberfläche nachgewiesen. Die untersuchte Insel auf der (023)-Oberfläche zeigte bei einer Höhe von 250 nm ein mit der Volumenphase identisches Elektronenbeugungsbild (mit einer höheren Intensität der 100 Super-Reflexe). Dies deutet darauf hin, dass die Insel eine Perowskit-Struktur besitzt. Die chemische Analyse mit Hilfe von XEDS-Messungen zeigen, dass die stöchiometrische Zusammensetzung der Insel nahe der Grenzfläche derjenigen des $SrTiO_3$ Volumens entspricht. Die Zusammensetzung ändert sich kontinuerlich in Wachstumsrichtung der Insel und wird dabei zunehmend $Sr^{2+}$-reicher auf Kosten der $Ti^{4+}$-Ionen. Die Perowskit-Struktur der Insel bleibt jedoch erhalten. Es ist anzunehmen, dass die $Ti^{4+}$-Ionen in Wachstumsrichtung allmählich durch $Sr^{2+}$-Ionen in Form von $Sr''_{Ti}$ Defekten ersetzt werden. Dies entspricht einer strukturellen und chemischen Veränderung der (023)-Insel in Wachstumsrichtung von $SrTiO_3$ zu $Sr_2O_2$ durch Bildung von $Sr_1(Ti_{1-x}Sr_x)O_{3-x}$ (0=x=1; x wächst in Wachstumsrichtung). In diesem Modell würden Sauerstoffleerstellen für den Ladungsausgleich der $Sr''_{Ti}$-Defekte sorgen. Dagegen zeigt die untersuchte 900 nm hohe Insel auf der (012)-Oberfläche ein vom $SrTiO_3$-Volumen deutlich verschiedenes Elektronenbeugungsbild. Die gemessenen Gitterebenenabstände in der Insel stimmen gut mit den in der Literatur genannten Werten für SrO überein. Auch die XEDS-Analysen zeigen lediglich das Vorhandensein von $Sr^{2+}$-Ionen in der Insel. Beides legt nahe, dass diese Insel aus SrO besteht mit der SrO-(260)-Ebene als Grenzfläche zu $SrTiO_3$. Das Wachstum der SrO-Inseln auf der $SrTiO_3$-(012)-Oberfläche resultiert in einer Gitterfehlpassung von 4% in $[210]_{SrTiO3}$-Richtung beziehungsweise ~30% in $[001]_{SrTiO3}$-Richtung der Grenzfläche.
Es bleibt zu klären, inwieweit die Orientierung der Oberflächen, d. h. die spezifische atomare Struktur der Oberflächen, die Inselbildung bestimmt. Hierfür sind allerdings Untersuchungen an zahlreichen weiteren Inseln erforderlich.

## 2. Kinetische Entmischung im oberflächennahen Bereich

Nach der Reoxidation bildet sich in der Nähe der Oberfläche eine optisch transparente Schicht, deren Dicke etwa 50-70 µm beträgt. In dieser Schicht läßt sich eine ausgeprägte Inhomogenität der Kationen nachweisen. In der Nähe der Oberfläche findet eine Anreicherung von $Sr^{2+}$-Ionen statt. Dies ist auf den ersten Blick überraschend, da man bei der Reoxidation auf Grund der zu erwartenden Sr-Leerstellen eine erniedrigte Sr-Konzentration nahe der Oberfläche erwarten würde. Anderseits liegt im tieferen Bereich der reoxidierten Schicht ein $Ti^{4+}$-Überschuss vor. Hinsichtlich $Nb^{5+}$-Ionen lassen sich keine signifikante

Konzentrationsunterschiede in der Oxidationsschicht nachweisen.

Der starke Gradient des chemischen Potentials des Sauerstoffs zwischen Oberfläche und Probeninneren wirkt jedoch als treibende Kraft für eine kinetische Entmischung der Kationen. Voraussetzung für die kinetische Entmischung sind unterschiedliche Beweglichkeiten der verschiedenen Kationen, wie dies in $SrTiO_3$ der Fall ist. Die Anreicherung der beweglicheren $Sr^{2+}$-Kationen in Bereichen mit höherem chemischen Potential des Sauerstoffs, insbesondere nahe der Oberfläche, stimmt mit diesem Model überein. Die in dieser Arbeit beschriebenen Messungen stellen den ersten experimentellen Nachweis für eine kinetische Entmischung in $SrTiO_3$ dar. Es ist anzunehmen, dass in oberflächennahen Bereichen (höherer $p(O_2)$-Bereich) überschüssige $Sr^{2+}$-Kationen die $Ti^{4+}$-Gitterplätze besetzen und hierdurch $Sr_{Ti}^{''}$-Defekte verursachen, die elektrische Ladung von $Nb_{Ti}^{\bullet}$ kompensieren. Die Vergrößerung der Gitterkonstante (um 0.3%) in diesem Bereich im Vergleich zu der von $SrTiO_3$ bestätigt diese Annahme.

Diese Arbeit liefert somit erstmals starke Hinweise, dass zusätzlich zum üblicherweise diskutierten Mechanismus der Ladungskompensation ($e'$ oder $V_{Sr}^{''}$) auch Anti-Site-Defekte ($Sr_{Ti}^{''}$) zu einer Kompensation der Donator-Ionen führen können. An der Unterseite der reoxidierten Schicht (niedriger $p(O_2)$-Bereich) besetzen die überschüssigen $Ti^{4+}$-Kationen dagegen vermutlich $Sr^{2+}$-Gitterplätze und verursachen dadurch $Ti_{Sr}^{\bullet\bullet}$-Defekte. Der Ladungsausgleich der $Ti_{Sr}^{\bullet\bullet}$- und $Nb_{Ti}^{\bullet}$-Defekte erfolgt in diesem Bereich wohl durch Elektronen und/oder durch $V_{Sr}^{''}$-Defekte.

## 3. Bildung der RP-Phase an Korngrenzen

An den Trippl punkten läßt sich nach der Reoxidation eine $Sr^{2+}$-reiche zweite Phase ($Sr_2TiO_4$) nachweisen. Dies macht sich im TEM-Beugungsbild bei Projektion auf die [100] bzw. [210] Zonen-achse durch eine zusätzlichen Reflexion in [001]-Richtung bemerkbar. $Sr_2TiO_4$ gehört zur homologen Reihe $Sr_{n+1}Ti_nO_{3n+1}$, die als Ruddlesden-Popper Phasen (RP-Phase) bekannt sind. Auf Grund der bislang gewonnen Daten kann die Existenz der anderen Reihenmitglieder ($n$ = 2, 3, ...) nicht ausgeschlossen werden. Damit konnte zum ersten Mal eine durch Reoxidation verursachte Korngrenzen-Phase (RP-Phase) in $SrTiO_3$ nachgewiesen werden.

Verschiedene Autoren (z.B. [Daniels, 76], [Moos, 97b]) hatten die Phase zwar vorhergesagt, konnten jedoch keinen experimentellen Nachweis führen.

Die Arbeit führt insgesamt zu einem wesentlich verbesserten Verständnis der chemischen und strukturellen Phänomene an Oberflächen und im Volumen von donator-dotiertem $SrTiO_3$ nach der Reoxidation geführt.

# Appendix A

## Sample preparation

### i) Sample preparation for LM / OIM / SEM studies

In this work the specimens have to be polished to mirror quality. An excellent polished surface is a prerequisite for performing surface reoxidation experiments as well as OIM investigations. Well polished surfaces produce clear and sharp EBSD patterns and this, in turn, leads to a high degree confidence in OIM map (section 3.1.II). In the following the surface preparation route is briefly explained:

- Wet grinding of the sample on SiC papers
- Polishing of the surface with 6, 3, and 1 μm diamond particle size on a pellon, hard synthetic and hard silk cloths
- Final polishing (etch polishing) of the surface on a short napped fiber cloth with a diluted silicon dioxide suspension (0.05 μm)
- Chemical etching in an $HF + H_2O$ -solution (1:4 volume fraction) for 20-30 seconds

### ii) TEM specimen preparation

For TEM investigations an excellent specimen has to be prepared with a thickness in range of 100 to 300 nm. The preparation route for providing such thin foils is schematically shown in Fig. A1.

For TEM studies of the secondary phase formed on the surface of the polycrystalline sample, one needs to prepare cross sectional TEM samples. For this reason a piece of Si wafer is glued on top of the sample (Fig. A2). This protects the secondary phase during preparation. The resulting sandwich (sample-epoxy glue-Si wafer) is cut into slices perpendicular to the plane of the sample surface. The subsequent preparation steps follow the same route as in the case of plane-view preparation (Fig A1).

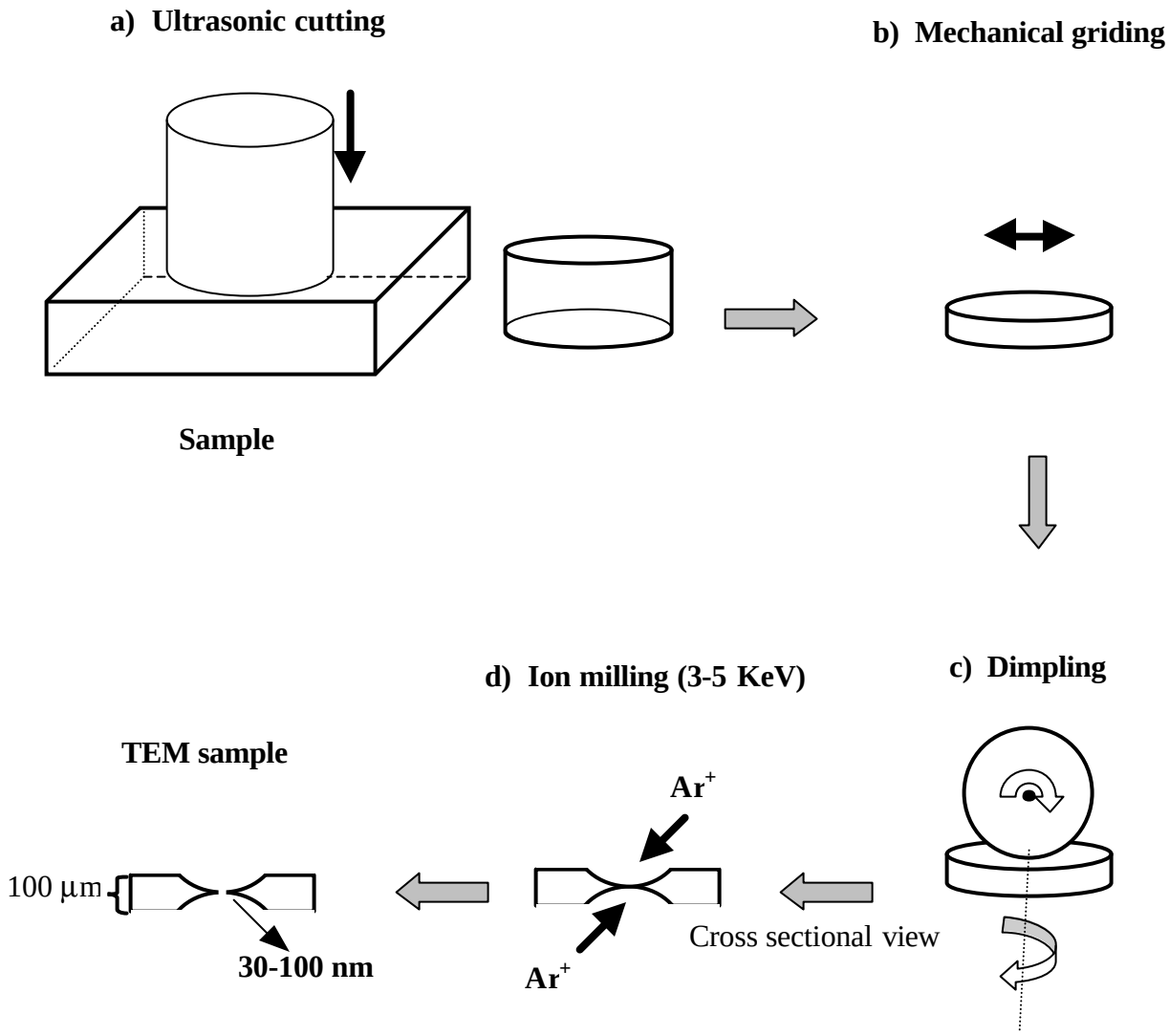


**Fig. A1:** Plan-view preparation steps : **a)** cutting of the sample into a disc with a diameter of 3 mm and a thickness of 500 µm; **b)** mechanical grinding and polishing of the disk from both sides down to 100 µm; **c)** dimpling to form a wedge-shaped dip down to a thickness of about 30 µm in the middle of the sample; **d)** ion milling ($Ar^+$-ions) until a hole in the middle of the sample appears. The edge of the hole is the electron transparent region.

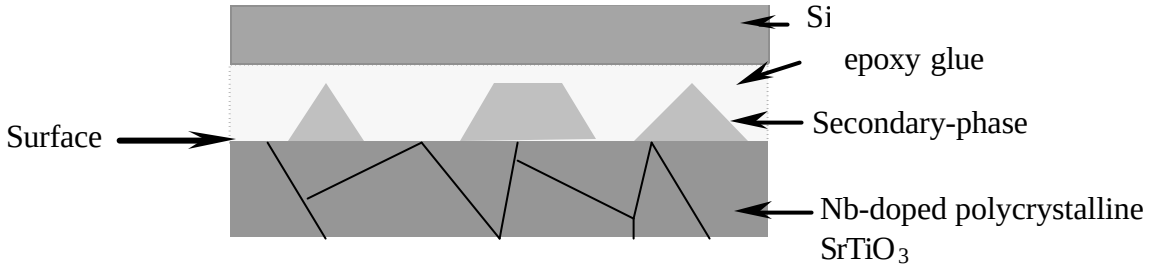


**Fig. A2:** Cross section of a sample with the secondary phase at top of its surface. To protect the secondary phase during TEM preparation a Si-layer is glued on top of the sample. (The subsequent preparation follows the plane-view procedure (Fig. A1)).

## iii) Selection of proper electrodes for impedance measurements

For the performance of impedance spectroscopic measurements, the ohmic behavior of the electrodes (negligible specimen-electrode interfacial resistance) is very important. Otherwise, a third semicircle (in Fig. 3.11b) due to the formation of Schottky barrier at the interface of electrode/sample has to be considered. This may overlap with the GB-semicircle and makes the interpretation of the impedance spectra more difficult [Sundaram, 94]. For this reason, ohmic InGa electrodes [Makovec, 01] are prepared from In-Ga alloy with eutectic composition and deposited on both sides of Nb-doped $SrTiO_3$ samples. This alloy can be easily spread on the polished surface of the sample.

# Appendix B

In the following Table B1, the oxidation level of the GBs and their geometrical data are given. The data of the GBs in terms of the misorientation angle of the neighboring grains ($q$), rotation axis <*uvw*> and the lattice plane of the corresponding grains, i.e. $(hkl)_1$ and $(hkl)_2$ are obtained from OIM. Depending on the misorientation angle, different types of GBs were distiguished: small angle GBs (SAGB: $q \leq 15°$), coincidence site lattice boundaries ($\Sigma$) and general GBs. The oxidation tendency of the GBs was qualitatively evaluated by means of optical microscopy and classified in four categories: strong (S), partial (P), weak (W) and immune (I) (Fig. 5.9).

**Table B1:** Geometrical data of the GBs (up to $\Sigma$39) determined by OIM and the oxidation tendencies of the corresponding GBs observed by optical microscopy.

| Type of GB | Rotation data | | $(hkl)_1$ | $(hkl)_2$ | Oxidation tendency of GB |
|---|---|---|---|---|---|
| | <*uvw*> | $q$ | | | |
| | | | | | |
| SAGB | 2 3 7 | 19.6° | 2 1 2 | 3 0 4 | I |
| | 3 7 14 | 8.1 | 0 0 1 | 0 0 1 | W |
| | 3 1 5 | 10° | | | P |
| | 3 3 1 | 10.5 | 5 7 3 | 19 –6 22 | P |
| | 3 1 -5 | 9.9° | | | P |
| | 8 1 4 | 15.35 | 0 0 1 | 0 1 3 | S |
| | 1 1 0 | 13.8 | 11 15 21 | -1 1 1 | S |
| | | | | | |
| $\Sigma$3 | 7 5 7 | 58.9 | 6 –1 8 | 00 1 | I |
| | 1 1 1 | 55.26 | 2 5 14 | 1 4 10 | I |
| | 1 1 1 | 59.24 | | | S |
| | 1 1 -1 | 57.65 | 0 0 1 | -2 1 2 | S |
| | 12 15 13 | 57.96±5.7 | 6 8 15 | 2 1 2 | S |
| | | | | | |
| $\Sigma$5 | 0 1 0 | 41±6 | 1 4 4 | 0 0 1 | I |
| | 1 0 0 | 34.16±5 | 0 1 4 | 0 2 2 | S |
| | 1 0 0 | 35.87 | 1 2 2 | 2 5 13 | S |
| | | | | | |
| $\Sigma$ 7 | 1 1 1 | 42.72 | 0 0 1 | 1 1 2 | I |

| Type of GB | Rotation data | | $(hkl)_1$ | $(hkl)_2$ | Oxidation tendency of GB |
|---|---|---|---|---|---|
| | <*uvw*> | *q* | | | |
| Σ9 | 0 2 2 | 35.24±4 | 2 11 28 | 001 | I |
| | 1 1 0 | 39.9±3.5 | 6 5 14 | 10 1 16 | S |
| | 2 2 0 | 37 | 1 9 12 | 8 1 15 | S |
| | | | | | |
| Σ11 | 1 0 1 | 48±4 | 6 1 9 | 3 1 4 | I |
| | 0 1 1 | 50.96±1.7 | | | I |
| | | | | | |
| Σ13a | 0 –1 0 | 25.8±3.7 | 9 26 12 | 5 7 19 | P |
| Σ13b | 12 –15 16 | 30.18 | | | I |
| | | | | | |
| Σ15 | 14 5 6 | 49.39 | 0 1 1 | 102 | I |
| | 2 1 0 | 46.8 | 0 0 1 | 3 9 7 | W |
| | 3 5 0 | 50.18±3.6 | 1 12 28 | 4 3 3 | S |
| | | | | | |
| Σ17a | 0 0 1 | 29.9 | -1 4 3 | 1 4 3 | I |
| | 0 0 1 | 28.8 | 1 4 3 | 1 4 3 | I |
| | 0 0 1 | 29.43 | 2 7 29 | 6 2 22 | S |
| | | | | | |
| Σ21b | 9 8 16 | 44.9±2.2 | 1 2 3 | 0 0 1 | P |
| Σ21b | 5 11 5 | 44.5±2.3 | 3 0 5 | 2 6 29 | P/W |
| | | | | | |
| Σ23 | 21 7 6 | 41.9 | 9 2 14 | 1 2 2 | S |
| | | | | | |
| Σ33b | 3 8 3 | 34.9±1.8 | 0 0 1 | 7 6 12 | W |
| | | | | | |
| Σ37b | 3 1 0 | 43.5 | 6 1 9 | 11 14 19 | P |
| | | | | | |
| Σ39a | 111 | 31.6 | -1 5 12 | -4 19 -20 | S |

| Type of GB | Rotation data | | $(hkl)_1$ | $(hkl)_2$ | Oxidation tendency of GB |
|---|---|---|---|---|---|
| | <*uvw*> | *q* | | | |
| General GBs | -2 1 0 | 43.93 | 10 1 16 | 14 19 18 | I |
| | 4 6 -22 | 44.27 | 0 –1 3 | -3 –2 6 | I |
| | 12 20 11 | 54 | -2 2 1 | 2 7 12 | I |
| | -12 –5 -8 | 21.8 | 2 –5 14 | 0 0 1 | I |
| | 4 1 -10 | 39.2 | 0 1 3 | -1 0 3 | I |
| | 2 3 3 | 58.8 | 1 0 4 | 3 0 4 | I |
| | 2 –2 -1 | 57.7 | -6 4 11 | 2 –2 4 | I |
| | 6 27 -9 | 35.7 | 3 5 15 | 7 1 7 | I |
| | 2 3 2 | 29.5 | 3 0 5 | -3 0 4 | I |
| | 2 0 2 | | 1 6 4 | 4 1 3 | I |
| | 14 7 11 | 29 | 1 9 8 | 6 2 9 | I |
| | 12 2 | 55 | -4 3 3 | 1 2 3 | I |
| | 5 15 2 | 34.3 | 0 0 1 | 1 0 2 | I |
| | 14 2 -5 | | 1 9 22 | 0 0 1 | I |
| | 0 5 3 | 38.7 | 1 2 2 | -1 2 2 | I |
| | -19 5 3 | 35 | 0 0 1 | 10 14 25 | I |
| | 3 16 15 | 43.7 | 2 0 2 | 6 3 25 | I |
| | 15 19 17 | 52.2 | 13 11 21 | 3 2 7 | I |
| | 1 0 3 | 35.37 | 6 2 22 | 1 4 9 | I |
| | 3 4 1 | 55.55 | 0 0 1 | 11 17 18 | I |
| | 2 6 5 | 51.74 | 1 0 0 | 2 1 2 | I |
| | 1 0 0 | 27.12 | 4 2 9 | 14 16 20 | I |
| | 3 1 4 | 31.13 | -17 16 19 | 8 10 14 | W |
| | 16 23 11 | 36.7 | 5 2 13 | 0 0 1 | W |
| | 1 9 6 | 45.95 | 1 17 14 | 2 5 14 | W |
| | 5 4 3 | 47 | 2 5 14 | 3 5 4 | W |
| | -9 6 5 | 47.82 | 6 2 29 | 1 6 5 | W |
| | -19 –13 -2 | 48.4 | 5 6 25 | 5 3 7 | W |
| | 1 1 1 | 52.7 | -10 6 15 | 7 20 15 | W |
| | 6 23 2 | 38 | 8 5 12 | 0 0 1 | W |
| | 4 8 11 | 54 | 1 2 2 | 5 2 12 | W |
| | 3 –4 12 | 44.4 | 0 0 1 | 3 9 21 | C/W |
| | -5 14 3 | 36.65 | 9 –3 19 | -6 –3 29 | C/W |
| | 4 9 2 | 45.56 | 9 5 17 | 2 2 4 | C/W |
| | 17 19 12 | 54.23 | 1 9 8 | 2 4 9 | P/W |
| | -11 14 7 | 51.75 | 3 0 5 | 2 11 28 | P/W |
| | 1 0 0 | 28.38 | 0 0 1 | 0 1 2 | P/W |

| Type of GB | Rotation data | | $(hkl)_1$ | $(hkl)_2$ | Oxidation tendency of GB |
|---|---|---|---|---|---|
| | <*uvw*> | *q* | | | |
| General GBs | 3 5 1 | 37.26 | 2 2 1 | 7 8 18 | P |
| | 8 5 4 | 50.66 | 8 –7 17 | 0 1 3 | P |
| | 5 13 -2 | 43.7 | 6 1 9 | -7 –2 24 | P |
| | 1 2 2 | 56 | 7 0 11 | -1 3 4 | P |
| | 16 5 6 | 45.8 | 1 2 2 | 6 1 9 | P |
| | 3 5 7 | 55.3 | 1 11 28 | 1 16 18 | P |
| | 5 3 4 | 50.36 | 4 11 16 | 1 3 5 | P |
| | 1 –7 7 | 33.7 | 1 3 5 | 2 6 29 | P |
| | 0 1 0 | 40.5 | 0 0 1 | 8 5 14 | P |
| | 20 14 17 | 44.86 | 1 3 5 | 2 4 11 | P |
| | 10 15 6 | 48.53 | 16 10 24 | 0 1 2 | P |
| | 3 2 1 | 52.7 | 0 0 1 | 12 16 23 | P |
| | 3 1 4 | 39.06 | 7 8 18 | -10 9 6 | S |
| | 8 2 3 | 45.6 | -2 2 1 | -4 0 8 | S |
| | 3 6 -10 | 52.3 | -4 0 8 | 0 0 1 | S |
| | 20 7 9 | 45.5 | 7 8 17 | 2 –5 14 | S |
| | -7 2 -3 | 49 | 0 1 3 | 3 4 0 | S |
| | 2 3 -7 | 34.6 | 5 17 15 | 6 11 14 | S |
| | 27 7 -10 | 48 | 0 0 1 | 0 1 0 | S |
| | -17 –1 14 | 52.6 | -5 17 15 | 0 0 1 | S |
| | 11 –10 2 | 53.48 | 14 13 16 | 0 0 1 | S |
| | 3 14 -10 | 39.2 | 3 4 15 | -6 7 6 | S |
| | 273 | 46.37 | 6 1 9 | 3 9 7 | S |
| | 14 –17 -2 | 52.7 | 5 8 28 | 6 1 8 | S |
| | 4 2 2 | 27.9 | 9 2 14 | 5 –2 13 | S |
| | -5 1 3 | 38.9 | 9 2 14 | 1 2 2 | S |
| | 17 –5 -4 | 40.38 | 0 0 1 | 0 1 1 | S |
| | 12 5 -27 | 47.87 | 0 0 1 | 1 –11 28 | S |
| | -1 0 4 | 42.34 | 0 0 1 | 0 0 1 | S |
| | 4 5 3 | 40.64 | 354 | 3 5 15 | S |
| | 3 1 4 | 35 | 0 1 3 | 7 2 29 | S |
| | 4 1 -8 | 39.6 | -4 –4 15 | 7 2 -29 | S |
| | 3 0 -4 | 46.5 | 0 1 1 | -10 –6 15 | S |
| | 2 1 2 | 38.44 | 9 3 10 | 4 1 3 | S |
| | 8 1 9 | 56.2 | 1 2 2 | 13 4 27 | S |
| | 8 15 6 | 51 | 2 0 2 | 0 1 2 | S |
| | 22 4 15 | 39.9 | 5 17 9 | 1 1 5 | S |
| | 11 2 5 | 44.13 | 2 1 2 | 15 15 20 | S |

# References


[Abrantes, 20] J.C. Abrantes, J.A. Labrincha, "Representations of impedance spectra of ceramics, PartII: Spectra of polycrystalline $SrTiO_3$", *Mater. Res. Bull.*, 35 (2000) 965.

[Akhtar, 95] M.J. Akhtar, Z.N. Akhtar, R.A. Jackson, C.R.A. Catlow, "Computer Simulation Studies of STO" *J. Am. Ceram. Soc.*, 78 [2] (1995) 421.

[Anderson, 85] H.U. Anderson, M.M. Nasrallah, B.F. Flandermeyer, A.K. Agrwal, "High temperature redox behavior of doped $SrTiO_3$ and $LaCrO_3$", *J. Solid State Chem.*, 56 (1985) 325.

[Aruta, 01] C. Aruta, "Structure of superconducting $[BaCuO_x]_2[CaCuO_2]_n$ superlattices on SrTiO3(001) investigated by X-ray scattering", *Phys. Status Solidi A*, 183 (2001) 353.

[Balachandran, 82a] U. Balachandran and N.G. Eror, "Electrical Conductivity in La-Doped $SrTiO_3$" *J. Electrochem. Soc.*, 129 [5] (1982) 1021.

[Balachandran, 82b] U. Balachandran and N.G. Eror, "On the defect structure of $SrTiO_3$ with excess SrO", *J. Mater. Sci.*, 17 (1982) 2133.

[Bauerle, 69] J.E. Bauerle, "Study of solid electrolyte polarization by a complex admittance method", *J. Phys. Chem. Solids*., 30 (1969) 2657.

[Blendell, 99] J.E. Blendell, W.C. Carter, "Faceting and Wetting Transition of Anisotropic Interfaces and Grain Boundaries.", *J. Am. Ceram. Soc.*, 82 [7] (1999) 1889.

[Brandon, 66] D. G. Brandon, "The Structure of High-Angle Grain Boundaries", *Acta Metall.*, 14 (1966) 1479.

[Bristowe, 20] P.D. Bristowe, "Theoretical investigations of interfaces in electroceramic materials", Interface Controlled Materials, eds M. Rühle et. al Wiley-VCH, vol. 19 (2000) 222.

[Brooks, 87] N.B. Brooks, G. Thornton, "$SrTiO_3$(100) step sites as catalytic centers for $H_2O$ dissociation", *Solid State Commun*., 64 (1987) 383.

[Castel, 02] M.R. Castel, "STM of reconstruction on the $SrTiO_3$ (001) surface" *Surf. Sci*., 505 (2002) 1.

[Chan, 81] N.H. Chan, R.K. Sharma, D.M. Smyth, "Nonstoichiometry in $SrTiO_3$", *J. Electroceram. Soc. : Solid-State Science and Technology,* 128 [8] (1981) 1762.

[Chan, 86] H.M. Chan, M.P. Harmer, D.M. Smyth, "Compensating Defects in Highly Donor-Doped $BaTiO_3$", *J. Am. Ceram. Soc.*, 69 [6] (1986) 507.

[Ceh, 94] M. Che, D. Kohlar, "Solubility of CaO in $CaTiO_3$", *J. Mater. Sci.*, 29 [23] (1994) 6295.

[Chiang, 90] Y. M. Chiang and T. Tadagi, "Grain-Boundary chemistry of barium titanate and strontium titanate: I., High-temperature equilibrium space charge", *J. Am Ceram. Soc*., 73 (1990) 3278-3285.

[Chiang, 97] Y.M. Chiang, D. Birnie, W.D. Kingery, *"Physical Ceramics"*, Wiley Press, New York, 1997.

[Cho, 94] S.G. Cho, P.F. Johnson, "Evolution of the microstructure of undoped and Nb-doped $SrTiO_3$", J. Mater. Sci., 29 (1994) 4866.

[Daniels, 76] J. Daniels and K.H. Härdtl, "Electrical conductivity at high temperatures of donor-doped $BaTiO_3$ ceramic" *Phillips Res. Repts.*, 31 (1976) 489.

[de Groot, 89] F.M.F. de Groot, M. Grioni, "Oxygen 1s X-ray-absorption edges of transition-metal oxides", *Phys. Rev.* **B,** 48 (1989) 5715.

[Denk, 97] I. Denk, J. Maier, "Electrochemical investigations of $SrTiO_3$ boundaries", *J. Electrochem. Soc*., 144 (1997) 3526.

[Desu, 90] S.B. Desu, D.A. Payne, "Interfacial segregation in perovskites: I. Theory", *J. Am Ceram. Soc*., 73 (1990) 3391.

[Eror, 81] N.G. Eror, U. Balachandran, "Self-Compensation in Lanthanum-doped $SrTiO_3$", *J. Solid State Chem.*, 40 (1981) 85.

[Erdman, 03] N. Erdman, L.D. Marks, " $SrTiO_3$ (001) surface structures under oxidizing conditions" *Surface Science*, 526 (2003) 107.

[Feighery, 01] A.J. Feighery, J.C.C. Abrantes, J.M.F. Ferreira "Microstructural effects on the electrical behavior of $SrTi_{0.95}Nb_{0.05}O_{3+\delta}$ materials on changing from reducing to oxidizing conditions", *Sensors and Actuators* **B**, 75 (2001) 88.

[Flandermeyer, 84] B.F. Flandermeyer, A.K. Agrwal, H.U. Anderson, "Oxidation-reduction behavior of La-doped $SrTiO_3$" *J. Mater. Science*, 19 (1984) 2593.

[Fleig, 20] J. Fleig S. Rodewald, J. Maier, " Microcontact impedance measurements of individual highly resistive grain boundaries: General aspects and application to acceptor-doped $SrTiO_3$", *J. Appl. Phys.*, 87 [5] (2000) 2372.

[Fu, 02] Q. Fu, Th. Wagner, "Thermal stability of Cr clusters on $SrTiO_3$ (100)", *Sur. Sci.* 505 (2002) 39.

[Fujimoto, 85a] M. Fujimoto, W.D. Kingery, "Microstructure of $SrTiO_3$ Internal Boundary Layer Capacitors" *J. Am. Ceram. Soc*., 68 [49 (1985) 169.

[Fujimoto, 85b] M. Fujimota, M. Watanabe, "$Ti_nO_{2n-1}$ Magneli phase formation in $SrTiO_3$ dielectrics", *J. Mater. Sci.*, 20 (1985) 3683.

[Gopel, 85] W. Gopel, "Chemisorption and charge transfer at ionic semiconductor surfaces. Implications in designing gas sensors", *Prog. Surf. Sci.*, 20 (1985) 9.

[Greuter, 99] F. Greuter and G. Blatter, *Semicond. Sci. Technol.*, 5 [111] (1999).

[Gülgün, 99] M.A. Gülgün, V. Putlayev, M. Rühle, "Effects of Yttrium Doping a-Aumina: I, Microstructure and Microchemistry", *J. Am. Ceram. Soc.*, 82 [7] (1999) 1849.

[Gunhold, 03] A. Gunhold, l. Beuermann, M. Frerichs, "Island Formation on 0.1 at.% La-Doped $SrTiO_3$ at elevated Temperature Under Reducing Conditions", *Surface Science*, 523 (2003) 80.

[Hirata, 94] A. Hirata, A. Ando "Characterization of surface-defects formation in $SrTiO_3$ (100)" *Surf. Sci.*, 310 (1994) 89.

[Hirsch, 65] P. Hirsch, A. Howie, R. Nichclson, "*Electron Microscopy of Thin Crystall"*, Malabar, Florida, Kriger Publishing CO., (1965)

[Henrich, 78] V.E. Henrich, G. Dresselhous, H.J. Zeiger, "Surface defects and the electronic structure of $SrTiO_3$ surfaces", *Phys. Rev.* B, 17 (1978) 4908.

[Heywang, 61] W. Heywang, "Bariumtitanat als sperrschichthalbleiter", *Solid State Electronics*, 3 [1] (1961) 51.

[JCPDS] Powder Diffraction File Card No. 35-0734, Joint Committee on Powder Diffraction Standards, Swarthmore, PA, 1994.

[Kim, 01] S.H. Kim, H.H.Moon, J.H.Park, "Analysis of defect formation in Nb-doped $SrTiO_3$ by impedance spectroscopy",*J. Mater. Res.*, 16[1] (2001).

[Königstein, 98] M. Königstein, C. Richard and A. Catlow "Ab initio quantum mechanical study of the structure and stability of the alkaline earth metal oxides and peroxides", *J. Solid State Chemistry*, 140 (1998) 103.

[Kröger, 56] F.A. Kröger and H.J. Vink, "Relations between the Concentrations of Imperfections in Solids", *Solid State Physics*, 3 (1956) 307.

[Kubo, 98] M. Kubo, Y. Ourni, "Molecular dynamics simulation on a layer-by-layer homoepitaxial growth process of SrTiO3(001)", *J. Chem. Phys.*, 109 (1998) 8601.

[Kubo, 03] M. Kubo, H. Nozoye, "Surface structure of SrTiO3(100)", *Surf. Sci.*, 542 (2003) 177.

[Lee W.H., 01] W.H. Lee, T.Y. Tseng, D. Hennings, "Effects of ceramic processing parameters on the microsstructure and electric properties of ($Ba_{1-x}Ca_xTi_{1-y}Zr_yMn_{0.01}O_3$) sintered in a reducing atmosphere" *J. Mater. Sci* , 12 (2001) 123.

[Lee J.K., 01] J.K. Lee, K.S. Hong, "Revisit to the origin of grain growth anomaly in Y-doped $BaTiO_3$", *J. Am. Ceram. Soc.*, 84 [8] (2001).

[Leonhardt, 02] M. Leonhardt, R.A, De Souza, "Surface kinetics of oxygen incorporation into $SrTiO_3$", *J. Electrochem. Soc.*, 149 [2] (2002) 19.

[Levin, 64] E.M. Levin, C.R. Robbins, "Phase Diagrams for Ceramics", New York, The American Ceramic Society, 1964.

[Levinson, 86] L.M. Levinson, H.R. Philipp, "Zinc oxide varistors-a review", *Am. Ceram. Soc. Bull.*, 65 (1986) 639.

[Liang, 94] Y. Liang, D.A. Bonnell "Structures and chemistry of the annealed $SrTiO_3$ (100) surface" *Surf. Sci.*, 310 (1994) 128.

[Liang, 95] Y. Liang, D.A. Bonnell "Effect of variations in stoichiometry on the

surface structure of $SrTiO_3$ (100)", *J. Am. Ceram. Soc.*, 87 (1995) 2633.

[Maier, 20] J. Maier, *"Festkörper-Fehler und Funktion"*, Teubner Verlag, (2000).

[Mao, 97] Z. Mao, K.M. Knowles, "Characterization of interfacial effects in $SrTiO_3$ ceramics" *Electron microscopy and analysis*, (1997) 523. (Conference, Cambridge, UK, 2-5 sept 1997)

[Mavroides, 76] J.G. Mavroides, J.A. Kafalas, " Photoelectrolysis of water in cells with $SrTiO_3$ anodes", *Appl. Phys. Lett*., 28 (1976) 241.

[McCoy, 97] M.A. McCoy, R.W. Grimes, W.E. Lee, "Phase stability and interfacial structures in SrO-$SrTiO_3$", *Philosophical Magazine* A, 75[3] (1997)833.

[McKee, 98] R.A. McKee, F.J. Walker, "Crystalline oxide on silicon: the first five monolayer", *Phys. Rev. Lett*., 81 (1998) 3014.

[McKee, 01] R.A. McKee, F.J. Walker, "Physical structure and inversion charge at a semiconductor interface with a crystalline oxide ", *Science*, 293 (2001) 468.

[McIntyre, 20] P.C. McIntyre, "Equilibrium point defects and electronic carrier distributions near interfaces in acceptor-doped Strontium titanate" *J. Am Ceram. Soc*., 83 [5] (2000) 1129.

[Menesklou, 97] W. Menesklou, "Kompensationsmechanismen der Überschussladung in Lanthandotiertem Barium- und Strontium titanat", *PhD Thesis*, Karlsruhe (Germany), VDI-Verlag Reihe 5, Nr. 481 (1997).

[Menesklou, 99] W. Menesklou, H.J. Schreiner, K.H. Härdtl, " High temperature oxygen sensors based on doped $SrTiO_3$", *Sensors and Actuators* **B**, 59 (1999) 184.

[Meyer, 99] R. Meyer, R. Waser, "Restructuring the surface region of donor doped

$SrTiO_3$ single crystals under oxidizing conditions" *Ferroelectrics*, 224 (1999) 323.

[Meyer, 02] R. Meyer, R. Waser, "Cationic surface segregation in donor-doped $SrTiO_3$ under oxidizing conditions" *J. Electroceramics*, 9 (2002) 101.

[Mokovec, 95] D. Mokovec, Z. Samardzija, U. Delalut, "Defect structure and phase relations of highly La-doped $BaTiO_3$*"* *J. Amer. Ceram. Soc.*, 78 [8] (1995) 2193.

[Mokovec, 01] D. Mokovec, N. Ule, "Positive temperature coefficient of resistivity effect in highly donor-doped $BaTiO_3$*"*, *J. Am. Ceram. Soc.*, 84 [6] (2001) 1273.

[Monceau, 91] D. Monceau, C. Petot, G. Petot-Ervas, "Kinetic demixing profile calculation in oxide solid solution under a chemical potential gradient", *Solid State Ionics, Diffusion & Reactions*, 45 [3-4] (1991) 231.

[Moos, 97a] R. Moos, T. Bischoff, K.H. Härdtl, "Solubility of La in $SrTiO_3$ in oxygen rich atmosphere", J. *Mater. Sci.*, 32 (1997) 4247.

[Moos, 97b] R. Moos and K.H. Härdtl, "Defect chemistry of donor-doped and undoped $SrTiO_3$ ceramic between 1000 and 1400°C", *J. Am. Ceram. Soc.*, 80 [10] (1997) 2549.

[Noguera, 96] C. Noguera, *"Physics and Chemistry at Oxide Surfaces"*, Cambridge University Press, (1996).

[Olsson, 89] E. Olsson, G.L. Dunlop, " Characterization of individual interfacial barriers in a ZnO varistor material", *J. Appl. Phys.*, 66 (1989) 3666.

[Polli, 99] A.D. Polli, Th. Wagner, M. Rühle, "Effect of Ca impurities and wet chemical etching on the surface morphology of SrTiO3 substrates", *Surf. Sci.*, 429 (1999) 237.

[Reihl, 84] B. Reihl, J.G. Bednorz, "Electronic-structure of $SrTiO_3$", *Phys. Rev.* B, 30 (1984) 803.

[Rodewald, 01] S. Rodewald, J. Fleig, M. Maier, "Microcontact Impedance Spectroscopy at Single Grain Boundaries in Fe-doped $SrTiO_3$ Polycrystals", *J. Am. Ceram. Soc.*, 84 [3] (2001) 521.

[Rossel, 94] C. Rossel, A. Catana, "Microstructure of (001), (110) and (103) oriented thin films of $YBa_2Cu_3O_{7-x}$ investigated with STM, SEM and HRTEM", *Physica* C, 223 (1994) 370.

[Ruddlesdon, 57] S.N. Ruddlesdon and P. Popper, "New compounds of the $K_2NiF_4$" *Acta Crystallogr.*, 10 (1957) 538.

[Sano, 03] T. Sano, D.M. Saylor, "Surface energy anisotropy of $SrTiO_3$ at 1400°C in air", *J. Am. Ceram. Soc.* 86 [11] (2003) 1933.

[Schmalzried, 79] H. Schmalzried, W. Laqua, "Crystalline oxide solid solutions in oxygen potential gradients", Z. *Naturforsch.*, 34A [2] (1979) 192.

[Smyth, 85] Y.H. Hu, M.P. Harmer, D.M. Smyth, "Solubility of BaO in $BaTiO_3$", *J. Am. Ceram. Soc.*, 68, [7], (1985) 372.

[Schwartz, 20] A.J. Schwartz, M. Kumar, B.L. Adams *"Electron Backscatter Diffraction in Material Science"*, Kluwer Academic, Plenum Publishers, New York (2000).

[Sekiguchi, 98] S. Sekiguchi, M. Fujimoto, "Structure Analysis of $SrTiO_3$ (111) Polar Surface", *Jpn. J. Appl. Phys.*, 37 (1998) 4140.

[Sundaram, 94] S.K. Sundaram, "The electrode effect in reduced semiconduction Nb-doped $SrTiO_3$ ceramics", *J. Mat. Sci*, 5 (1994) 344.

[Szot, 99] K. Szot and W. Speier, "Surface of reduced and oxidized $SrTiO_3$ from

atomic microscopy", *Phys. Rev. B*, 60 (1999) 5909.

[Szot, 20] K. Szot et al. "Formation of micro-crystals on the (100) surface of $SrTiO_3$ at elevated temperatures", *Surf. Sci*., 460 (2000) 112.

[Tambo, 98] T. Tambo, T. Nakamura, "Molecular Beam Epitaxy of $SrTiO_3$ Film on Si (100) with SrO Buffer Layer", *Jpn. J. Appl. Phys.*, 37 (1998) 4454.

[Tanaka, 93] H. Tanaka, T. Matsumoto "Surface-structure and electronic property of reduced $SrTiO_3$ (100) surface observed by scanning tunneling microscopy spectroscopy." *Jpan. J. Appl. Phys.* 32 (1993) 1405.

[Teller, 97] O. Teller, M. Martin, "Kinetic demixing of (Co,Ni)O in an electric field", *Solid State Ionics, Diffusion & Reactions*, 101-103 (1997) 475.

[Tien, 67] T.Y. Tien, F.A. Hummel, "Solid Solution in the System $SrTiO_3$", *Trans, Br. Ceram. Soc.*, 66 (1967) 233.

[Tilley, 77] R.J.D. Tilley, "An Electron Microscopy Study of Perovskite-Related Oxides in the Sr-Ti-O system", *J. Solid State Chem.*, 21 (1977) 293.

[Uematsu, 84] K. Uematsu, O. Sakurai, N. Mizutani and M. Kato, "Electrical properties of La-doped SrTiO3 (La: 0.1 to 2.0 at.%) single crystals grown by xenon-arc image floating zone method", *J. Mater. Sci.*, 19 (1984) 3671.

[Vollman, 94] M. Vollman and R. Waser, "Grain Boundary Defect Chemistry of Acceptor-Doped Titanates: Space Charge Layer Width" *J. Am Ceram. Soc*., 77 [1] (1994) 235.

[Waser, 91] R. Waser, "Bulk Conductivity and Defect Chemistry of Acceptor-Doped $SrTiO_3$ in the Quenched State", *J. Am. Ceram. Soc.*, 74 [8](1991) 1934.

[Williams, 96] D.B. Williams, C.B. Carter, *"Transmission Electron Micrscopy"*, Plenum Press, New York (1996).

[Wei, 98] M. Wei, L. Zhuang, "Preparation of $SrTiO_3$-based ceramic material for boundary layer capacitor by vacuum sintering method", J. Korean Phys. Soc., 32 (1998) 1180.

[Wei, 01] H. Wei, L. Beuermann, " Study of SrO segregation on $SrTiO_3$ (100) surfaces", *J.Eur. Ceram. Soc.* 21 (2001) 1677.

[Wernicke, 78] R. Wernicke, *Phys. Stat. Sol.*, 47a (1978) 139.

# Acknowledgement

This PhD work was performed under supervision of *Prof. Dr. Dr. h.c. M. Rühle* director at the Max-Planck-Institut für Metallforschung, Stuttgart.
I would like to express my deepest gratitude to *Prof. Rühle* for giving me the opportunity to do my PhD in his research group. I specially thank him for the constant support and encouragement during my work.

I greatfully acknowledge *Prof. Joachim Maier* director at the Max-Planck-Institut für Festkörperforschung for forward-looking suggestions and for providing access to the department facilities.

I would like to thank *Prof. Fritz Aldinger* and *Prof. Helmut Bertagnolli* for taking over the *Mitbericht* and *Mitprüfer*.

Sincere thanks to *Dr. Jürgen Fleig*, whose constant stream of ideas and inspiring encouragement was very motivating. The cooperation with him was a very rewarding and fulfilling experience, which I will always appreciate.

I thank *Mrs. Annette Fuchs*, *Mr. Peter Senk* and *Mr. Udo Klock* (Ceramic laboratory), *Mrs. Gabi Götz* (XRD) as well as *Mr. Uwe Traub* (software) for their friendly cooperativeness.

Sincere Thanks *to Dr. Albrecht Meyer* and his Colleagues in PML (Pulver metallurgisches Laboratorium) for ICP analysis.

I would like to thank the Metallography group, specially *Dr. Ewald Bischoff* for teaching me OIM and supporting me overcoming the hindrances. *Mrs. Margit Kapp*, *Mrs. Ulrike Täffner* and *Mr. Horst Opielka* are acknowledged for the excellent SEM specimen preparations.

Special thanks go to the TEM specimen preparation team, namely *Mrs. Ute Salzberger*, *Mrs. Maria Sycha* and *Mr. Adolf Strecker* for preparing excellent TEM specimens.

I gratefully appreciate colleagues for assistance during TEM investigations, namely *Mr. Kirsten Hahn*, *Mr. Peter Kopold* and *Mr. Jörg Thomas*.

I appreciate the critical and accurate scientific style of *Dr. Christoph Koch*, *Dr. Neng Yun Jin-Phillipp*, *Dr. Zaoli Zhang* and *Dr. Wilfrid Sigle* for the interpretation of the electron microscopy results.

I would also like to acknowledge *Prof. Eugene Kotomin*, *Dr. Roger De Souza*, *Dr. Palani Balaya*, *Dr. Rotraut Merkle*, and *Dr. Jong-Sook Lee* for fruitful discussions.

I am indebted to *my family* for their patience during my frequent absences at home. I admire them for being appreciative of my own agenda.